CONTROL OF SWITCHED RELUCTANCE MOTORS CONSIDERING MUTUAL INDUCTANCE

By

Han-Kyung Bae

Dissertation submitted to the faculty of the Virginia Polytechnic Institute and State University in partial fulfillment of the requirements for the degree of

Doctor of Philosophy

In

The Bradley Department of Electrical and Computer Engineering

APPROVED:

Dr. Krishnan Ramu, Chairman

Dr. Charles E. Nunnally

Dr. Robert W. Hendricks

Dr. Lamine Mili

Dr. Werner Kohler

August 9, 2000

Blacksburg, Virginia

Keywords: Switched Reluctance Motor, Mutual Inductance, Torque Distribution Function, Current Control, Flux Linkage Control, Unipolar Switching

CONTROL OF SWITCHED RELUCTANCE MOTORS CONSIDERING MUTUAL INDUCTANCE

By

Han-Kyung Bae

Prof. Krishnan Ramu, Chairman

Electrical and Computer Engineering

(ABSTRACT)

A novel torque control algorithm, which adopts a two-phase excitation, is proposed to improve the performance of the Switched Reluctance Motor (SRM) drive. By exciting two adjacent phases instead of single phase, the changing rate and the magnitude of the phase currents are much reduced. Therefore the existing problems caused by the single-phase excitation such as large torque ripple during commutation, increased audible noise and fatigue of the rotor shaft are mitigated. The electromagnetic torque is efficiently distributed to each phase by the proposed Torque Distribution Function (TDF) that also compensates the effects of mutual coupling. To describe the effects of mutual coupling between phases, a set of voltage and torque equations is newly derived for the two-phase excitation. Parameters of the SRM are obtained by Finite Element Analysis (FEA) and verified by measurements. It is shown that the mutual inductance of two adjacent phases partly contributes to generate the electromagnetic torque and introduces coupling between two adjacent phases in the current or flux linkage control loop, which has been neglected in the single-phase excitation. The dynamics of the current or flux linkage loop are coupled and nonlinear due to the mutual inductance between two adjacent phases and the time varying nature of inductance. Each phase current or flux linkage needs to be controlled precisely to achieve the required performance. A feedback linearizing current controller is proposed to linearize and decouple current control loop along with a gain scheduling scheme to maintain performance of the current control loop regardless of rotor position as well as a feedback linearizing flux linkage controller. Finally, to reduce current or flux linkage ripple, a unipolar switching strategy is proposed. The unipolar switching strategy effectively doubles the

switching frequency without increasing the actual switching frequency of the switches. This contributes to the mitigation of current or flux linkage ripple and hence to the reduction of the torque ripple.

ACKNOWLEDGEMENTS

I would like to thank my advisor, Dr. Krishnan Ramu for his valuable advice on the framework of this dissertation, his continued guidance and support during the completion of the work, and his careful review of the results. Due to his expertise in the SRM, I could start the work in the right direction and complete the work successfully.

I also would like to thank Dr. Nunnally, Dr. Handricks, Dr. Mili, and Dr. Kohler for their assistance and concerns. Their generous encouragement and support throughout the work has been a great source of inspiration.

Most of all, I would like to express deep gratitude to my parents who have provided endless encouragement and support. I also would like to express heartfelt gratitude to my wife, Agnes. Her patience and understanding helped me accomplish this work.

CONTENTS

LIST OF FIGURES

LIST OF TABLES

LIST OF SYMBOLS

θ :	Mechanical angular displacement or rotor position
β_s :	Stator pole arc
β_r :	Rotor pole arc
P_s :	Number of stator poles
P_r :	Number of rotor poles
W_c :	Coenergy
W_f :	Field energy
J :	Moment of inertia
B :	Viscous damping coefficient
$\omega^* (\omega)$:	Commanded (actual) angular speed
$T_e^* (T_e)$:	Commanded (actual) electromagnetic torque
$T_k^* (T_k)$[1]:	Commanded (actual) phase electromagnetic torque
L_k :	Self inductance
L_k' :	Equivalent self inductance
M_{jk} [2]:	Mutual inductance between two adjacent phases
$\frac{\partial L_k}{\partial \theta}$:	Changing rate of self inductance with respect to rotor position
$\frac{\partial M_{jk}}{\partial \theta}$:	Changing rate of mutual inductance with respect to rotor position
$\frac{\partial L_k}{\partial i_k}$:	Changing rate of self inductance with respect to phase current
g_k :	Self torque function
g_{jk} :	Mutual torque function between two adjacent phases

[1] *k=a, b, c, d*
[2] *jk=da, ab, bc, cd*

g'_k:	Modified self torque function
g'_{jk}:	Modified mutual torque function between two adjacent phases
v_k:	Phase voltage
i_k^* (i_k):	Commanded (actual) phase current
λ_k^* (λ_k):	Commanded (actual) phase flux linkage
f_k:	Torque distribution function
H_c:	Current feedback gain
H_f:	Flux linkage feedback gain
K_r:	Converter gain
ω_c:	Current loop bandwidth
ω_f:	Flux linkage loop bandwidth
ζ_c:	Current loop damping ratio
ζ_f:	Flux linkage loop damping ratio
K_{px} (K_{py}):	Proportional gain of the current or flux linkage control loop
K_{ix} (K_{iy}):	Integral gain of the current or flux linkage control loop

CHAPTER 1: INTRODUCTION

The Switched Reluctance Motor (SRM) has been used not only for low performance applications such as fans, pumps and hand-tools but also for high performance applications such as centrifuges, electric vehicles and spindles. The SRM is known to be highly cost-effective and reliable due to its simple structure and the unidirectional operation of its converter. Its rotor is made of steel laminations without magnets and windings, and its stator is also made of steel laminations with short-pitched and concentrated windings as shown in Fig. 1.1. As a result, the manufacturing cost of the SRM is relatively low and it can be operated at very high speed without mechanical problems. In addition, the unidirectional nature of the converter for the SRM provides room for unique and diverse designs such as [1] - [5] and eliminates the problems common in bidirectional converters such as requiring “dead-time” to prevent the shoot-through of upper and lower switches. By connecting switches always in series with a phase winding it is not necessary to add “lock-out” circuitry and in case of a failure, enough time can be provided to shut off the converter to prevent further damage. There is also a greater degree of independence between phases than is possible in other motor drives due to the winding and converter configurations. A fault in one phase in the motor or in the converter generally affects only the flawed phase and other phases can continue to operate independently. Therefore, uninterrupted operation of the motor drive is possible although with reduced power output.

However, because of the double saliency of the SRM, the dynamic equations of the SRM are nonlinear and time varying. It makes it difficult to obtain high performance SRM drives with conventional control schemes. Historically, few in-depth studies of high performance drives for the SRM are currently available in literature. This could be attributed to the fact that the concept of a basic SRM drive has to be acceptable to a broad range of drives industries before the high performance design aspects would become important to dominate the discussion. The former task has been fairly accomplished in the last decade. This has enabled the push for high performance SRM drives which, in turn, places emphasis on their design aspects in the research and development field.

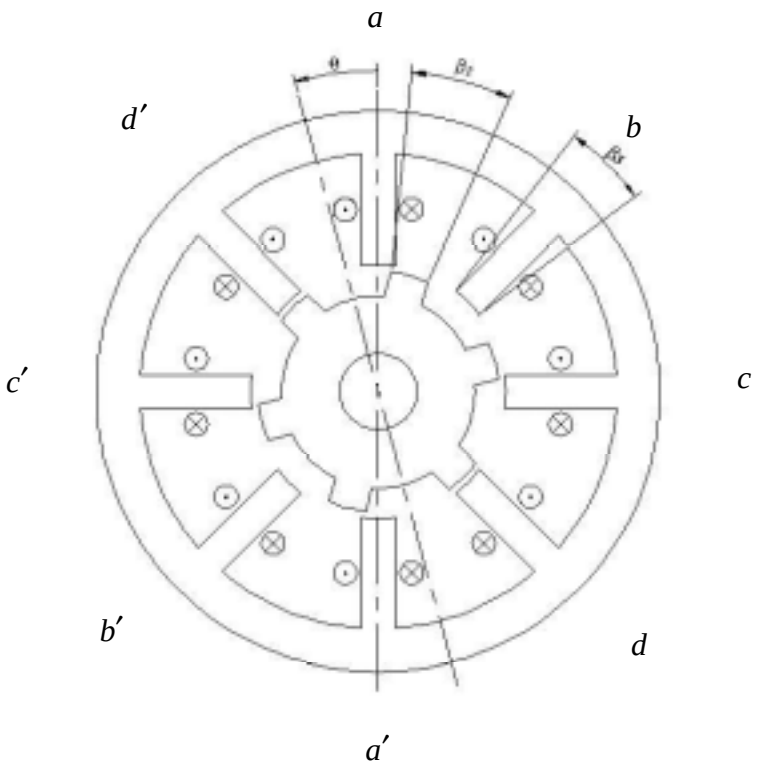

Fig. 1.1 Cross section of the prototype 8/6 SRM

The next section describes the conventional operation of the SRM [6], along with the limitations of this operation. Earlier research activities to improve the performance of the SRM drives, [7] - [21], will be reviewed in the following section. The problems to be solved will be defined after the review, and the scope of this dissertation will be summarized at the end of this chapter.

1.1 Conventional Operation of the SRM

Shown in Fig. 1.2 is an example of an ideal inductance profile of phase *a* for an SRM with 8 stator poles and 6 rotor poles. Conventionally, it is called an 8/6 SRM. It is shown for only 60 mechanical degrees because of its periodicity. Fig. 1.2 portrays an ideal situation while in reality the inductance and torque are nonlinear functions of the current and rotor position. This ideal inductance profile of the SRM is assumed to produce torque in the conventional drives.

The rotor position is defined as the mechanical angle from the polar axis of phase a to one of the interpolar axes of the rotor. At zero degree, the inductance of phase a is the lowest and the interpolar axis of the rotor is aligned with the polar axis of phase a. At the points where inductance is the highest, a set of rotor poles are in full alignment with two opposite stator poles, which composes phase a. If a phase is excited when its inductance is rising, positive torque is produced while negative torque is produced during the falling slope of the inductance. The torque is proportional to the square of the phase current as given in (1.1). Hence, the direction of the current is arbitrary. This unidirectional current requirement has a distinct advantage over other motor drives requiring four-quadrant operational converter, whereas only a two-quadrant operational converter is necessary in the SRM drives.

To move the rotor by 60 degrees in the counter clockwise direction, it takes four phase excitations in the sequence of $a\text{-}b\text{-}c\text{-}d$ and one revolution of the rotor needs six sets of the same sequences. Similarly, four phase excitations in the sequence of $d\text{-}c\text{-}b\text{-}a$ are necessary for the movement of the rotor in the clockwise direction.

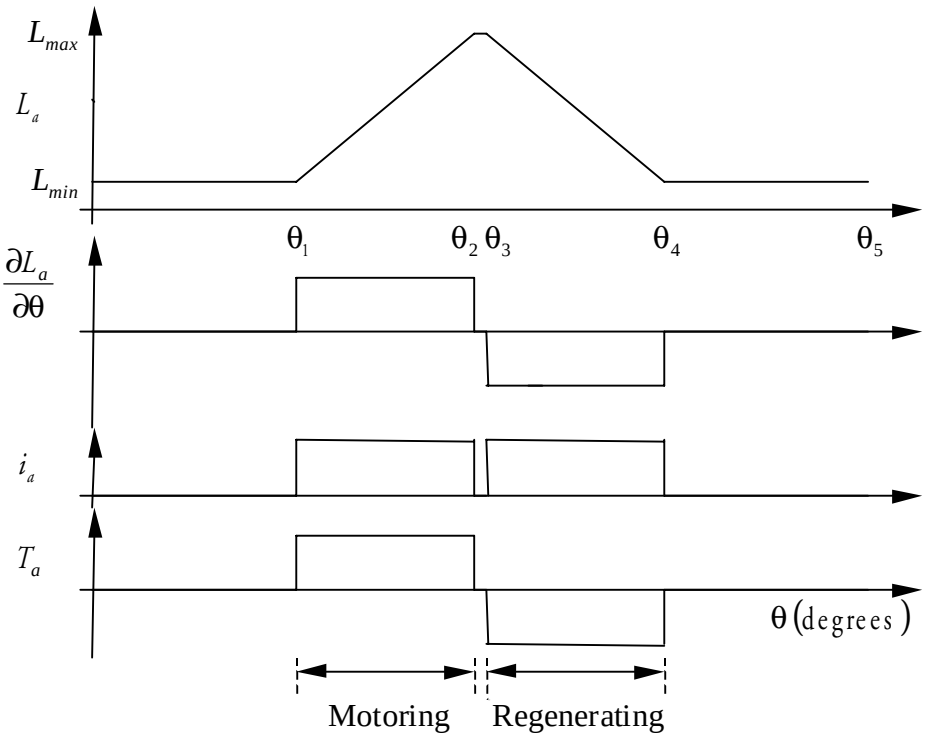

Fig. 1.2 Conventional operation of the SRM

The total output torque generated by this scheme is given in (1.1). It is the sum of the torques produced by the sequentially excited phases.

$$T_e = \sum_{k=a,b,c,d} \frac{1}{2}\frac{\partial L_k}{\partial \theta} i_k^2 \tag{1.1}$$

Where $\partial L_k / \partial \theta$ and i_k are the rate of change of self inductance with respect to rotor position and the phase current, respectively. From the relationship between the self inductance to rotor position shown in Fig. 1.2, the rate of change of self inductance with respect to rotor position can be approximated as a piece-wise linear function such as,

$$\frac{\partial L_a}{\partial \theta} \cong \begin{cases} \dfrac{L_{max} - L_{min}}{\theta_2 - \theta_1} & \text{for } \theta_1 \le \theta < \theta_2 \\ -\dfrac{L_{max} - L_{min}}{\theta_4 - \theta_3} & \text{for } \theta_3 \le \theta < \theta_4 \\ 0 & \textit{elsewhere} \end{cases} \tag{1.2}$$

Here, the relevant defining positions for the prototype SRM are given as follows.

$$\begin{cases} \theta_1 = \dfrac{1}{2}\left\{\dfrac{2\pi}{P_r} - (\beta_s + \beta_r)\right\} = 13^\circ \\ \theta_2 = \theta_1 + \beta_s = 29^\circ \\ \theta_3 = \theta_2 + (\beta_r - \beta_s) = 31^\circ \\ \theta_4 = \theta_3 + \beta_s = 49^\circ \\ \theta_5 = \dfrac{2\pi}{P_r} = 60^\circ \end{cases} \tag{1.3}$$

Where $\beta_s (= 16^\circ)$ and $\beta_r (= 18^\circ)$ are the stator and rotor pole arcs, respectively, and $P_r (= 6)$ is the number of rotor poles. Therefore, the various defining positions are solely determined by the mechanical parameters.

From the torque equation in (1.1), the phase current commands are calculated as,

$$i_k^* = \sqrt{\frac{2T_e^*}{\partial L_k / \partial \theta}} \quad \text{for } k = a,b,c,d \tag{1.4}$$

Only a positive current command is considered to guarantee the unidirectional operation of the converter. If an ideal current control is assumed, *i.e.*, i_k^* is equal to i_k, then the output torque can be controlled as shown in Fig. 1.2.

It is relatively simple to implement this control scheme. However, in an actual machine it is not possible to achieve such an ideal inductance profile. The saturation of magnetic material curves the inductance profile around θ_1, θ_4 and near the top, and the pole-to-pole leakage. The leakage flux plays an important role in determining inductance in the unaligned and partially aligned positions when the stator and rotor poles are not fully overlapping. Furthermore, for rectangular currents, it is observed that torque is produced in a pulsed form resulting in a large torque ripple due to the limited bandwidth of current control loop. Increased audible noise and fatigue of the rotor shaft are drawbacks of this operation. More importantly rectangular currents cannot produce electromagnetic torque without ripple even if zero tracking error is achieved in the current control loop due to the non-ideal inductance profile. With this control scheme, mutual coupling is neglected. Only one phase is excited at a time except during the short commutation period. The torque ripple caused by the mutual coupling is usually small compared with the torque error caused by incorrect current commands and the limited bandwidth of the current control loop.

1.2 State of the Art

In earlier work given in [7] – [8], the aligned inductance L_{max} and the unaligned inductance $L_{\min}$ were analytically estimated and the self inductance was modeled as a piecewise linear function similar to that of Fig. 1.2. All the above methods have considerable error in

predicting the unaligned inductance and they don't provide enough information about inductance at positions in between. Hence, to obtain an actual inductance profile either Finite Element Analysis (FEA) [9] - [15] and or measurements have been adopted.

Based on practical inductance profiles, Schramm *et al.* [16] proposed the phase current optimal profiling in the sense of minimum stator copper loss. The commutation angle θ_c was selected where two adjacent phases would produce the same torque at the same current level assuming that commutation occurs instantaneously. However, due to the finite bandwidth of current control loop, it still generated significant torque ripple during commutation.

To avoid stepwise current or flux linkage commands, several schemes were also proposed in [17] - [21]. Husain *et al.* [17] and Ilic-Spong *et al.* [18] proposed a sinusoidal function and an exponential function as a torque distribution function, respectively. The basic idea was to distribute the desired torque to two adjacent phases during predetermined commutation interval using the torque distribution function. By assuming an ideal inductance profile, however, incorrect current commands caused torque error and by choosing a short commutation interval the rates of change of currents or flux linkages could not be much reduced. On the other hand, Wallace *et al.* [19] linearly decreased the outgoing phase current and increased the incoming phase current during commutation accepting possible torque error. Kim *et al.* [20] proposed a torque distribution function, which could minimize the rates of change of currents over the commutation interval.

In some of these control schemes, ideal inductance profiles were assumed and more importantly all of them didn't consider the effects of the mutual inductance during commutation. The effects of the mutual inductance were mentioned in [14] and [15] but a controller to compensate the effects was not proposed. The possibility of two-phase excitation was shown in [21] but it also only mentioned the effects of mutual coupling without suggesting any active control scheme to overcome the effects. In some applications, the torque ripple caused by the mutual inductance may not be acceptable. Therefore, the effect of mutual coupling should be analyzed to decide whether it is negligible or not.

Torque controllers in these references assumed high performance current control that can track current command with desirable tracking error. High gain current controller and hysteresis current controller were frequently used but they had inherent drawbacks such as high switching loss and noise. If faster switching devices are used in order to mitigate these drawbacks, the cost of the control system will be increased dramatically. On the other hand, due to the fact that the stator inductance changes according to rotor position from L_{min} to L_{max} or vice versa and the fact that the current control loop is highly nonlinear and closely coupled, it is not possible to obtain high performance with a conventional PWM current controller.

1.3 Scope

The review in the previous sections provides insight into the development of the different control schemes for the SRM and their advantages and limitations for different applications. Based on this review, the following are identified as the key objectives to be achieved in this dissertation for high performance SRM drives.

1) Identification of parameters and suitable modeling of the SRM for multi-phase excitation.

2) A simple and effective torque distribution function to reduce the rate of change and the peak value of the phase current or flux linkage commands without torque ripple.

3) A high performance current or flux linkage controller to track the commands with desirable accuracy.

4) Selection of a converter and a switching strategy for the converter.

5) Verification of the proposed control algorithms by simulation and experimental results.

6) Application of the above objectives to a prototype Linear Switched Reluctance Motor (LSRM).

This dissertation is organized as follows. Chapter 2 introduces a novel modeling of the SRM, which is suitable for two-phase excitation and which also takes into account the mutual inductance. Parameters for this modeling are obtained by FEA and verified by measurements. Chapter 3 describes a new torque distribution function for two-phase excitation, which substantially reduces the rates of change of the phase currents or flux linkages and which also compensates the effect of the mutual inductance. Chapter 4 presents torque control algorithms based on the phase currents and flux linkages, respectively. For the phase current control, a feedback linearizing current controller, which linearizes and decouples the current control loop, and a gain scheduling, which adapts gains of current controller according to the change of phase inductances, are proposed. An alternate torque control based on the phase flux linkages is also introduced in this chapter. By a feedback linearization, flux linkage controller gains become independent of the phase inductances. Operation of the SRM including magnetic saturation is given in Chapter 5. Chapter 6 deals with a unipolar switching strategy for the SRM proposed by the author in [24] and [29], which reduces the phase current ripple and doubles the effective switching frequency. Simulation and experimental results for both the rotary and linear SRMs are included in Chapter 7. Conclusions are summarized in Chapter 8. Appendix A describes the application of the proposed torque control algorithm to the LSRM and the structure of the converter for the LSRM. Appendix B describes the derivation of the proportional and integral gains of the system and Appendix C gives the specifications of the prototype SRM used in the dissertation.

CHAPTER 2: MODELING OF THE SRM INCLUDING MUTUAL INDUCTANCE

In the conventional operation of the SRM, ideal inductance profiles, which are not practically achievable, are assumed. The identification of actual parameters in a system is essential in designing a high performance controller. In this chapter, parameters such as self inductances, mutual inductances and the rates of change of the inductances with respect to rotor position are obtained by Finite Element Analysis (FEA). A commercially available software package FLUX2D® of Magsoft Corp. was used in FEA [31] - [32]. The results of this analysis are given without a detailed description because the finite element method is beyond the scope of this research. To verify this analysis, measurements were performed and parameters obtained by both methods were compared.

All parameters are functions of rotor position only if the SRM operates in a magnetically linear region. If the SRM operates in a magnetically saturated region, the parameters become functions of phase currents as well as rotor position. Therefore, when the operation in the entire region is considered, the parameters should be expressed in terms of phase currents and rotor position. On the other hand, in many linear motor drive applications such as [29] - [30], the SRM operates only in magnetically linear region. In this chapter and following two chapters, the analysis of the SRM and the design of its drives are performed assuming a linear magnetic system. The operation of the SRM including magnetic saturation will be described separately in Chapter 5.

From the geometry of the SRM shown in Fig. 1.1, several fundamental properties of parameters are derived to gain some insight into the design of the SRM drives. From these properties, the possibility of two-phase excitation and the necessity of considering the effects of mutual coupling can be found. Conventionally, only one phase was considered at a time when the voltage and torque equations were derived. However, the effects of mutual coupling could not be included with these equations. Therefore, two adjacent phases should be considered

simultaneously. The dynamic equations of the SRM for two-phase excitation that includes the effects of mutual inductances are derived. Two different dynamic equations in terms of phase current and flux linkages are derived and compared to examine the merits and demerits of their use.

Section 2.1 describes the identification of parameters by FEA in the linear magnetic region. The self inductances, mutual inductances and the rates of change of self and mutual inductances with respect to rotor position are obtained. Section 2.2 verifies the FEA results with experimental measurements over the entire operating region. Section 2.3 describes the voltage equations for two-phase excitation both in terms of phase currents and flux linkages. The torque equations for two-phase excitation both in terms of phase currents and flux linkages are described in Section 2.4.

2.1 Parameters by FEA

The prototype SRM is not saturated when the output torque is less than 0.2 N·m or the phase current is less than 1.2 A. Therefore, all parameters in the linear magnetic region are obtained when corresponding phase currents are equal to 1.2 A. For notational simplicity, some frequently referred variables are redefined. The rates of change of self and mutual inductances with respect to rotor position are defined as “the self torque functions” and “the mutual torque functions”, respectively. They are denoted as follows.

$$\begin{aligned} g_k(\theta) &\equiv \frac{\partial L_k(\theta)}{\partial \theta} \quad \text{for } k = a, b, c, d \\ g_{jk}(\theta) &\equiv \frac{\partial M_{jk}(\theta)}{\partial \theta} \quad \text{for } jk = da, ab, bc, cd \end{aligned} \tag{2.1}$$

The self inductances and mutual inductances of the prototype SRM are shown in Fig. 2.1. From the geometry of the prototype SRM, it should be noticed that all parameters have a period of 60° and there is a phase shift of 15° between adjacent phases.

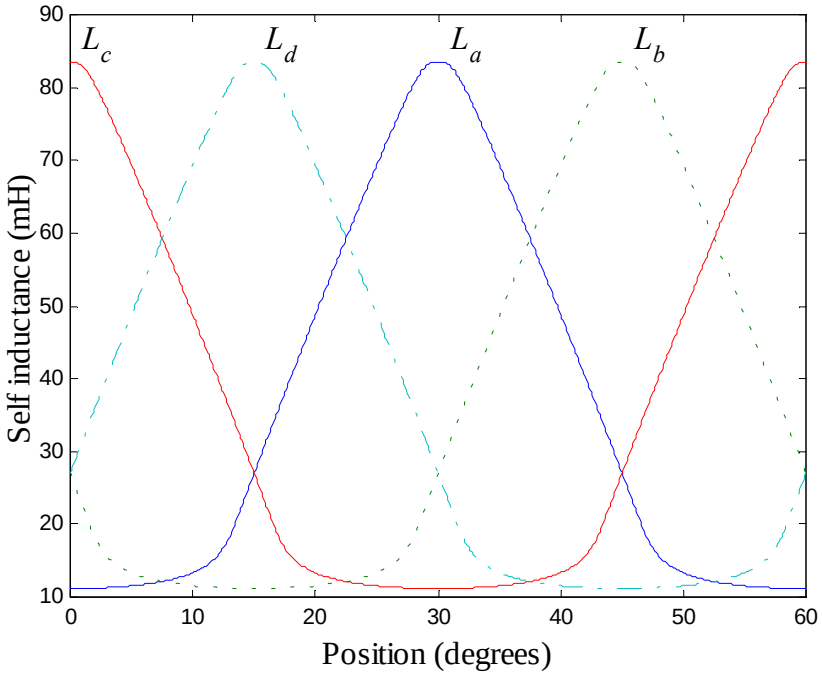

(a) Self inductances

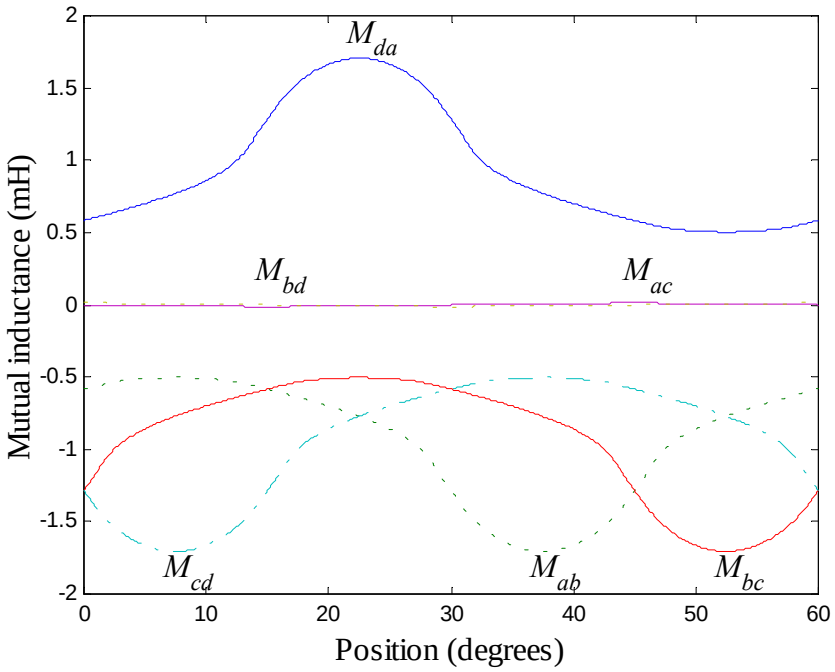

(b) Mutual inductances

Fig. 2.1 Inductances of the prototype SRM

During half of the period, the self inductance of a phase is monotonously increasing and during the other half of the period it is monotonously decreasing. In other words, a phase can produce useful torque during half of the period. The magnitude of the self inductance at the aligned position is about 7.5 times larger than the magnitude of the self inductance at the unaligned position. This causes difficulties in controlling phase currents or flux linkages. As illustrated in Fig. 2.1(b), the mutual inductance between two adjacent phases is not more than 6.4% of the related self inductances and the mutual inductance between non-adjacent phases is not more than 0.07% of the related self inductances at any rotor position. Therefore, the mutual inductance between non-adjacent phases is negligible although they may be used to detect rotor position in a sensorless control system such as in [22]. Important properties of the self and mutual inductance are summarized as,

Property I:

$$\begin{array}{lll} L_b(\theta) = L_a(\theta - 15^\circ) & L_c(\theta) = L_a(\theta - 30^\circ) & L_d(\theta) = L_a(\theta - 45^\circ) \\ M_{ab}(\theta) = -M_{da}(\theta - 15^\circ) & M_{bc}(\theta) = -M_{da}(\theta - 30^\circ) & M_{cd}(\theta) = -M_{da}(\theta - 45^\circ) \end{array} \tag{2.2}$$

$$\begin{array}{lll} g_b(\theta) = g_a(\theta - 15^\circ) & g_c(\theta) = g_a(\theta - 30^\circ) & g_d(\theta) = g_a(\theta - 45^\circ) \\ g_{ab}(\theta) = -g_{da}(\theta - 15^\circ) & g_{bc}(\theta) = -g_{da}(\theta - 30^\circ) & g_{cd}(\theta) = -g_{da}(\theta - 45^\circ) \end{array} \tag{2.3}$$

$$\begin{array}{ll} g_a(\theta) \geq 0 \text{ for } 0^\circ \leq \theta < 30^\circ & \text{for } g_a(0^\circ) = 0 \\ g_a(\theta) \leq 0 \text{ for } 30^\circ \leq \theta < 60^\circ & \text{for } g_a(30^\circ) = 0 \end{array} \tag{2.4}$$

It also should be noted that the mutual coupling between phases *d* and *a* is additive and other mutual couplings are subtractive. It can be explained from the winding configuration of the prototype SRM shown in Fig. 1.1. The stator windings of phases *d* and *a* are wound such that when both phase currents flow in the same direction the flux linkages are additive unlike other phases. It is possible to make the effects of the mutual couplings positive by appropriately selecting the directions of the related phase currents if a four-quadrant operational converter is used. This will decrease the peak of the related phase currents. By carefully examining property I given in (2.2) - (2.4) and the torque functions shown in Fig. 2.2, the following can be deduced.

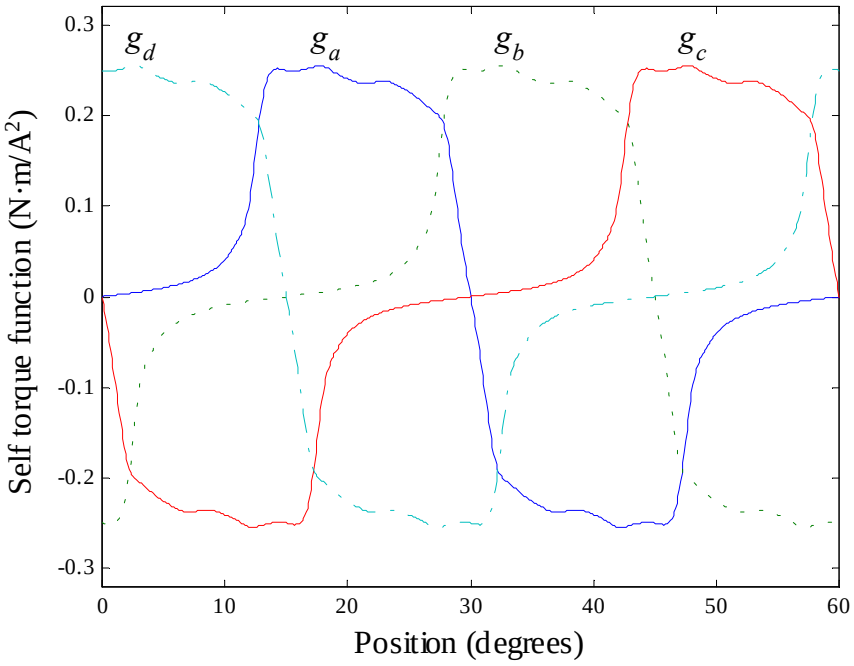

(a) Self torque functions

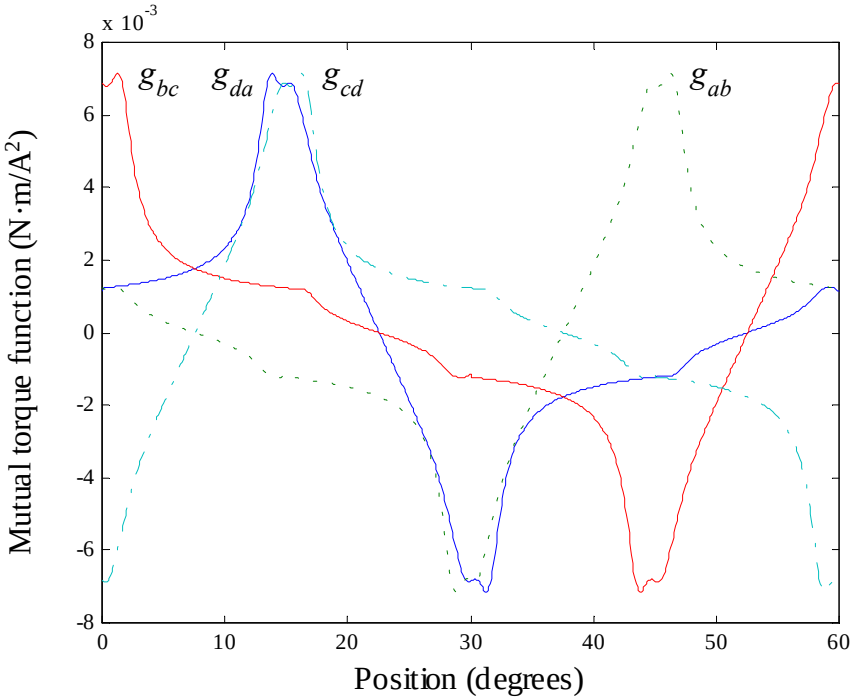

(b) Mutual torque functions

Fig. 2.2 Torque functions of the prototype SRM

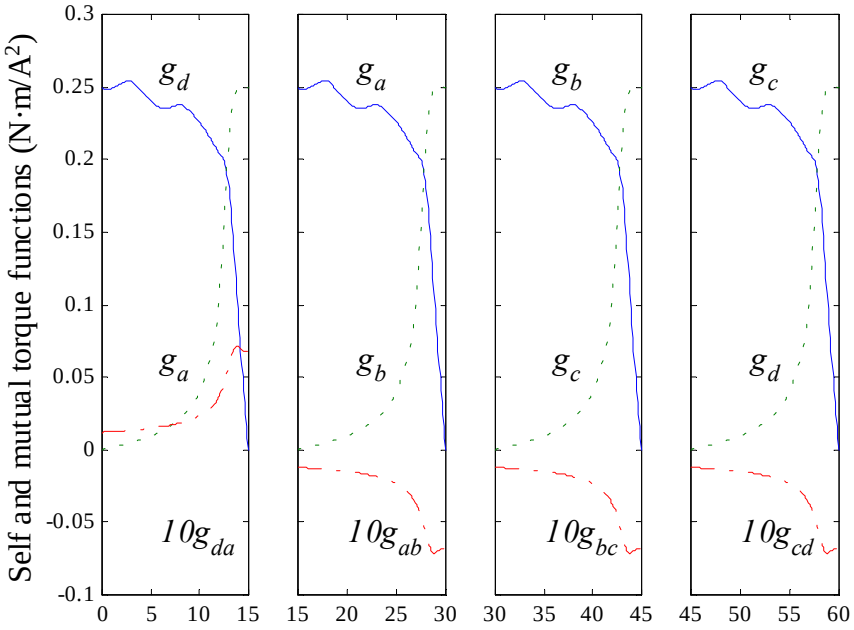

(a) $T_e \geq 0$

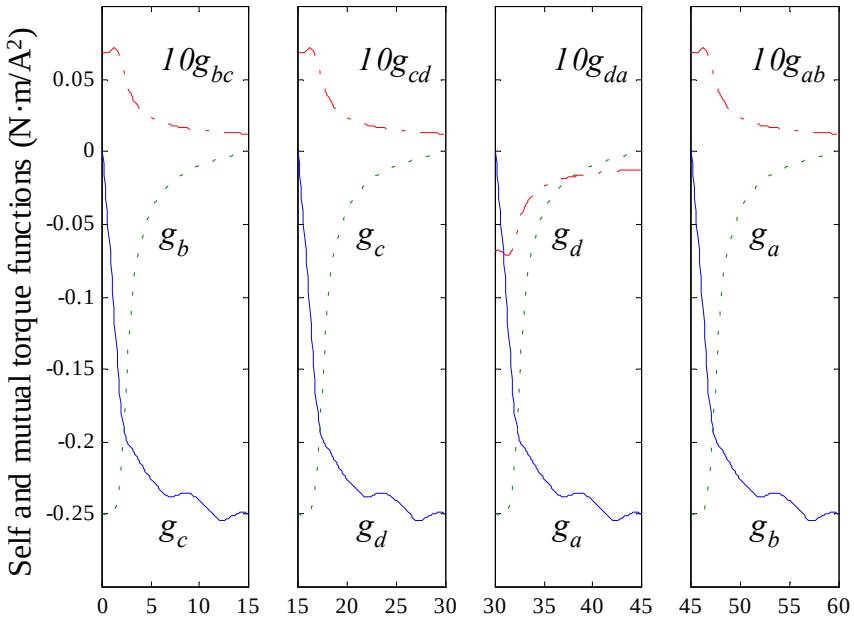

(b) $T_e < 0$

Fig. 2.3 Considered torque functions in each region.

Two adjacent phases can contribute to generate the desired output torque during an interval of 15° because the polarities of the self torque functions are identical during the interval. This interval is defined as the excitation region. There are four different excitation regions in a period for an 8/6 SRM and only two phases are useful in an excitation region. For example, phases *d* and *a* or phases *b* and *c* are useful when the sign of the required output torque is positive or negative, respectively. Exciting two phases simultaneously will be advantageous in terms of reducing the overall ripple torque as well as reducing the peak values of the phase currents. In addition, it can be noticed that the mutual coupling between the phases is not negligible. This implies the importance of considering the effects of mutual coupling while designing a high-performance SRM controller.

In Fig. 2.3, the considered torque functions in each region are redrawn from Fig. 2.2. The mutual torque functions are magnified ten times for easier comparison. The waveforms of the corresponding self torque functions in four regions at the same torque are equal. However, the waveforms of the mutual torque functions in the first region when T_e is positive and the third region when T_e is negative are different from the waveforms of the mutual torque functions in other excitation regions because only the mutual coupling between phases d and a are additive. A four-phase system can be considered as a two-phase system because only one excitation region is considered at a time. Now, the dynamic equations suitable for two-phase excitation can be derived.

2.2 Verification of Parameters by Measurements

To verify the results obtained by FEA, inductances of the prototype SRM have been measured. Due to mechanical symmetry of the prototype SRM, only the self inductance of phase *a*, L_a and the mutual inductance between phase *a* and *d*, M_{da} have been measured and compared with the results of FEA. When the SRM is operated in the saturation region, both inductances are dependent on the phase current as well as rotor position. Thus, the measurements of inductances

have been performed by the flux linkage method by measuring phase current and voltage [28]. The results of FEA in the saturation region are given in Chapter 5.

Decaying current instead of rising current has been measured to avoid oscillation due to the LC circuit formed by the dc link capacitor and the winding inductance. The flux linkage method is based on the voltage equations of the SRM. When $i_d = 0$, they are given by,

$$\begin{aligned} v_a &= R_s i_a + \frac{d\lambda_a}{dt} \\ v_d &= \frac{d\lambda_d}{dt} \end{aligned} \tag{2.5}$$

where,

$$\begin{aligned} \lambda_a &= L_a i_a \\ \lambda_d &= M_{da} i_a \end{aligned} \tag{2.6}$$

From (2.5), the instantaneous flux linkages are obtained as,

$$\begin{aligned} \lambda_a(t) - \lambda_a(0) &= \int_0^t (v_a(\tau) - R_s i_a(\tau))d\tau \\ \lambda_d(t) - \lambda_d(0) &= \int_0^t v_d(\tau)d\tau \end{aligned} \tag{2.7}$$

$\lambda_a(0)$ and $\lambda_d(0)$ are the flux linkages at $t = 0$, respectively. Therefore, the flux linkages at any instant can be obtained from the measurements of the phase current and voltage provided that the resistance per phase is known. From the obtained flux linkages, inductances are calculated as,

$$\begin{aligned} L_a(t) &= \frac{\lambda_a(t) - \lambda_a(0)}{i_a(t)} \\ M_{da}(t) &= \frac{\lambda_d(t) - \lambda_d(0)}{i_a(t)} \end{aligned} \tag{2.8}$$

Experimental setup for the inductance measurements is shown in Fig. 2.4. Phase current and voltage are measured simultaneously through a data acquisition system. A digital storage scope is used to acquire data with the sampling time of 5 ms. Numerical integration of the acquired data was then performed to obtain phase flux linkages. The measurement sequence is as follows. The rotor is fixed to the desired position by mechanical means and then a steady DC current is established in the winding by turning on the switch T_m and adjusting the variable AC source. To measure L_a, 30 steps of 1 degree are used. The decaying current and the voltage drop across phase *a* winding at the selected positions are sampled at the same time right after turning off the switch T_m. The freewheeling diode D_m, which provides a path for the energy stored in the winding when the phase winding is disconnected from the source, has to be fast enough to minimize the recovery time. The magnitude of the voltage drop across the phase winding during the measurement period is equal to the magnitude of the forward voltage drop of the diode D_m. In addition, to measure M_{da}, 24 steps of 2.5 degrees are used and the decaying current and the voltage drop across the phase *d* winding are also sampled at each position. Numerical calculations represented by (2.7) and (2.8) were performed in a personal computer. Fig. 2.5 shows the predicted and measured inductances at the selected positions and at $i_a = 1.2$ A and 2.0 A. Numerical values at representative positions are listed in Table 2.1.

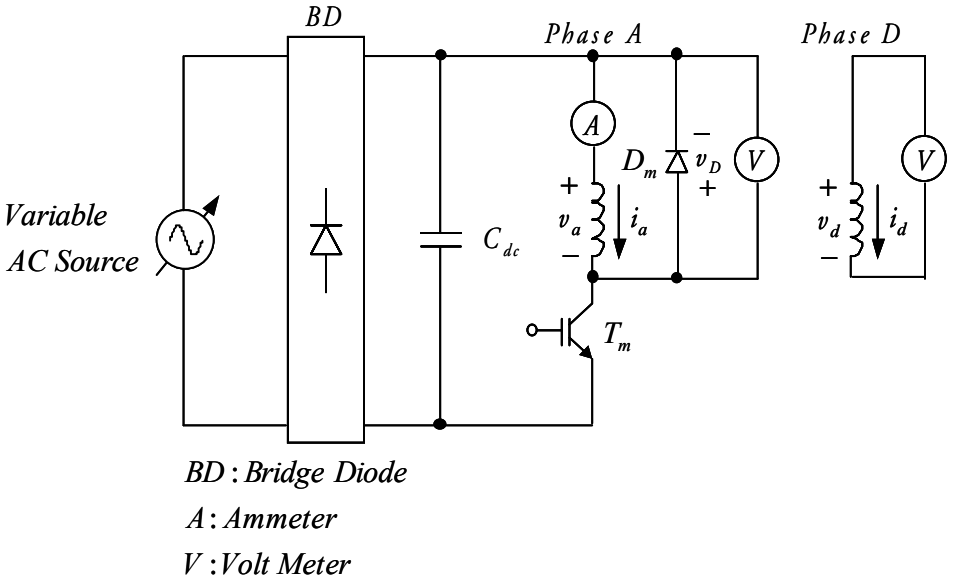

Fig. 2.4 Experimental setup for the inductance measurements

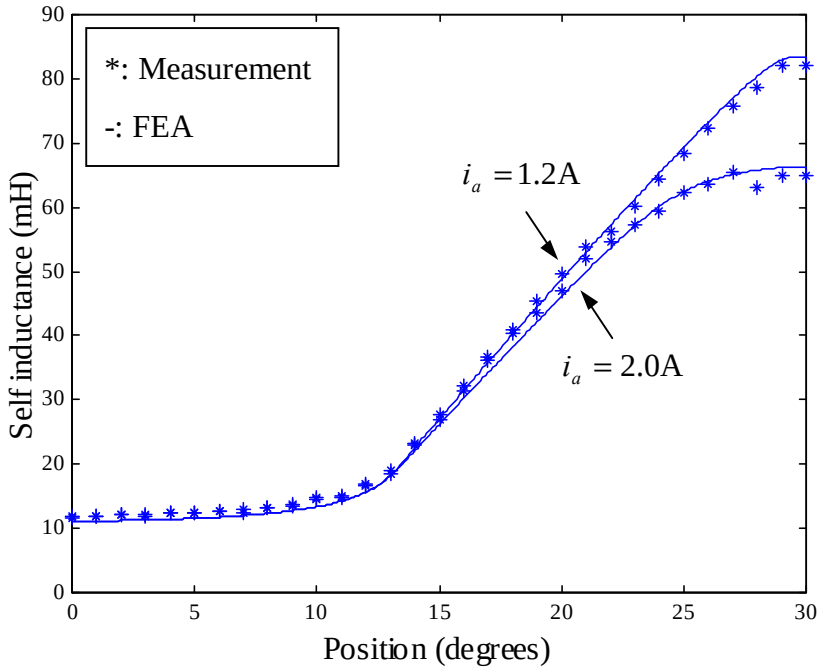

(a) Self inductance

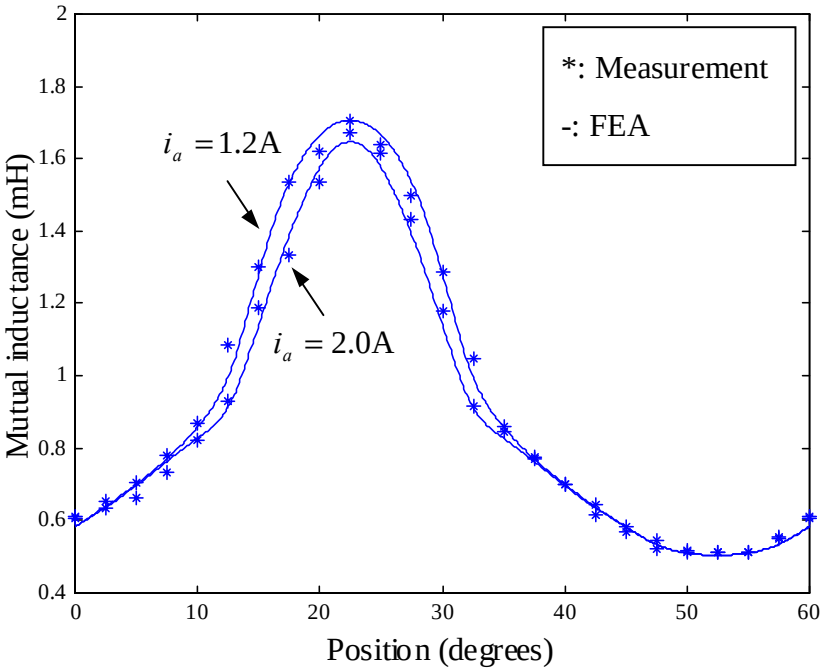

(b) Mutual inductance

Fig. 2.5 Comparison of measured and predicted inductances

TABLE 2.1 Comparison of inductance values

Inductance (mH)	i_a =1.2 A		i_a =2.0 A	
	FEA	Measurement	FEA	Measurement
$L_{a,max}$	83.5	82.0	66.3	65.0
$L_{a,min}$	11.2	12.0	11.2	11.6
$M_{da,max}$	1.71	1.72	1.64	1.67
$M_{da,min}$	0.504	0.511	0.504	0.508

Measurements by the flux linkage method are in very close agreement with the FEA results. The accuracy of the measurements depends on the measurement technique and instrumentation. Deviations are mainly caused by the insufficient resolution of the data acquisition system and the poor signal to noise ratio. The resolution of the digital storage oscilloscope used in these measurements is 8-bit and the gain of the isolation amplifier is 0.05. As a result, there are small errors in these measurements.

2.3 Voltage Equations for Two-Phase Excitation

If the mutual inductances between non-adjacent phases, M_{ac} and M_{bd} are neglected, the voltage and flux linkage equations for four-phase SRM can be expressed in terms of both phase currents and flux linkages as follows.

$$\begin{aligned} v_a &= R_s i_a + \frac{d\lambda_a}{dt} \\ v_b &= R_s i_b + \frac{d\lambda_b}{dt} \\ v_c &= R_s i_c + \frac{d\lambda_c}{dt} \\ v_d &= R_s i_d + \frac{d\lambda_d}{dt} \end{aligned} \tag{2.9}$$

and

$$\begin{aligned}
\lambda_a &= L_a i_a + M_{ab} i_b + M_{da} i_d \\
\lambda_b &= M_{ab} i_a + L_b i_b + M_{bc} i_c \\
\lambda_c &= M_{bc} i_b + L_c i_c + M_{cd} i_d \\
\lambda_d &= M_{da} i_a + M_{cd} i_c + L_d i_d
\end{aligned} \tag{2.10}$$

Where R_s is the winding resistance of a phase, and v_k and λ_k for $k = a, b, c, \text{and } d$ are the phase voltage and flux linkage, respectively.

If two adjacent phases are considered at a time and the phase currents of other two phases are assumed to be zero, then four-phase equation (2.10) can be simplified as follows.

$$\begin{aligned}
v_x &= R_s i_x + \frac{d\lambda_x}{dt} \\
v_y &= R_s i_y + \frac{d\lambda_y}{dt}
\end{aligned} \tag{2.11}$$

and

$$\begin{aligned}
\lambda_x &= L_x i_x + M_{xy} i_y \\
\lambda_y &= M_{xy} i_x + L_y i_y
\end{aligned} \tag{2.12}$$

Where the subscript x are y are the phases in consideration and the set (x, y) is one of (a,b), (b,c), (c,d), and (d,a). Either phase x or phase y is leading and the other phase is following according to the direction of rotation. For example, phase d is leading phase a in the first excitation region when the output torque and the velocity are positive.

Voltage equations in terms of phase currents

The voltage equations can be expressed in terms of either phase currents or flux linkages. In this subsection, phase currents are chosen as state variables. Differentiating (2.12) with respect to time *t* yields,

$$\frac{d\lambda_x}{dt} = L_x \frac{di_x}{dt} + g_x \omega i_x + M_{xy} \frac{di_y}{dt} + g_{xy} \omega i_y$$
$$\frac{d\lambda_y}{dt} = M_{xy} \frac{di_x}{dt} + g_{xy} \omega i_x + L_y \frac{di_y}{dt} + g_y \omega i_y \tag{2.13}$$

Where $\omega = d\theta / dt$ and g_x, g_y, and g_{xy} are the torque functions defined in (2.1). Hence, substituting (2.13) into (2.11) and rearranging they yield,

$$\frac{di_x}{dt} = -a_1 i_x - a_2 \omega i_x + a_3 i_y + a_4 \omega i_y + a_0 \left(v_x - \frac{M_{xy}}{L_y} v_y \right)$$
$$\frac{di_y}{dt} = -b_1 i_y - b_2 \omega i_y + b_3 i_x + b_4 \omega i_x + b_0 \left(-\frac{M_{xy}}{L_x} v_x + v_y \right) \tag{2.14}$$

where,

$$D = L_x L_y - M_{xy}^2 \tag{2.15}$$

$$a_0 = \frac{L_y}{D} \qquad b_0 = \frac{L_x}{D}$$

$$a_1 = a_0 R_s \qquad b_1 = b_0 R_s$$

$$a_2 = a_0 \left(\frac{\partial L_x}{\partial \theta} - \frac{M_{xy}}{L_y} \cdot \frac{\partial M_{xy}}{\partial \theta} \right) \quad b_2 = b_0 \left(\frac{\partial L_y}{\partial \theta} - \frac{M_{xy}}{L_x} \cdot \frac{\partial M_{xy}}{\partial \theta} \right)$$
$$a_3 = a_0 \frac{M_{xy} R_s}{L_y} \qquad b_3 = b_0 \frac{M_{xy} R_s}{L_x} \tag{2.16}$$
$$a_4 = a_0 \left(\frac{M_{xy}}{L_y} \cdot \frac{\partial L_y}{\partial \theta} - \frac{\partial M_{xy}}{\partial \theta} \right) \quad b_4 = b_0 \left(\frac{M_{xy}}{L_x} \cdot \frac{\partial L_x}{\partial \theta} - \frac{\partial M_{xy}}{\partial \theta} \right)$$

It can be noticed that there are two nonlinear back EMF terms and one coupling term in each equation in (2.14) and the phase currents are affected not only by the associated phase input but also by the other phase input. Therefore, states should be linearized and decoupled and inputs also should be decoupled to design a high-performance current controller. It is the main disadvantage of choosing the phase currents as state variables. When the phase flux linkages are chosen as state variables, only states need to be decoupled as explained in the next subsection.

Voltage equations in terms of phase flux linkages

Phase flux linkages are now chosen as state variables assuming they are obtainable through either direct measurement or indirect estimation. Rearranging (2.12) yields,

$$\begin{aligned} i_x &= \frac{L_y}{D}\lambda_x - \frac{M_{xy}}{D}\lambda_y \\ i_y &= -\frac{M_{xy}}{D}\lambda_x + \frac{L_x}{D}\lambda_y \end{aligned} \tag{2.17}$$

Substituting (2.17) into (2.11) yields,

$$\begin{aligned} \frac{d\lambda_x}{dt} &= -c_1\lambda_x + c_2\lambda_y + v_x \\ \frac{d\lambda_y}{dt} &= -d_1\lambda_y + d_2\lambda_x + v_y \end{aligned} \tag{2.18}$$

where,

$$\begin{aligned} c_1 &= \frac{L_y}{D}R_s \qquad d_1 = \frac{L_x}{D}R_s \\ c_2 &= \frac{M_{xy}}{D}R_s \quad d_2 = \frac{M_{xy}}{D}R_s \end{aligned} \tag{2.19}$$

Unlike the voltage equations in terms of phase currents given in (2.14), the voltage equations in terms of phase flux linkages given in (2.18) have only coupling terms that can be easily removed and the inputs are no longer coupled. This is the main advantage of choosing the phase flux linkages as state variables.

2.4 Torque Equation for Two-Phase Excitation

Similarly, either phase currents or phase flux linkages can be assigned as state variables to express the output torque equation.

Torque equation in terms of phase currents

To express the output torque in terms of phase currents and rotor position, the output torque equation is derived from the coenergy W_c. From the definition of the coenergy and the relationship given in (2.12), the differential coenergy is expressed as [23],

$$\begin{aligned} dW_c(i_x, i_y, \theta) &= \lambda_x di_x + \lambda_y di_y + T_e d\theta \\ &= (L_x i_x + M_{xy} i_y) di_x + (M_{xy} i_x + L_y i_y) di_y + T_e d\theta \end{aligned} \tag{2.20}$$

The coenergy can be found by integrating (2.20) along a path of integration. The most convenient integration path is to integrate over θ holding i_x and i_y fixed at zero, integrate over i_y by holding i_x fixed at zero, and finally integrate over i_x as shown in Fig. 2.6. In the first part of the integration, the integral is zero because T_e is zero when both i_x and i_y are zeros. Thus, the coenergy is calculated as,

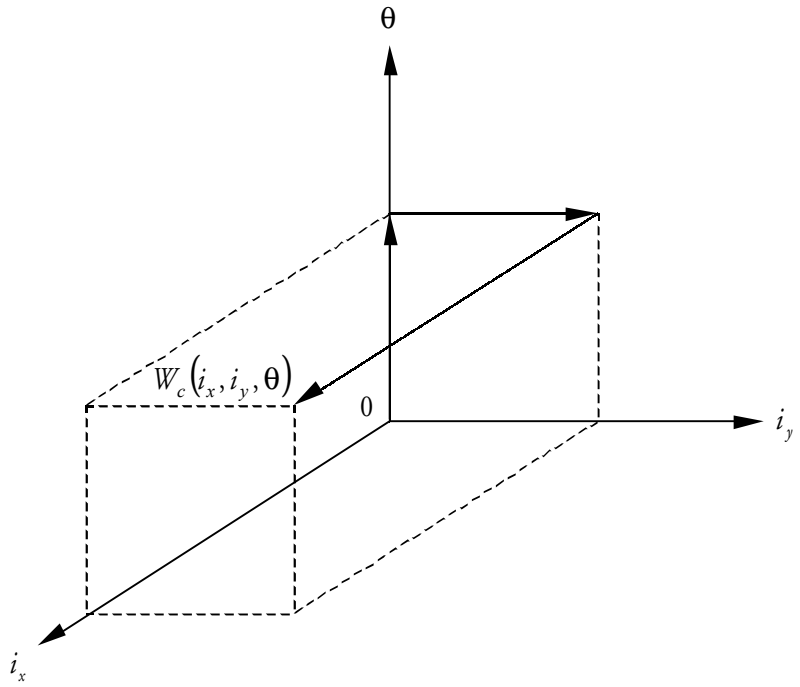

Fig. 2.6 Integration path to obtain $W_c(i_x, i_y, \theta)$

$$
\begin{aligned}
W_c(i_x, i_y, \theta) &= \int_0^{i_y} \lambda_y(0, \xi, \theta) d\xi + \int_0^{i_x} \lambda_x(\xi, i_y, \theta) d\xi \\
&= \int_0^{i_y} L_y \xi d\xi + \int_0^{i_x} (L_x \xi + M_{xy} i_y) d\xi \\
&= \frac{1}{2} L_x i_x^2 + \frac{1}{2} L_y i_y^2 + M_{xy} i_x i_y
\end{aligned} \tag{2.21}
$$

Where ξ is an integration variable. Then, T_e is calculated as,

$$
T_e = \left. \frac{\partial W_c(i_x, i_y, \theta)}{\partial \theta} \right|_{i_x, i_y \text{ fixed}} = \frac{1}{2} g_x i_x^2 + \frac{1}{2} g_y i_y^2 + g_{xy} i_x i_y \tag{2.22}
$$

Now T_e is expressed in terms of state variables, i_x, i_y, and θ. The effect of mutual inductance is represented by the third term in (2.22).

Torque equation in terms of phase flux linkages

The output torque can be obtained from the field energy W_f to express the output torque equation in terms of phase flux linkages and rotor position. Alternatively, the output torque can be derived from the relationship between the phase currents and flux linkages. Substituting (2.17) into (2.22) yields,

$$
\begin{aligned}
T_e = & \frac{1}{2D^2} (L_y^2 g_x + M_{xy}^2 g_y - 2 M_{xy} L_y g_{xy}) \lambda_x^2 \\
& + \frac{1}{2D^2} (M_{xy}^2 g_x + L_x^2 g_y - 2 M_{xy} L_x g_{xy}) \lambda_x^2 \\
& + \frac{1}{D^2} \{ - M_{xy} L_y g_x - M_{xy} L_x g_y + (L_x L_y + M_{xy}^2) g_{xy} \} \lambda_x \lambda_y
\end{aligned} \tag{2.23}
$$

The dynamic equations governing the behavior of the SRM in terms of phase currents and in terms of phase flux linkages are summarized in (2.24) and (2.25), respectively.

Dynamic Equation I:

$$\begin{aligned}
\frac{di_x}{dt} &= -a_1 i_x - a_2 \omega i_x + a_3 i_y + a_4 \omega i_y + a_0 \left(v_x - \frac{M_{xy}}{L_y} v_y \right) \\
\frac{di_y}{dt} &= b_1 i_x + b_2 \omega i_x - b_3 i_y - b_4 \omega i_y + b_0 \left(-\frac{M_{xy}}{L_x} v_x + v_y \right) \\
\frac{d\omega}{dt} &= -\frac{B}{J}\omega + \frac{1}{J}\left(\frac{1}{2} g_x i_x^2 + \frac{1}{2} g_y i_y^2 + g_{xy} i_x i_y \right)
\end{aligned} \tag{2.24}$$

Dynamic Equation II:

$$\begin{aligned}
\frac{d\lambda_x}{dt} &= -c_1 \lambda_x + c_2 \lambda_y + v_x \\
\frac{d\lambda_y}{dt} &= -d_1 \lambda_y + d_2 \lambda_x + v_y \\
\frac{d\omega}{dt} &= -\frac{B}{J}\omega + \frac{1}{J}\left[\frac{1}{2D^2}\left(L_y^2 g_x + M_{xy}^2 g_y - 2M_{xy} L_y g_{xy} \right)\lambda_x^2 \right. \\
&\quad + \frac{1}{2D^2}\left(M_{xy}^2 g_x + L_x^2 g_y - 2M_{xy} L_x g_{xy} \right)\lambda_x^2 \\
&\quad \left. + \frac{1}{D^2}\left\{ -M_{xy} L_y g_x - M_{xy} L_x g_y + \left(L_x L_y + M_{xy}^2 \right) g_{xy} \right\}\lambda_x \lambda_y \right]
\end{aligned} \tag{2.25}$$

Where J and B are the moment of inertia and the viscous damping coefficient of the SRM and load, respectively.

The voltage equations given in (2.18) have some advantages over the equations given in (2.14). The voltage equations in terms of phase currents are relatively complex. Especially, the back EMF terms such as the second and the fourth terms in right hand side of (2.14) should be taken care of at high speed. The voltage equations in terms of phase flux linkages do not have the back EMF terms and the coefficients are simpler. However, the accessibility of the phase flux linkages should be guaranteed by some means. One way of obtaining flux linkage feedback is

using the relationship given in (2.12) if phase currents are already available and parameters are well known. The torque equation in terms of the phase currents, however, is relatively simple. As a result, it will be used to derive the torque distribution functions described in the following chapter.

CHAPTER 3: TORQUE DISTRIBUTION FUNCTION

Conventionally, the SRM has been operated with step-wise phase currents. The electromagnetic torque of the SRM depends on phase currents and rotor position, which when operated with step-wise currents results in significant torque ripple. The commutation process is another cause of torque ripple. To obtain higher performance and efficiency, the commutation angles must be carefully chosen based on speed and torque, and the duration of the commutation period becomes more important as speed increases. Consequently, this form of control that produces an average torque output is not effective for high performance operation. To achieve a high bandwidth torque control in applications that require good transient performance, it is necessary to employ instantaneous torque control. Conventional commutation has to be replaced by a control scheme that profiles the phase currents or flux linkages to produce the desired total motor torque by coordinating the torque produced by individual phases. If the individual phase currents or flux linkages can be controlled with a high bandwidth, then choosing the appropriate current or flux linkage waveforms will guarantee low torque ripple.

After a brief review of previous work, a new torque control strategy that efficiently utilizes all useful phases and considers the mutual coupling is introduced. In the following description, an SRM with 8 stator poles and 6 rotor poles (8/6) is assumed. The proposed torque control strategy, however, can be applied to differently configured machines such as a 6/4 SRM with slight modification as described at Appendix A [29].

Property I given in (2.2) - (2.4) shows that at any position two adjacent phases contribute to generate desired torque and the excitation interval of a phase can be broadened to 30 degrees while it is 15 degrees in conventional drives. As a result, if precise current or flux linkage control is assumed, torque control implies the distribution of the desired torque to each phase and the generation of phase currents or flux linkages from the distributed torque. Considering several feasible performance indices, a novel Torque Distribution Function (TDF) is proposed. In the first step, the effects of mutual inductance are neglected to clarify the notion of the TDF and in

the second step, the effects of mutual inductance are considered to eliminate the torque ripple caused by mutual coupling.

3.1 Review of Previous Work

Based on practical inductance profiles, Schramm *et al.* [16] proposed phase current optimal profiling in the sense of minimum stator copper loss. The commutation angle θ_c was selected where two adjacent phases would produce the same torque at the same current level assuming that commutation occurs instantaneously. The excitation interval of a phase was 15° in this control scheme. However due to the finite bandwidth of current control loop, it still showed significant torque ripple during commutation.

To avoid step-wise current or flux linkage commands, several schemes were also proposed such as in [17] - [21]. For instance, Husain *et al.* [17] and Ilic-Spong *et al.* [18] proposed a sinusoidal function and an exponential function as a TDF, respectively. The basic idea was to distribute the desired torque to two adjacent phases during predetermined commutation interval using the TDF. Consequently, the excitation interval of a phase was increased to more than 15 degrees. These schemes can be viewed as having TDFs given in (3.4)-(3.7) such that the sum of the phase torque commands are equal to the commanded torque.

$$T_e^* = T_x^* + T_y^* \tag{3.1}$$

where,

$$\begin{aligned} T_x^* &= T_e^* f_x(\theta) \\ T_y^* &= T_e^* f_y(\theta) \end{aligned} \tag{3.2}$$

The reference angles θ_i' and θ_f' are the initial and the final angle of the commutation region, respectively. According to the approaches, the choice of the reference angles depends on the inductance profile of a specific motor. For instance, when $T_e^* \geq 0$ and $0^\circ \leq \theta < 15^\circ$ for an 8/6 SRM,

$$0^\circ << \theta'_i < \theta'_f < 15^\circ \tag{3.3}$$

Therefore, the excitation interval of a phase was much narrower than 30 degrees and all phases were not fully utilized in their approaches. Husain *et al*. [17] proposed following TDF.

$$\begin{aligned} f_x(\theta) &= \begin{cases} 1 & \text{for } 0^\circ \le \theta < \theta'_i \\ (1 + cos\, k(\theta - \theta'_i))/2 & \text{for } \theta'_i \le \theta < \theta'_f \\ 0 & \text{for } \theta'_f \le \theta < 15^\circ \end{cases} \\ f_y(\theta) &= \begin{cases} 0 & \text{for } 0^\circ \le \theta < \theta'_i \\ (1 - cos\, k(\theta - \theta'_i))/2 & \text{for } \theta'_i \le \theta < \theta'_f \\ 1 & \text{for } \theta'_f \le \theta < 15^\circ \end{cases} \end{aligned} \tag{3.4}$$

where,

$$k = 180/(\theta'_f - \theta'_i) \tag{3.5}$$

On the other hand, Ilic-Spong *et al*. [18] proposed following TDF.

$$\begin{aligned} f_x(\theta) &= \begin{cases} 1 & \text{for } 0^\circ \le \theta < \theta'_i \\ e^{-(\theta - \theta'_i/k)^2} & \text{for } \theta'_i \le \theta < \theta'_f \\ 0 & \text{for } \theta'_f \le \theta < 15^\circ \end{cases} \\ f_y(\theta) &= \begin{cases} 1 & \text{for } 0^\circ \le \theta < \theta'_i \\ 1 - e^{-(\theta - \theta'_i/k)^2} & \text{for } \theta'_i \le \theta < \theta'_f \\ 0 & \text{for } \theta'_f \le \theta < 15^\circ \end{cases} \end{aligned} \tag{3.6}$$

where,

$$k = (\theta'_f - \theta'_i)/5 \tag{3.7}$$

The rates of change of phase current commands were reduced during commutation as expected but by assuming an ideal inductance the resulting incorrect current commands caused torque error and by choosing relatively short commutation interval the changing rates of currents could not be reduced significantly.

For a 6/4 SRM, instead of defining a TDF, Wallace *et al.* [19] linearly decreased the leading phase current and increased the following phase current during commutation interval. By neglecting the relationship between the output torque and the phase currents during commutation, the torque ripple was inevitable whereas the rates of change of phase currents were fixed for a given torque command. Kim *et al.* [20] proposed a torque distribution function, which could minimize the changing rates of currents over the commutation interval. With this approach an extensive off-line numerical calculation to obtain the optimal solution was necessary for individual SRM and excessive memory was required to store torque distribution functions. More importantly none of the approaches considered the effects of mutual inductance during commutation.

The effects of mutual inductance were mentioned in some papers such as [14] and [15]. However, those papers were focused mainly on the characteristics of the SRM and no control scheme to compensate the effects was proposed. The possibility of two-phase excitation was shown in reference [21]. Still the effects of mutual inductance were merely mentioned but not considered.

3.2 Proposed Torque Distribution Function Neglecting Mutual Inductance

TDF will be derived based on phase currents because the output torque equation in terms of phase currents is relatively simple. This TDF is readily applicable to the flux linkage based system due to the fact that no dynamics are involved in the relationship between phase currents and flux linkages.

If actual stator currents, i_x and i_y track current commands, i_x^* and i_y^* with desirable accuracy due to the high performance current controller, which will be described later in Chapter 4, the actual torque expressed by (2.18) can be indirectly controlled by controlling phase currents. In other words,

$$i_x^* \cong i_x, i_y^* \cong i_y \tag{3.8}$$

then,

$$T_e^* = \frac{1}{2} g_x \left(i_x^*\right)^2 + \frac{1}{2} g_y \left(i_y^*\right)^2 + g_{xy} i_x^* i_y^* \cong \frac{1}{2} g_x i_x^2 + \frac{1}{2} g_y i_y^2 + g_{xy} i_x i_y = T_e \tag{3.9}$$

Under the assumption of no tracking error, the following descriptions will be given without distinguishing command and feedback. If g_{xy} is equal to zero, then (3.9) is simplified as,

$$T_e = T_x + T_y \tag{3.10}$$

where,

$$\begin{aligned} T_x &= \frac{1}{2} g_x i_x^2 = f_x T_e \\ T_y &= \frac{1}{2} g_y i_y^2 = f_y T_e \end{aligned} \tag{3.11}$$

Now, torque functions f_x and f_y have to be determined for two-phase excitation. First, f_x and f_y are determined by neglecting mutual inductance and then they are modified to compensate for the effects of mutual coupling in the next section.

Possibly, there exist several criteria to choose torque functions. Commonly used criteria are as follows,

$$minimize\ J = \int_0^{60^\circ} \left(\sum_{k=a,b,c,d} \left(\frac{di_k}{d\theta} \right)^2 \right) d\theta \tag{3.12}$$

$$minimize\ J = \max_{0 \le \theta < 60^\circ} \left\{ \frac{di_k(\theta)}{d\theta} \right\} \text{ for } k = a,b,c,d \tag{3.13}$$

$$minimize\ J = \max_{0 \le \theta < 60^\circ} \left\{ i_k(\theta) \right\} \text{ for } k = a,b,c,d \tag{3.14}$$

$$minimize\ J = \sum_{k=a,b,c,d} \left(\int_0^{60^\circ} i_k^2 R_s d\theta \right) \tag{3.15}$$

Phase currents satisfying one of the performance indices specified by (3.12)-(3.15) can be determined by analytical or numerical methods as explained in [15] and [19]. But they are optimal only in one sense and each criterion may conflict. For instance, when the i^2R loss is minimized the other performance indices cannot be minimized as illustrated in Fig. 3.7. Hence, there should be a trade-off between them.

To ensure that the sum of T_x and T_y is equal to T_e, T_x and T_y have the same sign as T_e, and the waveforms of phase currents or flux linkages are smooth, TDF should satisfy the following constraints.

Constraints I:

$$\begin{aligned} &f_x(\theta) + f_y(\theta) = 1 \\ &0 \le f_x(\theta) \le 1 \quad f_x(\theta_i) = 1 \quad f_x(\theta_f) = 0 \qquad \text{for } \theta_i \le \theta \le \theta_f \\ &0 \le f_y(\theta) \le 1 \quad f_y(\theta_i) = 0 \quad f_y(\theta_f) = 1 \end{aligned} \tag{3.16}$$

where,

$$(\theta_i, \theta_f) \in \{(0^\circ, 15^\circ), (15^\circ, 30^\circ), (30^\circ, 45^\circ), (45^\circ, 60^\circ)\}$$

The reference angles θ_i and θ_f are the initial and the final angle of the commutation region, respectively.

Noting the fact that if more torque is distributed to the phase, whose self torque function is larger, the magnitude of phase currents can be reduced and the fact that $g_x g_y \ge 0$ for $\theta_i \le \theta \le \theta_f$ and $g_x(\theta_f) = 0, g_y(\theta_i) = 0$, the following TDF is proposed.

TDF I:

$$f_x = \frac{g_x^2}{g_x^2 + g_y^2}$$
$$f_y = \frac{g_y^2}{g_x^2 + g_y^2} \qquad \text{for } \theta_i \le \theta \le \theta_f \tag{3.17}$$

It is evident that TDF I satisfies constraints I given in (3.16). From (3.11) and (3.17), phase currents are calculated as,

$$i_x = \sqrt{\frac{2g_x T_e}{g_x^2 + g_y^2}}$$
$$i_y = \sqrt{\frac{2g_y T_e}{g_x^2 + g_y^2}} \qquad \text{for } \theta_i \le \theta \le \theta_f \tag{3.18}$$

When mutual inductance is neglected, phase flux linkages are calculated from (2.28) as,

$$\lambda_x = L_x i_x = L_x \sqrt{\frac{2g_x T_e}{g_x^2 + g_y^2}}$$
$$\lambda_y = L_y i_y = L_y \sqrt{\frac{2g_y T_e}{g_x^2 + g_y^2}} \qquad \text{for } \theta_i \le \theta \le \theta_f \tag{3.19}$$

TDF I in an excitation period is summarized in table I and shown in Fig. 3.1. The resultant phase currents, flux linkages and the torque error caused by TDF I at a given torque in the first quadrant operation are shown in Fig. 3.2 and 3.3, respectively. It should be mentioned that if f_k is equal to zero, to avoid unnecessary switching of devices, the corresponding phase is turned off instead of regulating i_k to zero. Operations in other quadrants are similar to the operation in the first quadrant. Although the rates of change of the phase currents and flux linkages are significantly reduced, there is about 7% peak-to-peak torque ripple caused by neglecting the mutual inductance.

TABLE 3.1 TDF I in an excitation period

	$T_e^* \geq 0$	$T_e^* < 0$
f_a	$\frac{g_a^2}{g_d^2+g_a^2}$ for $0^\circ \leq \theta < 15^\circ$ $\frac{g_a^2}{g_a^2+g_b^2}$ for $15^\circ \leq \theta < 30^\circ$ 0 for $30^\circ \leq \theta < 45^\circ$ 0 for $45^\circ \leq \theta < 60^\circ$	0 for $0^\circ \leq \theta < 15^\circ$ 0 for $15^\circ \leq \theta < 30^\circ$ $\frac{g_a^2}{g_d^2+g_a^2}$ for $30^\circ \leq \theta < 45^\circ$ $\frac{g_a^2}{g_a^2+g_b^2}$ for $45^\circ \leq \theta < 60^\circ$
f_b	0 for $0^\circ \leq \theta < 15^\circ$ $\frac{g_b^2}{g_a^2+g_b^2}$ for $15^\circ \leq \theta < 30^\circ$ $\frac{g_b^2}{g_b^2+g_c^2}$ for $30^\circ \leq \theta < 45^\circ$ 0 for $45^\circ \leq \theta < 60^\circ$	$\frac{g_b^2}{g_b^2+g_c^2}$ for $0^\circ \leq \theta < 15^\circ$ 0 for $15^\circ \leq \theta < 30^\circ$ 0 for $30^\circ \leq \theta < 45^\circ$ $\frac{g_b^2}{g_a^2+g_b^2}$ for $45^\circ \leq \theta < 60^\circ$
f_c	0 for $0^\circ \leq \theta < 15^\circ$ 0 for $15^\circ \leq \theta < 30^\circ$ $\frac{g_c^2}{g_b^2+g_c^2}$ for $30^\circ \leq \theta < 45^\circ$ $\frac{g_c^2}{g_c^2+g_d^2}$ for $45^\circ \leq \theta < 60^\circ$	$\frac{g_c^2}{g_b^2+g_c^2}$ for $0^\circ \leq \theta < 15^\circ$ $\frac{g_c^2}{g_c^2+g_d^2}$ for $15^\circ \leq \theta < 30^\circ$ 0 for $30^\circ \leq \theta < 45^\circ$ 0 for $45^\circ \leq \theta < 60^\circ$
f_d	$\frac{g_d^2}{g_d^2+g_a^2}$ for $0^\circ \leq \theta < 15^\circ$ 0 for $15^\circ \leq \theta < 30^\circ$ 0 for $30^\circ \leq \theta < 45^\circ$ $\frac{g_d^2}{g_c^2+g_d^2}$ for $45^\circ \leq \theta < 60^\circ$	0 for $0^\circ \leq \theta < 15^\circ$ $\frac{g_d^2}{g_c^2+g_d^2}$ for $15^\circ \leq \theta < 30^\circ$ $\frac{g_d^2}{g_d^2+g_a^2}$ for $30^\circ \leq \theta < 45^\circ$ 0 for $45^\circ \leq \theta < 60^\circ$

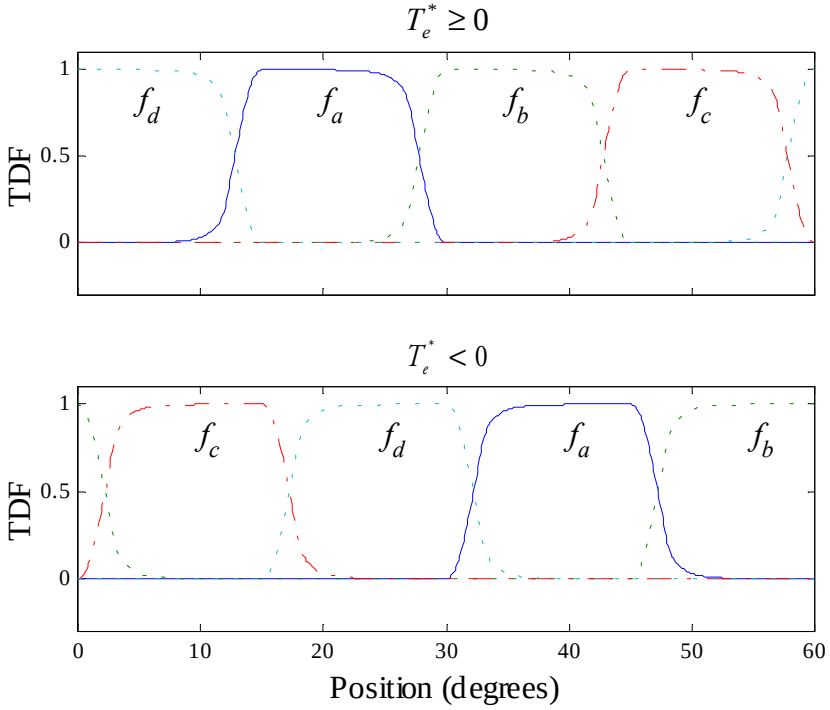

Fig. 3.1 TDF I in an excitation period

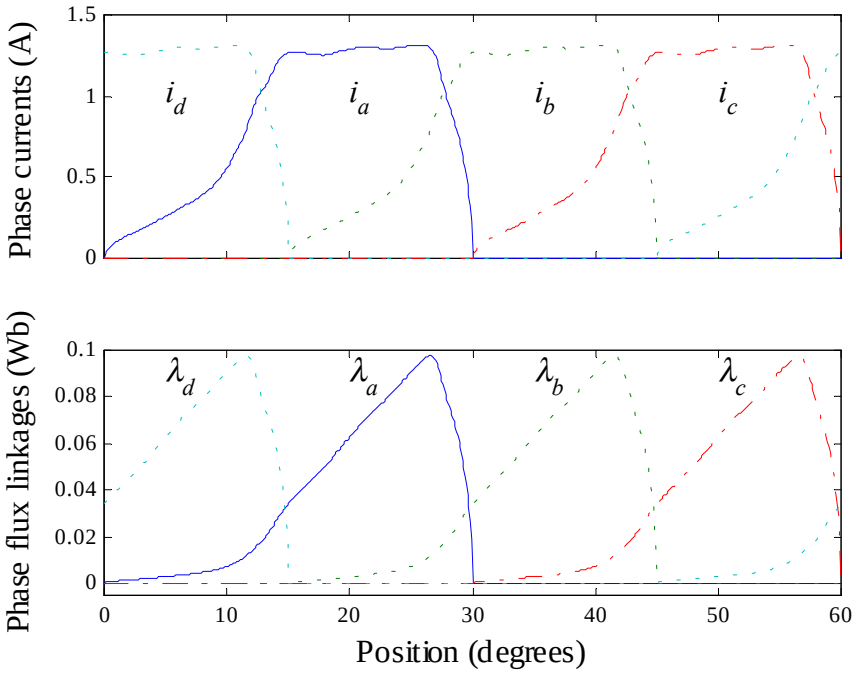

Fig. 3.2 Resultant phase currents and flux linkages for TDF I at T_e^*=0.2 N·m

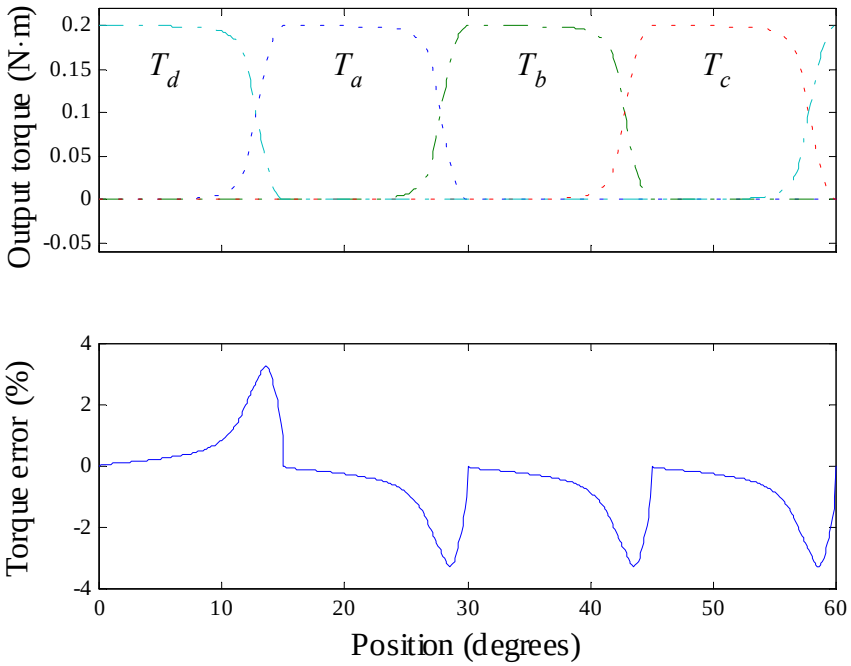

Fig. 3.3 Resultant output torque and torque error for TDF I at T_e^*=0.2 N·m

3.3 Proposed Torque Distribution Function Considering Mutual Inductance

In some applications, the torque ripple caused by the mutual inductance may not be acceptable. The prototype SRM was designed to minimize mutual inductance but generally mutual inductance is relatively larger due to higher β_s and β_r. In [14] and [15], β_s and β_r are reported to be $20.2^\circ, 23.5^\circ$, and $23^\circ, 24^\circ$, respectively, and the mutual inductances of their designs are larger than the prototype SRM's. Therefore, it is evident that TDF I given in (3.17) can cause higher torque ripple in those cases. As a result, the TDF has to be modified to eliminate the torque error.

When mutual inductance is not neglected, the three torque components in (2.18) are defined as,

$$T_e = T_x + T_y + T_{xy} \tag{3.20}$$

where,

$$T_x = \frac{1}{2} g_x i_x^2 = f_x T_e$$
$$T_y = \frac{1}{2} g_y i_y^2 = f_y T_e \tag{3.21}$$

$$T_{xy} = g_{xy} i_x i_y = f_{xy} T_e \tag{3.22}$$

The constraints for new TDF are modified as follows.

Constraints II:

$$\begin{aligned} & f_x(\theta) + f_y(\theta) + f_{xy}(\theta) = 1 \\ & 0 \le f_x(\theta) \le 1 \quad f_x(\theta_i) = 1 \quad f_x(\theta_f) = 0 \qquad \text{for } \theta_i \le \theta \le \theta_f \\ & 0 \le f_y(\theta) \le 1 \quad f_y(\theta_i) = 0 \quad f_y(\theta_f) = 1 \end{aligned} \tag{3.23}$$

where,

$$(\theta_i, \theta_f) \in \{(0^\circ, 15^\circ), (15^\circ, 30^\circ), (30^\circ, 45^\circ), (45^\circ, 60^\circ)\}$$

The reference angles θ_i and θ_f are the initial and the final angle of the commutation region, respectively. If f_x and f_y are slightly modified, similar relationship can be found. Because of the quadratic form of TDF I, f_x, f_y and f_{xy} can be of the following form to satisfy the constraints II given in (3.23).

$$f_x = \frac{g_x^2}{g_x^2 + g_y^2 \pm h_{xy}}$$
$$f_y = \frac{g_y^2}{g_x^2 + g_y^2 \pm h_{xy}} \tag{3.24}$$

$$f_{xy} = \frac{h_{xy}^2}{g_x^2 + g_y^2 \pm h_{xy}} \tag{3.25}$$

where h_{xy} is unknown variable to be solved. Note that in the denominator a plus sign applies when the output torque is positive and a minus sign applies when the output torque is negative. From (3.21) and (3.24), the phase currents are expressed as,

$$\begin{aligned} i_x &= \sqrt{\frac{2T_x}{g_x}} = \sqrt{\frac{2T_e g_x}{g_x^2 + g_y^2 \pm h_{xy}}} \\ i_y &= \sqrt{\frac{2T_y}{g_y}} = \sqrt{\frac{2T_e g_y}{g_x^2 + g_y^2 \pm h_{xy}}} \end{aligned} \tag{3.26}$$

Substituting (3.26) into (3.22) yields,

$$T_{xy} = \frac{2g_{xy}\sqrt{g_x g_y}}{g_x^2 + g_y^2 \pm h_{xy}} T_e \tag{3.27}$$

From (3.22), (3.25), and (3.27),

$$h_{xy} = 2g_{xy}\sqrt{g_x g_y} \tag{3.28}$$

Substituting (3.28) into (3.24) and (3.25) yields,

TDF II:

$$\begin{aligned} f_x &= \frac{g_x^2}{g_x^2 + g_y^2 \pm 2g_{xy}\sqrt{g_x g_y}} \\ f_y &= \frac{g_y^2}{g_x^2 + g_y^2 \pm 2g_{xy}\sqrt{g_x g_y}} \qquad \text{for } \theta_i \le \theta \le \theta_f \\ f_{xy} &= \frac{2g_{xy}\sqrt{g_x g_y}}{g_x^2 + g_y^2 \pm 2g_{xy}\sqrt{g_x g_y}} \end{aligned} \tag{3.29}$$

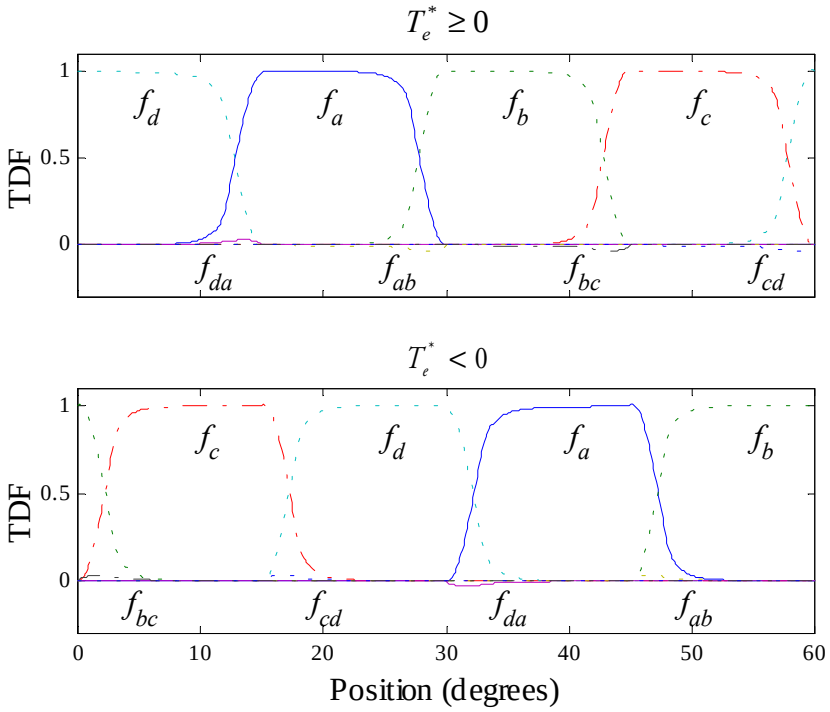

Fig. 3.4 TDF II in an excitation period

TDF II satisfies constraints II given in (3.23). Therefore, phase currents are calculated as,

$$i_x = \sqrt{\frac{2g_x T_e}{g_x^2 + g_y^2 \pm 2g_{xy}\sqrt{g_x g_y}}}$$
$$i_y = \sqrt{\frac{2g_y T_e}{g_x^2 + g_y^2 \pm 2g_{xy}\sqrt{g_x g_y}}} \qquad \text{for } \theta_i \leq \theta \leq \theta_f \qquad (3.30)$$

And phase flux linkages are calculated as,

$$\lambda_x = L_x\sqrt{\frac{2g_x T_e}{g_x^2 + g_y^2 \pm 2g_{xy}\sqrt{g_x g_y}}} + M_{xy}\sqrt{\frac{2g_y T_e}{g_x^2 + g_y^2 \pm 2g_{xy}\sqrt{g_x g_y}}}$$
$$\lambda_y = M_{xy}\sqrt{\frac{2g_x T_e}{g_x^2 + g_y^2 \pm 2g_{xy}\sqrt{g_x g_y}}} + L_y\sqrt{\frac{2g_y T_e}{g_x^2 + g_y^2 \pm 2g_{xy}\sqrt{g_x g_y}}} \qquad \text{for } \theta_i \leq \theta \leq \theta_f \quad (3.31)$$

TABLE 3.2 TDF II in an excitation period

	$T_e^* \geq 0$		$T_e^* < 0$	
f_a	$\frac{g_a^2}{g_d^2 + g_a^2 + 2g_{da}\sqrt{g_d g_a}}$	for $0^\circ \leq \theta < 15^\circ$	0	for $0^\circ \leq \theta < 15^\circ$
	$\frac{g_a^2}{g_a^2 + g_b^2 + 2g_{ab}\sqrt{g_a g_b}}$	for $15^\circ \leq \theta < 30^\circ$	0	for $15^\circ \leq \theta < 30^\circ$
	0	for $30^\circ \leq \theta < 45^\circ$	$\frac{g_a^2}{g_d^2 + g_a^2 - 2g_{da}\sqrt{g_d g_a}}$	for $30^\circ \leq \theta < 45^\circ$
	0	for $45^\circ \leq \theta < 60^\circ$	$\frac{g_a^2}{g_a^2 + g_b^2 - 2g_{ab}\sqrt{g_a g_b}}$	for $45^\circ \leq \theta < 60^\circ$
f_b	0	for $0^\circ \leq \theta < 15^\circ$	$\frac{g_b^2}{g_b^2 + g_c^2 - 2g_{bc}\sqrt{g_b g_c}}$	for $0^\circ \leq \theta < 15^\circ$
	$\frac{g_b^2}{g_a^2 + g_b^2 + 2g_{ab}\sqrt{g_a g_b}}$	for $15^\circ \leq \theta < 30^\circ$	0	for $15^\circ \leq \theta < 30^\circ$
	$\frac{g_b^2}{g_b^2 + g_c^2 + 2g_{bc}\sqrt{g_b g_c}}$	for $30^\circ \leq \theta < 45^\circ$	0	for $30^\circ \leq \theta < 45^\circ$
	0	for $45^\circ \leq \theta < 60^\circ$	$\frac{g_b^2}{g_a^2 + g_b^2 - 2g_{ab}\sqrt{g_a g_b}}$	for $45^\circ \leq \theta < 60^\circ$
f_c	0	for $0^\circ \leq \theta < 15^\circ$	$\frac{g_c^2}{g_b^2 + g_c^2 - 2g_{bc}\sqrt{g_b g_c}}$	for $0^\circ \leq \theta < 15^\circ$
	0	for $15^\circ \leq \theta < 30^\circ$	$\frac{g_c^2}{g_c^2 + g_d^2 - 2g_{cd}\sqrt{g_c g_d}}$	for $15^\circ \leq \theta < 30^\circ$
	$\frac{g_c^2}{g_b^2 + g_c^2 + 2g_{bc}\sqrt{g_b g_c}}$	for $30^\circ \leq \theta < 45^\circ$	0	for $30^\circ \leq \theta < 45^\circ$
	$\frac{g_c^2}{g_c^2 + g_d^2 + 2g_{cd}\sqrt{g_c g_d}}$	for $45^\circ \leq \theta < 60^\circ$	0	for $45^\circ \leq \theta < 60^\circ$
f_d	$\frac{g_d^2}{g_d^2 + g_a^2 + 2g_{da}\sqrt{g_d g_a}}$	for $0^\circ \leq \theta < 15^\circ$	0	for $0^\circ \leq \theta < 15^\circ$
	0	for $15^\circ \leq \theta < 30^\circ$	$\frac{g_d^2}{g_c^2 + g_d^2 - 2g_{cd}\sqrt{g_c g_d}}$	for $15^\circ \leq \theta < 30^\circ$
	0	for $30^\circ \leq \theta < 45^\circ$	$\frac{g_d^2}{g_d^2 + g_a^2 - 2g_{da}\sqrt{g_d g_a}}$	for $30^\circ \leq \theta < 45^\circ$
	$\frac{g_d^2}{g_c^2 + g_d^2 + 2g_{cd}\sqrt{g_c g_d}}$	for $45^\circ \leq \theta < 60^\circ$	0	for $45^\circ \leq \theta < 60^\circ$

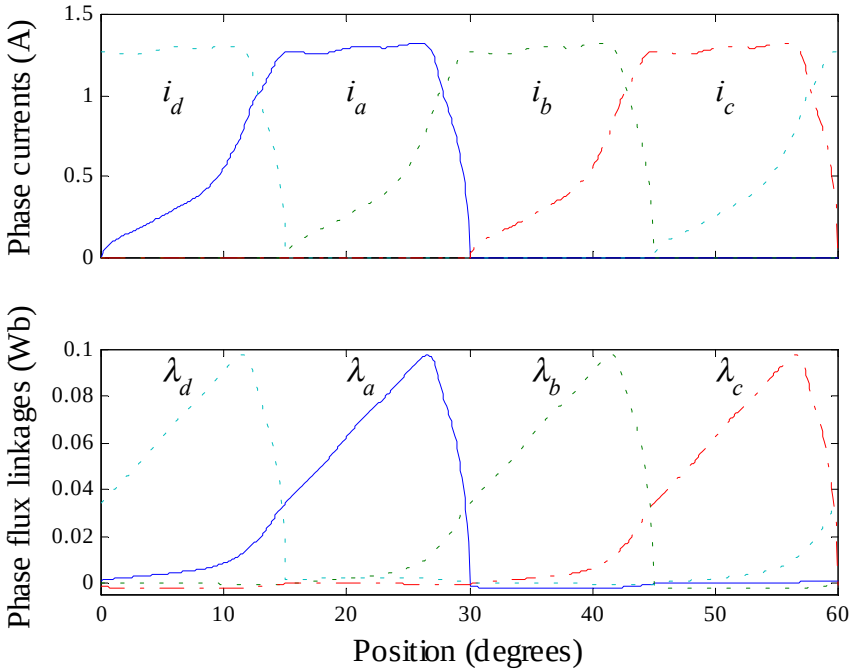

Fig. 3.5 Resultant phase currents and flux linkages for TDF II at T_e^*=0.2 N·m

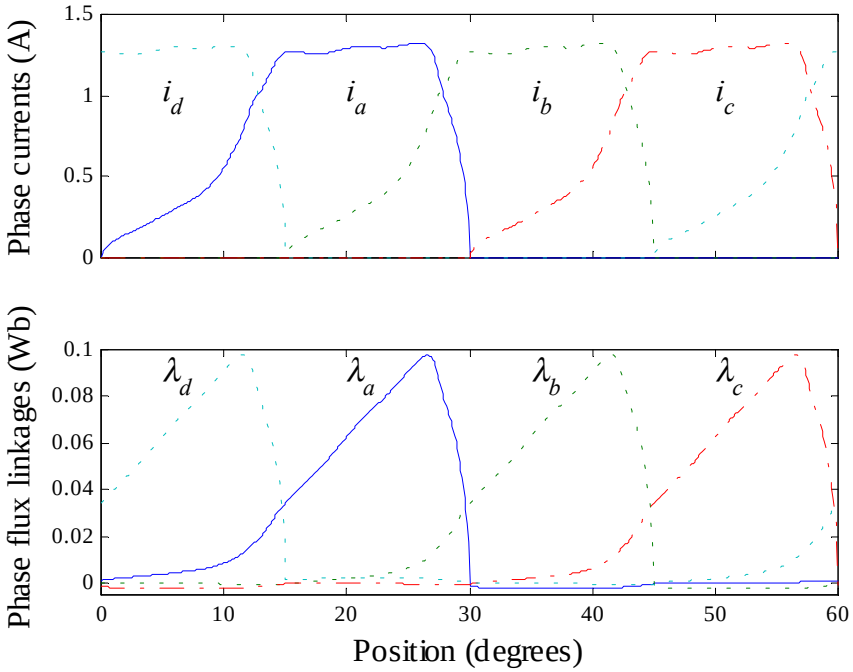

Fig. 3.6 Resultant output torque and torque error for TDF II at T_e^*=0.2 N·m

TDF II in an excitation period is summarized in table II. Fig. 3.4 shows TDF II in an excitation period. The resultant phase currents and flux linkages at a given torque are shown in Fig. 3.5. Fig. 3.6 shows the output torque and the torque error for TDF II. The phase currents and flux linkages in Fig. 3.2 and Fig. 3.5 are almost equal because the magnitude of mutual inductance is relatively small when compared with the magnitude of self-inductance.

3.4 Comparison of Torque Distribution Functions

The torque control scheme proposed by Schramm *et al.* [15] is chosen for comparison with the proposed TDF and named as TDF III for notational convenience. TDF III can be considered as the representation of conventional drives strategy because only one phase is excited at a time in this control scheme and phase current is calculated from the instantaneous self torque function instead of the average value of the torque function described in Section 1.1. In Table 3.4, TDF III in an excitation period is listed. In Fig. 3.7, the phase currents to satisfy the performance index (3.15), that minimizes stator copper loss, are shown for comparison.

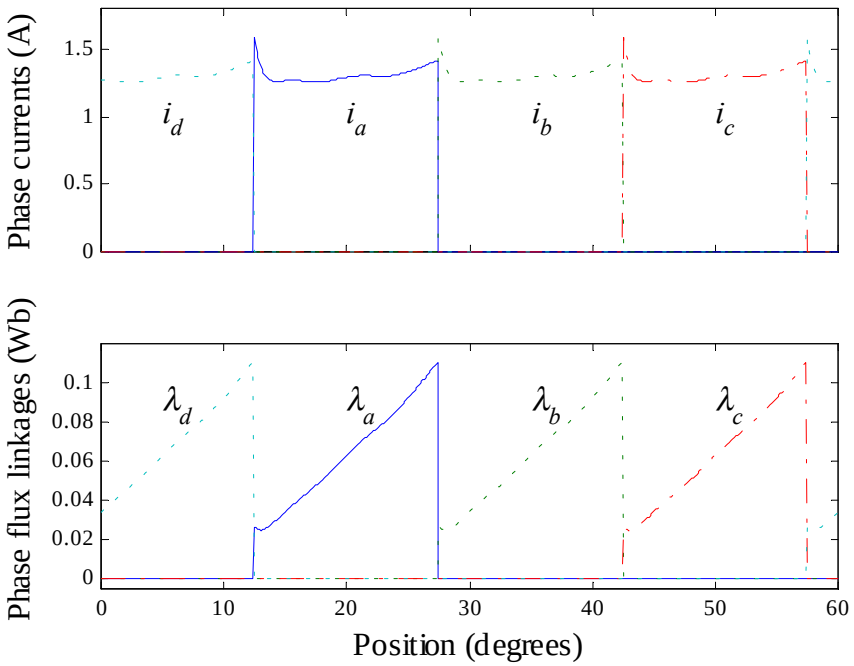

Fig. 3.7 Resultant phase currents and flux linkages for TDF III at T_e^*=0.2 N·m

TABLE 3.3 TDF III in an excitation period

	$T_e^* \geq 0$	$T_e^* < 0$
f_a	0 for $0^\circ \leq \theta < 12.4^\circ$ 1 for $12.4^\circ \leq \theta < 27.4^\circ$ 0 for $27.4^\circ \leq \theta < 42.4^\circ$ 0 for $42.4^\circ \leq \theta < 57.4^\circ$ 0 for $57.4^\circ \leq \theta < 60^\circ$	0 for $0^\circ \leq \theta < 2.6^\circ$ 0 for $2.6^\circ \leq \theta < 17.6^\circ$ 0 for $17.6^\circ \leq \theta < 32.6^\circ$ 1 for $32.6^\circ \leq \theta < 47.6^\circ$ 0 for $47.6^\circ \leq \theta < 60^\circ$
f_b	0 for $0^\circ \leq \theta < 12.4^\circ$ 0 for $12.4^\circ \leq \theta < 27.4^\circ$ 1 for $27.4^\circ \leq \theta < 42.4^\circ$ 0 for $42.4^\circ \leq \theta < 57.4^\circ$ 0 for $57.4^\circ \leq \theta < 60^\circ$	1 for $0^\circ \leq \theta < 2.6^\circ$ 0 for $2.6^\circ \leq \theta < 17.6^\circ$ 0 for $17.6^\circ \leq \theta < 32.6^\circ$ 0 for $32.6^\circ \leq \theta < 47.6^\circ$ 1 for $47.6^\circ \leq \theta < 60^\circ$
f_c	0 for $0^\circ \leq \theta < 12.4^\circ$ 0 for $12.4^\circ \leq \theta < 27.4^\circ$ 0 for $27.4^\circ \leq \theta < 42.4^\circ$ 1 for $42.4^\circ \leq \theta < 57.4^\circ$ 0 for $57.4^\circ \leq \theta < 60^\circ$	0 for $0^\circ \leq \theta < 2.6^\circ$ 1 for $2.6^\circ \leq \theta < 17.6^\circ$ 0 for $17.6^\circ \leq \theta < 32.6^\circ$ 0 for $32.6^\circ \leq \theta < 47.6^\circ$ 0 for $47.6^\circ \leq \theta < 60^\circ$
f_d	1 for $0^\circ \leq \theta < 12.4^\circ$ 0 for $12.4^\circ \leq \theta < 27.4^\circ$ 0 for $27.4^\circ \leq \theta < 42.4^\circ$ 0 for $42.4^\circ \leq \theta < 57.4^\circ$ 1 for $57.4^\circ \leq \theta < 60^\circ$	0 for $0^\circ \leq \theta < 2.6^\circ$ 0 for $2.6^\circ \leq \theta < 17.6^\circ$ 1 for $17.6^\circ \leq \theta < 32.6^\circ$ 0 for $32.6^\circ \leq \theta < 47.6^\circ$ 0 for $47.6^\circ \leq \theta < 60^\circ$

The resultant phase currents and torque error are calculated assuming there is no limit on the maximum value of phase currents. In addition, no tracking error is assumed. However, the phase current commands are not easily followed due to the sudden changes demanded. Hence, there will be a torque error caused by the tracking error and the effects of mutual coupling. Moreover, because of converter ratings, the phase currents are limited to a certain maximum value. The ratings of converter should be increased to eliminate the torque ripple caused by the maximum limit and this is likely to increase the cost of converter. If the rms and peak current value are defined as,

$$I_{rms} = max\left(\sqrt{\frac{1}{T}\int_0^{60^\circ} i_a^2 d\theta}\right) \text{ for } k = a,b,c,d \tag{3.32}$$

$$I_{peak} = \max_{0\le\theta<60^\circ}\{i_k(\theta)\} \text{ for } k = a,b,c,d \tag{3.33}$$

Then compared with the minimum stator copper loss scheme, the proposed TDF II shows about 19.7% decrease in peak current and 4.3% increase in rms current value. Smaller peak current is important in the sense that deeper saturation causes more loss and the converter is not fully utilized due to the limit of peak current. In addition, due to the reduced rates of change of phase currents in TDF II, the current commands are easily followed with practical and moderate controller gains.

TABLE 3.4 Comparison of TDF I, II, and III

	TDF I	TDF II	TDF III
I_{rms} (A)	0.679	0.680	0.651
I_{peak} (A)	1.31	1.32	1.58

CHAPTER 4: TORQUE CONTROL

The dynamics of the SRM are nonlinear and coupled as is evident from the system equations described in Chapter 2. This inherently affects designing an accurate control system. Designing a control system for a linear and decoupled system is a much easier task and hence the nonlinear system will be linearized and decoupled through a feedback linearization so as to apply well-known linear control techniques.

To control the output torque, either phase currents or flux linkages can be chosen as state variables as discussed in Chapter 3. Each has its own advantages and the maximization of its advantages depends on how the state feedback and states are obtained. Torque control based on phase currents is considered in section 4.1 with simulation and experimental results. Torque control based on phase flux linkages is described in section 4.2 with simulation results. To avoid tedious derivations and to deal with the more general case, the dynamics neglecting mutual inductance are not discussed in this chapter.

4.1 Torque Control Based on Phase Currents

4.1.1 Feedback Linearization and Decoupling Controller

The dynamics of the current loop are nonlinear and time varying due to the dependence of inductance on position and the mutual inductance between two adjacent phases. Nevertheless, phase current needs to be controlled precisely to achieve required performance. A feedback linearizing current controller is applied to linearize and decouple the current control loop and then a gain-scheduling scheme is introduced to maintain the performance of the current control loop at any rotor position.

Feedback linearization is a powerful tool for analyzing a nonlinear system or designing a controller for the system. The central idea of this approach is to algebraically transform a

nonlinear system into a linear one, so that the well known linear control techniques can be applied. When a system is linearized, it is desirable to make the system decoupled so that an input can control an output or a state. In this research, the decoupling as well as feedback linearization are achieved by a simple procedure. This is fundamentally different from conventional linearization in the sense that the feedback linearization is achieved by exact state transformation, input transformation and state feedback, rather than by linear approximation of the system around an operating point or multiple points.

Mathematical tools such as differential geometry and topology have been used to find a state transformation and an input transformation. Intuition of a designer also plays an important role in finding such transformations because the new states and inputs must be available and physically meaningful. Two steps are needed in this approach. Firstly, there is a need to find a state transformation if necessary and an input transformation so that the nonlinear system is transformed into an equivalent linear system. Secondly, usual linear control techniques are used to design the new input [27].

The dynamic equations of the SRM in terms of phase currents are rewritten for convenience as,

$$\begin{aligned}
\frac{di_x}{dt} &= -a_1 i_x - a_2 \omega i_x + a_3 i_y + a_4 \omega i_y + a_0 \left(v_x - \frac{M_{xy}}{L_y} v_y \right) \\
\frac{di_y}{dt} &= -b_1 i_y - b_2 \omega i_y + b_3 i_x + b_4 \omega i_x + b_0 \left(-\frac{M_{xy}}{L_x} v_x + v_y \right)
\end{aligned} \tag{4.1}$$

$$\frac{d\omega}{dt} = -\frac{1}{J}\omega + \frac{B}{J}\left(\frac{1}{2} g_x i_x^2 + \frac{1}{2} g_y i_y^2 + g_{xy} i_x i_y \right) \tag{4.2}$$

The current loop in block diagram form is shown in Fig. 4.1. The nonlinear terms such as the second and the fourth terms in the right hand side of (4.1) and the coupling term such as the third term are viewed as disturbances to make the block diagram look simple. In (4.1), it can be seen that there are two inputs v_x and v_y, and two states i_x and i_y. The dynamics and the input of one phase affect those of the other phase so that both states and inputs need to be decoupled. The

state decoupling can be achieved by state feedback and the input decoupling can be achieved by an input transformation.

First, the input $\boldsymbol{v} = \begin{bmatrix} v_x & v_y \end{bmatrix}^T$ is transformed. A transformation matrix $\boldsymbol{E}$ and a control law $\boldsymbol{u} = \begin{bmatrix} u_x & u_y \end{bmatrix}^T$ are defined as,

$$\begin{bmatrix} u_x \\ u_y \end{bmatrix} = \boldsymbol{E} \begin{bmatrix} v_x \\ v_y \end{bmatrix} \tag{4.3}$$

where,

$$\boldsymbol{E} = \begin{bmatrix} 1 & -M_{xy}/L_y \\ -M_{xy}/L_x & 1 \end{bmatrix} \tag{4.4}$$

Now, the control law $\boldsymbol{u} = \begin{bmatrix} u_x & u_y \end{bmatrix}^T$ of the form can cancel the nonlinearities and are given as,

$$\begin{bmatrix} u_x \\ u_y \end{bmatrix} = \begin{bmatrix} \left(a_2 \omega i_x - a_3 i_y - a_4 \omega i_y\right)/a_0 \\ \left(b_2 \omega i_y - b_3 i_x - b_4 \omega i_x\right)/b_0 \end{bmatrix} + \begin{bmatrix} \bar{u}_x \\ \bar{u}_y \end{bmatrix} \tag{4.5}$$

Where $\bar{\boldsymbol{u}} = \begin{bmatrix} \bar{u}_x & \bar{u}_y \end{bmatrix}^T$ is an equivalent input to be designed. The input transformation matrix $\boldsymbol{E}$ and the control law $\boldsymbol{u}$ transform the system (4.11) to a linear system as,

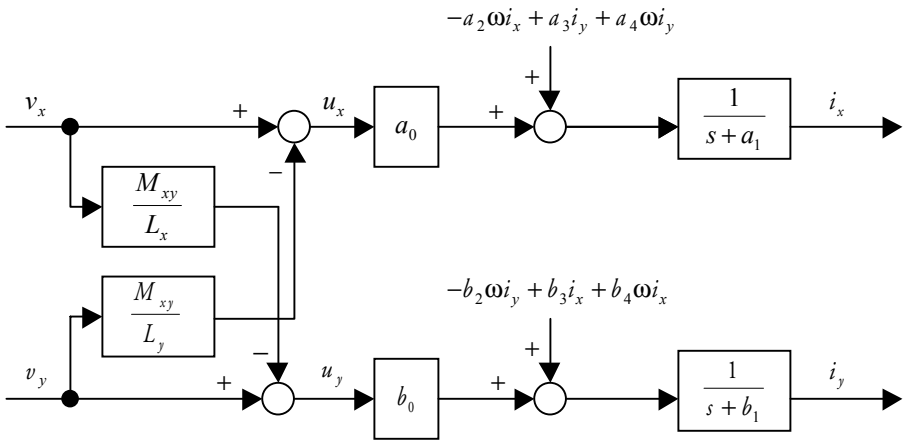

Fig. 4.1 Current loop

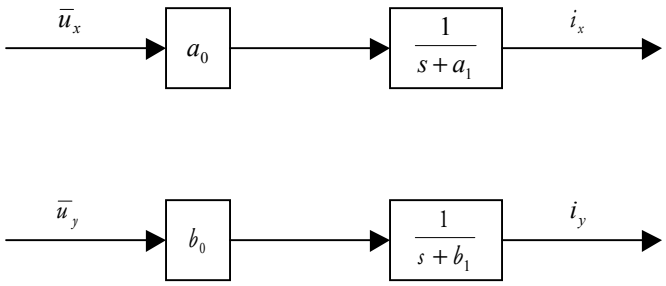

Fig. 4.2 Linearized and decoupled current loop

$$\begin{aligned} \frac{di_x}{dt} &= -a_1 i_x + a_0 \bar{u}_x \\ \frac{di_y}{dt} &= -b_1 i_y + b_0 \bar{u}_y \end{aligned} \tag{4.6}$$

Since the system (4.6) is linear and decoupled, a state transformation is not necessary in this case. The linearized and decoupled current loop is shown in Fig. 4.2. Since the inputs $\bar{u}_x$ and $\bar{u}_y$ only affect the outputs i_x and i_y, respectively, they are decoupling control laws. In addition, the invertible matrix $\boldsymbol{E}$ is the decoupling matrix of the system. That is, the physical input $\boldsymbol{v} = \begin{bmatrix} v_x & v_y \end{bmatrix}^T$ is calculated as,

$$\begin{bmatrix} v_x \\ v_y \end{bmatrix} = \boldsymbol{E}^{-1} \cdot \begin{bmatrix} u_x \\ u_y \end{bmatrix} = \frac{1}{D} \begin{bmatrix} L_x L_y & L_x M_{xy} \\ L_y M_{xy} & L_x L_y \end{bmatrix} \cdot \begin{bmatrix} u_x \\ u_y \end{bmatrix} \tag{4.7}$$

4.1.2 Gain Scheduling

It should be mentioned that system (4.6) is a linear time varying system. The coefficients of the dynamic equations are functions of rotor position and hence they are functions of time. But by examining the characteristics of self and mutual inductance, it is known that they are slowly varying compared with the bandwidth of the current control loop. Therefore, by adapting gains of the current controller, the performance of the current control loop can be maintained

regardless of rotor position. To obtain desired transient and steady state performances, the new control inputs $\bar{u}_x$ and $\bar{u}_y$ are given by proportional and integral (PI) controller as,

$$\begin{aligned}\bar{u}_x &= K_{px}\left[\left(i_x^* - i_x\right) + K_{ix}\int_0^t \left(i_x^* - i_x\right)d\tau\right] \\ \bar{u}_y &= K_{py}\left[\left(i_y^* - i_y\right) + K_{iy}\int_0^t \left(i_y^* - i_y\right)d\tau\right]\end{aligned} \tag{4.8}$$

Where K_{px}, K_{py}, K_{ix}, and K_{iy} are the gains of PI controllers for *x* and *y* phases, respectively. They can be evaluated by the conventional design procedure based on the frequency response characteristics. The system transfer functions $G_{cx}(s)$ and $G_{cy}(s)$ are derived from Fig. 4.3 as,

$$\begin{aligned}G_{cx}(s) \equiv \frac{i_x(s)}{i_x^*(s)} &= \frac{1}{H_c}\cdot\frac{a_0 H_c K_r K_{px} s + a_0 H_c K_r K_{px} K_{ix}}{s^2 + \left(a_0 H_c K_r K_{px} + a_1\right)s + a_0 H_c K_r K_{px} K_{ix}} \\ &\cong \frac{1}{H_c}\cdot\frac{K_{1x}K_{px}s + K_{1x}K_{px}K_{ix}}{s^2 + K_{1x}K_{px}s + K_{1x}K_{px}K_{ix}} \quad \text{for } a_0 H_c K_r K_{px} >> a_1 \\ G_{cy}(s) \equiv \frac{i_y(s)}{i_y^*(s)} &= \frac{1}{H_c}\cdot\frac{b_0 H_c K_r K_{py} s + b_0 H_c K_r K_{py} K_{iy}}{s^2 + \left(b_0 H_c K_r K_{py} + b_1\right)s + b_0 H_c K_r K_{py} K_{iy}} \\ &\cong \frac{1}{H_c}\cdot\frac{K_{1y}K_{py}s + K_{1y}K_{py}K_{iy}}{s^2 + K_{1y}K_{py}s + K_{1y}K_{py}K_{iy}} \quad \text{for } b_0 H_c K_r K_{py} >> b_1\end{aligned} \tag{4.9}$$

where,

$$\begin{aligned}&K_{1x} = a_0 H_c K_r \\ &K_{1y} = b_0 H_c K_r \\ &H_c : \text{current feedback gain} \\ &K_r : \text{converter gain}\end{aligned} \tag{4.10}$$

Now, to determine the gains K_{px}, K_{py}, K_{ix}, and K_{iy} to meet the control objectives a simple and straightforward design procedure is proposed. Two of the most common control objectives are the bandwidth and the damping ratio of the current control loop. For a given bandwidth ω_c and damping ratio ζ_c, the controller gains are algebraically calculated as,

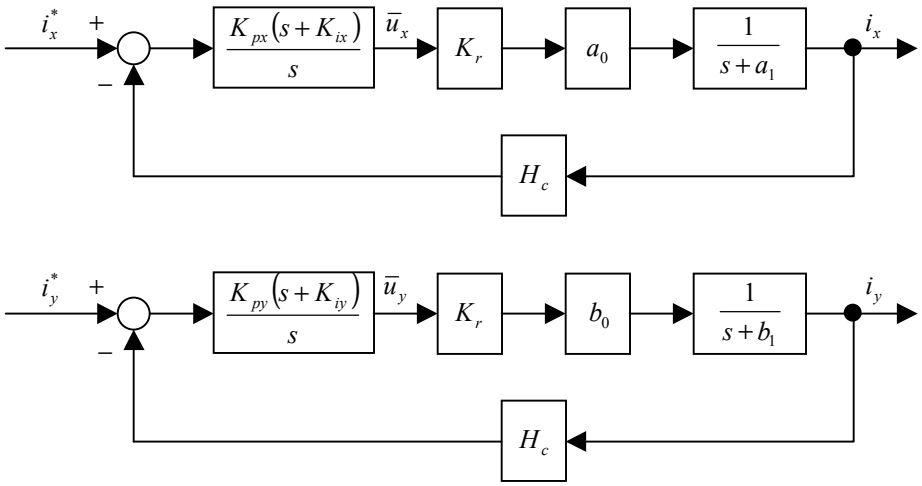

Fig. 4.3 Current control loop with PI controller

$$K_{px}(\theta)=\frac{2\zeta_c\omega_c}{\sqrt{\left(1+2\zeta_c^2\right)+\sqrt{\left(1+2\zeta_c^2\right)^2+1}}}\cdot\frac{1}{K_{1x}(\theta)}$$
$$K_{ix}=\frac{\omega_c}{2\zeta_c\sqrt{\left(1+2\zeta_c^2\right)+\sqrt{\left(1+2\zeta_c^2\right)^2+1}}} \tag{4.11}$$

$$K_{py}(\theta)=\frac{2\zeta_c\omega_c}{\sqrt{\left(1+2\zeta_c^2\right)+\sqrt{\left(1+2\zeta_c^2\right)^2+1}}}\cdot\frac{1}{K_{1y}(\theta)}$$
$$K_{iy}=\frac{\omega_c}{2\zeta_c\sqrt{\left(1+2\zeta_c^2\right)+\sqrt{\left(1+2\zeta_c^2\right)^2+1}}} \tag{4.12}$$

Details of the gain derivations are given in Appendix B. The proportional gains $K_{px}(\theta)$ and $K_{py}(\theta)$ are inversely proportional to $K_{1x}(\theta)$ and $K_{1y}(\theta)$ given in (4.10), respectively. The integral gains K_{ix} and K_{iy} are constant regardless of rotor position. Hence, by only adapting the proportional gains $K_{px}(\theta)$ and $K_{py}(\theta)$ according to rotor position, the characteristics of the current control loop will be identical at all rotor positions. Considering the high gains of the current control loop, the coefficients $a_1(\theta)$ and $b_1(\theta)$ can be regarded as slowly varying variables or constants.

To examine the responses of the conventional PI and proposed current controller, simulation and experimental results are shown in Fig. 4.4(a) and (b), respectively. The simulation results and experimental results are obtained at $T_e^* = 0.2\,\mathrm{N}\cdot\mathrm{m}$ and $\omega = 1000\,\mathrm{rpm}$. The phase current commands, which are indicated by dashed lines in Fig. 4.4(a), are obtained using the TDF II described in Section 3.3 and summarized in Table 3.2. The upper traces of Fig. 4.4(b) are the phase currents obtained by the conventional PI controller and the lower traces are the phase currents obtained by the proposed current controller, respectively. A unipolar switching strategy to be described in Chapter 6 of this dissertation is used as a switching strategy for the simulations and experiments. For the simulations, the phase currents are sampled at every 50 μs, and the control loop and PWM signals are also updated at 50 μs to have 2 kHz of the current control loop bandwidth and 20 kHz of switching frequency. Mutual inductances are neglected in the conventional PI controller. On the other hand, the gains of the proposed current controller are adapted from the relationships described in (4.11) and (4.12) to maintain the desired bandwidth and damping ratio. However, because of the limited capacity of the experimental setup described in Chapter 7, the sampling time for the experiments is set to 100 μs to have 1 kHz of the current control loop bandwidth and 10 kHz of switching frequency.

When compared with the simulation results in Fig. 4.4(a), the experimental results in Fig. 4.4(b) show more current ripple and slower response due to the embedded switching noise and larger sampling time but they strongly match the simulation results. As shown in Fig. 4.4, the conventional controller is not suitable for high performance SRM drives because of the following reasons. First, the dynamic characteristics of two different phase current control loops are not identical due to the varying inductances. Second, the responses at positions, where self inductance is much larger than L_{min}, are not desirable because of lower bandwidth and smaller damping ratio. Therefore, the responses at those points are sluggish and large overshoots can be observed. There also exists coupling between phases.

This leads to the proposed decoupling controller with a gain scheduling. As shown in simulation and experimental results, the proposed current controller shows good tracking performance at all positions.

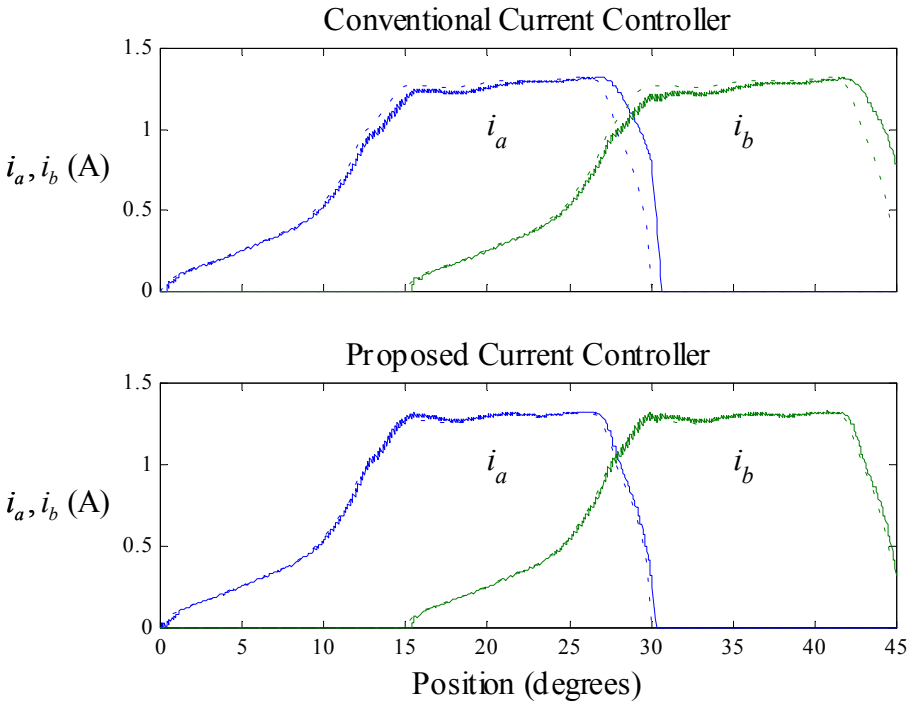

(a) Simulation results

(Vertical div.=0.5 A, horizontal div.=1 ms)

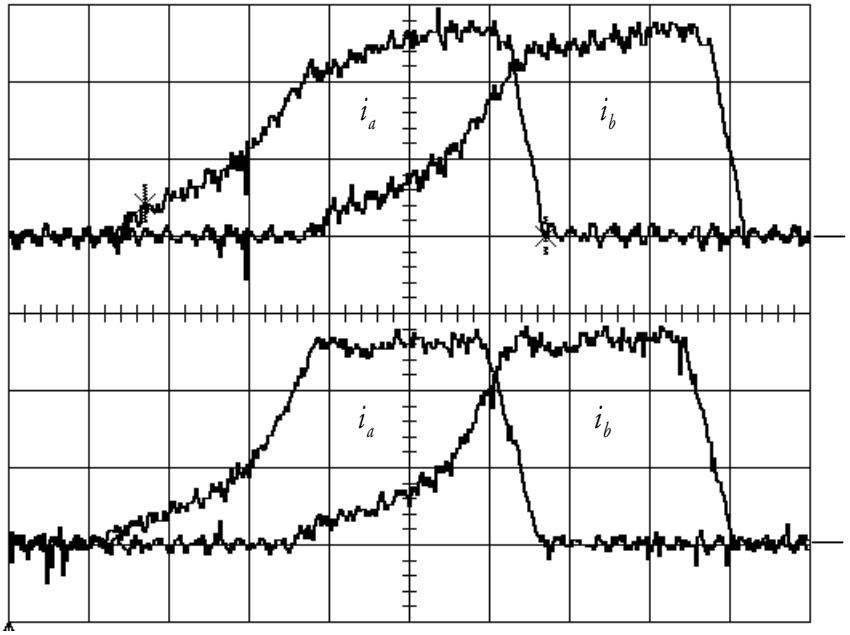

(b) Experimental results

Fig. 4.4 Comparison of the current controllers

4.2 Torque Control Based on Phase Flux Linkages

Torque control based on phase flux linkages is considered in this section. Again, to avoid tedious derivation and deal with the more general case, the dynamics neglecting mutual inductance are not discussed in this section. As discussed in previous section, when i_x, i_y, and θ are chosen as state variables, current controller gains should be adapted according to rotor position. However, if λ_x, λ_y, and θ are chosen as state variables, the gain adaptation can be avoided through a state feedback.

4.2.1 Flux Linkage Feedback

Practically, direct feedback of phase flux linkage is not popular because auxiliary sensing coils or special sensors should be implanted in the machine. Therefore, indirect estimation through current feedback is a preferred alternative. If the phase currents are available and parameters of the machine are well known, the phase flux linkages are estimated from the relationship given in (2.8) as,

$$\begin{aligned} \lambda_x &= L_x i_x + M_{xy} i_y \\ \lambda_y &= M_{xy} i_x + L_y i_y \end{aligned} \tag{4.13}$$

Because no dynamics are involved in this relationship, the phase flux linkages can be easily estimated from the phase currents.

4.2.2 Flux Linkage Control

The dynamic equations for the SRM in terms of phase flux linkages are rewritten for convenience. The flux linkage loop is shown in Fig. 4.5.

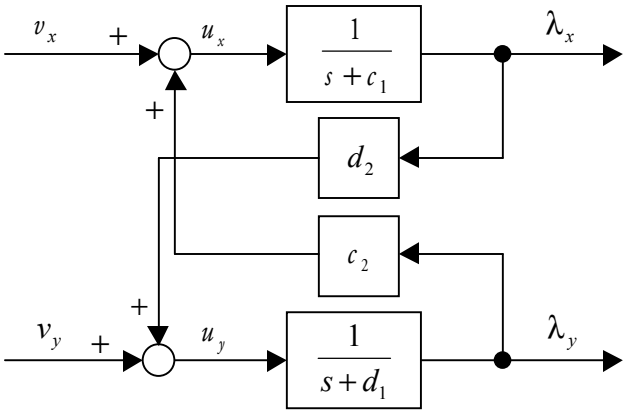

Fig. 4.5 Flux linkage loop

$$\begin{aligned}\frac{d\lambda_x}{dt} &= -c_1\lambda_x + c_2\lambda_y + v_x \\ \frac{d\lambda_y}{dt} &= -d_1\lambda_y + d_2\lambda_x + v_y\end{aligned} \tag{4.13}$$

$$\begin{aligned}\frac{d\omega}{dt} = -\frac{B}{J}\omega + \frac{1}{J}\Bigg[& \frac{1}{2D^2}\left(L_y^2 g_x + M_{xy}^2 g_y - 2M_{xy}L_y g_{xy}\right)\lambda_x^2 \\ & + \frac{1}{2D^2}\left(M_{xy}^2 g_x + L_x^2 g_y - 2M_{xy}L_x g_{xy}\right)\lambda_x^2 \\ & + \frac{1}{D^2}\left\{-M_{xy}L_y g_x - M_{xy}L_x g_y + \left(L_x L_y + M_{xy}^2\right)g_{xy}\right\}\lambda_x\lambda_y\Bigg]\end{aligned} \tag{4.14}$$

As explained in Chapter 3, the advantages of utilizing phase currents as auxiliary state variables are as follows: The simpler output torque equation given in (4.2) can be used instead of the more complex output torque equation given in (4.14) when calculating TDF. More importantly, the first and second terms in the right hand sides of (4.13) can be cancelled without actually calculating those terms. In other words, if the input $\boldsymbol{v} = \begin{bmatrix} v_x & v_y \end{bmatrix}^T$ is defined as,

$$\begin{aligned}v_x &= R_s i_x + u_x \\ v_y &= R_s i_y + u_y\end{aligned} \tag{4.15}$$

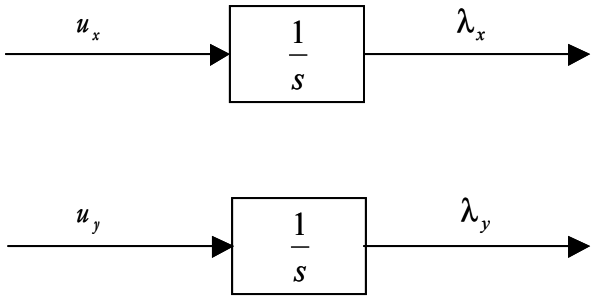

Fig. 4.6 Decoupled flux linkage loop

Where $\boldsymbol{u} = \begin{bmatrix} u_x & u_y \end{bmatrix}^T$ is an equivalent input to be designed. The control law $\boldsymbol{v}$ leads the system (4.13) to a linear system as shown in Fig. 4.6.

$$\begin{aligned} \frac{d\lambda_x}{dt} &= u_x \\ \frac{d\lambda_y}{dt} &= u_y \end{aligned} \tag{4.16}$$

From (2.13), the following relationship is obtained.

$$\begin{aligned} R_s i_x &= c_1 \lambda_x - c_2 \lambda_y \\ R_s i_y &= d_1 \lambda_y - d_2 \lambda_y \end{aligned} \tag{4.17}$$

The two state feedback terms in the right hand sides of (4.13) have time varying coefficients that need not be calculated. Instead, they can be replaced by the left hand side terms of (4.17), which are time invariant and can be used for practical calculations since the coefficients are constant. It should be mentioned that system (4.16) is a linear time invariant system unlike current control loop. Therefore, gain adaptation is not necessary in the flux control loop.

Similarly, to obtain desired transient and steady state performances, the new control inputs u_x and u_y are given by PI controller as,

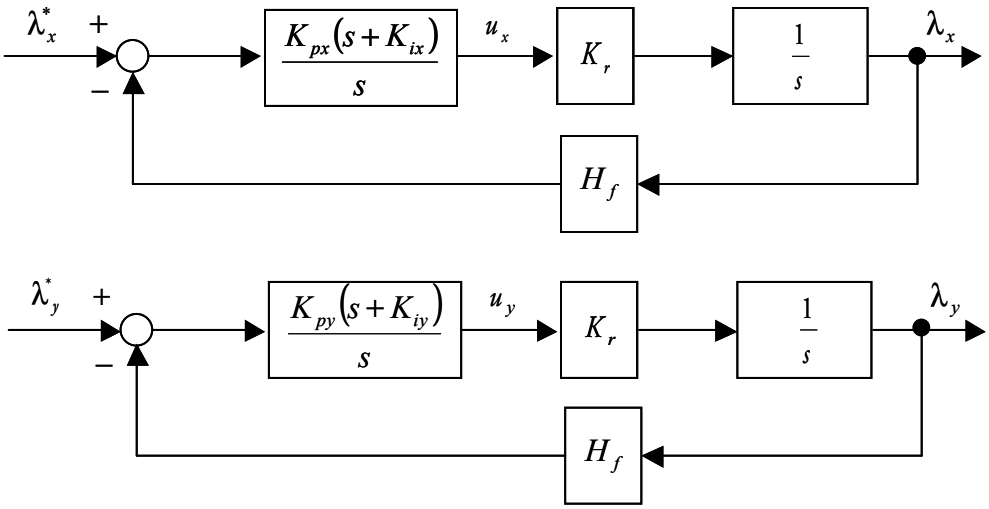

Fig. 4.7 Flux linkage control loop with PI controller

$$
\begin{aligned}
u_x &= K_{px}\left[\left(\lambda_x^* - \lambda_x\right) + K_{ix}\int_0^t \left(\lambda_x^* - \lambda_x\right)d\tau\right] \\
u_y &= K_{py}\left[\left(\lambda_y^* - \lambda_y\right) + K_{iy}\int_0^t \left(\lambda_y^* - \lambda_y\right)d\tau\right]
\end{aligned}
\tag{4.18}
$$

Where K_{px}, K_{py}, K_{ix}, and K_{iy} are the gains of the PI controllers. Again, they can be evaluated by the design procedure based on the frequency response characteristics. The system transfer functions $G_{fx}(s)$ and $G_{fy}(s)$ are derived from Fig. 4.7 as follows.

$$
\begin{aligned}
G_{fx}(s) &\equiv \frac{\lambda_x(s)}{\lambda_x^*(s)} = \frac{1}{H_f}\cdot\frac{H_f K_r K_{px} s + H_f K_r K_{px} K_{ix}}{s^2 + H_f K_r K_{px} s + H_f K_r K_{px} K_{ix}} \\
G_{fy}(s) &\equiv \frac{\lambda_y(s)}{\lambda_y^*(s)} = \frac{1}{H_f}\cdot\frac{H_f K_r K_{py} s + H_f K_r K_{py} K_{iy}}{s^2 + H_f K_r K_{py} s + H_f K_r K_{py} K_{iy}}
\end{aligned}
\tag{4.19}
$$

where,

$$
\begin{aligned}
&H_f : \text{flux linkage feedback gain} \\
&K_r : \text{converter gain}
\end{aligned}
\tag{4.20}
$$

Similarly, for a given set of the bandwidth ω_f and the damping ratio ζ_f, the controller gains are algebraically calculated as,

$$K_{px} = K_{py} = \frac{2\zeta_f \omega_f}{\sqrt{\left(1+2\zeta_f^2\right)+\sqrt{\left(1+2\zeta_f^2\right)^2+1}}} \cdot \frac{1}{H_f K_r}$$
$$K_{ix} = K_{iy} = \frac{\omega_f}{2\zeta_f \sqrt{\left(1+2\zeta_f^2\right)+\sqrt{\left(1+2\zeta_f^2\right)^2+1}}} \tag{4.21}$$

The proportional gains of the flux linkage control loop in (4.21) are not functions of rotor position and they are identical. Therefore, less computation is necessary in the flux linkage control. The stator winding resistance R_s, however, is temperature sensitive and its variation can adversely affect the performance of the flux linkage control loop. To examine the effect of the variation of the stator winding resistance, simulation results are shown in Fig. 4.8. An ideal linear amplifier is assumed as a power converter and it is also assumed that SRM is running at speed of 200 rpm regardless of the electromagnetic torque generated by the phase flux linkages. The gains of the flux linkage controller are set to have a bandwidth of 400 Hz and a damping ratio of 1.

When the estimated stator winding resistance $\hat{R}_s$ is larger than the real stator winding resistance R_s, slower response can be observed while larger overshoot is observed when $\hat{R}_s$ is smaller than R_s as shown in Fig. 4.8. This can be explained by the changes in the system pole locations. In other words, $\hat{R}_s$ can be modeled as,

$$\hat{R}_s = kR_s \tag{4.23}$$

where *k* is an arbitrary positive constant. Then, from (4.17)

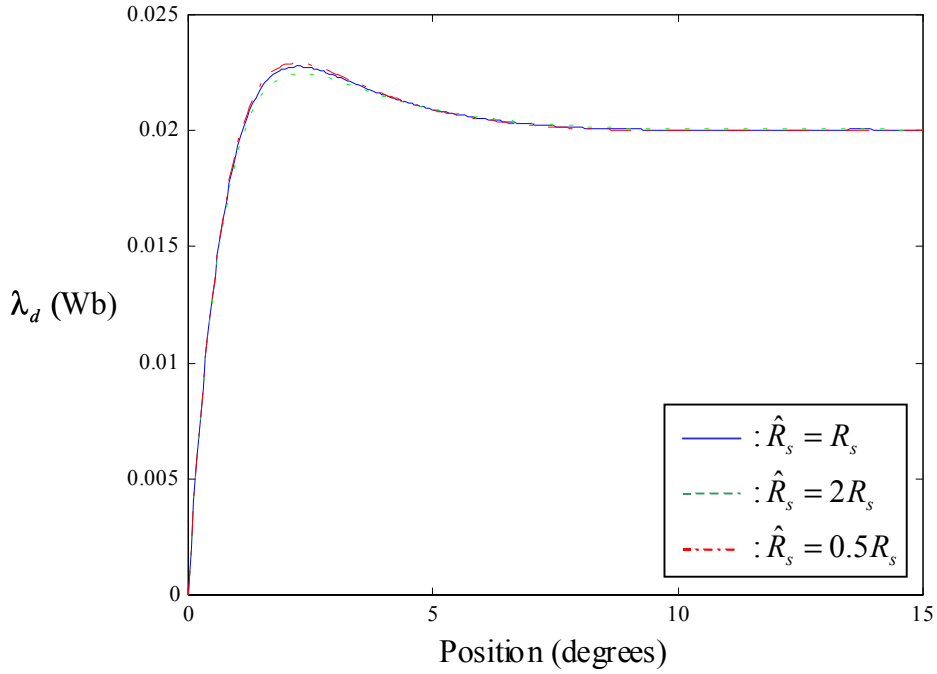

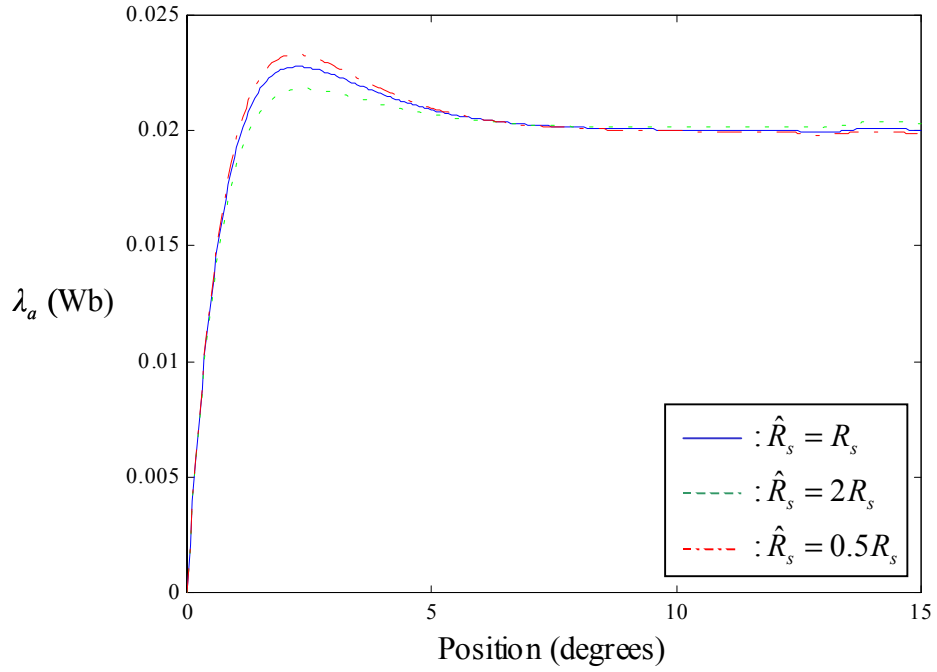

Fig. 4.8 Effect of the variation of the stator winding resistance

$$\hat{R}_s i_x = k\left(c_1\lambda_x - c_2\lambda_y\right)$$
$$\hat{R}_s i_y = k\left(d_1\lambda_y - d_2\lambda_y\right) \tag{4.24}$$

Since $c_1 >> c_2$ and $d_1 >> d_2$, the coupling terms in (4.24) are neglected and the system transfer functions $G_{fx}(s)$ and $G_{fy}(s)$ are derived as,

$$G_{fx}(s) = \frac{1}{H_f} \cdot \frac{H_f K_r K_{px} s + H_f K_r K_{px} K_{ix}}{s^2 + [(1-k)c_1 + H_f K_r K_{px}]s + H_f K_r K_{px} K_{ix}}$$
$$G_{fy}(s) = \frac{1}{H_f} \cdot \frac{H_f K_r K_{py} s + H_f K_r K_{py} K_{iy}}{s^2 + [(1-k)d_1 + H_f K_r K_{px}]s + H_f K_r K_{py} K_{iy}} \tag{4.25}$$

Therefore, the system pole locations are affected by the constant *k.* The effect of the variation of the stator winding resistance is negligible when the ratio of $(1-k)c_1$ or $(1-k)d_1$ to $H_f K_r K_{px}$ is small. However, if the ratio becomes larger, these terms should be considered. Especially when *k* is greater than 1 (estimated stator resistance is greater than the actual stator resistance), care should be taken because one of the system poles can be positive. That is, the system becomes unstable. In this specific application, the response of the flux linkage control loop is not severely affected by the variation of R_s and if the loop bandwidth ω_f is increased to 2 kHz, the effect is negligible.

CHAPTER 5: OPERATION OF THE SRM INCLUDING MAGNETIC SATURATION

Although the analysis of the SRM is initially performed assuming a linear magnetic system, the machine is normally operated in the saturation region. In order to get higher torque from the machine, part of the magnetic circuit is driven into saturation over at least part of the excitation period. The prototype SRM is designed such that it generally operates in the saturation region during the rated operating conditions. Since the saturation makes the coefficients of the differential equations describing the behavior of the SRM to be functions of not only the rotor position but also the phase currents, the generalization of the modeling of the SRM, the proposed TDF, and the current or flux linkage controllers are necessary. The fundamental concept of the proposed TDF and the controllers can be applied with the slight modifications in the torque functions and the introduction of an equivalent self inductance. This chapter focuses on the SRM operation in the entire region. The overlapping descriptions with those of the linear operating region described Chapters 2, 3, and 4 will be omitted so as not cause any ambiguity.

Section 5.1 describes the modeling of the SRM taking the machine saturation into consideration. The parameters of the machine such as self and mutual inductances are obtained for different rotor positions and phase currents. The self inductance of phase a, L_a and the mutual inductance between phase d and a, M_{da} have been measured and compared with the results of FEA in Section 2.2. Torque functions are newly defined, as is an equivalent self inductance to account for the effects of saturation. In Section 5.2, the proposed TDF described in Chapter 3 is modified such that the saturation effects on the machine are considered. Inductances and torque functions in an excitation region are also examined to assess the effects of the magnetic saturation on them. Section 5.3 describes the modification of torque controllers based on both the phase currents and flux linkages. By the introducing an equivalent self inductance, the gains of the proposed current controller have the same forms as those of the linear magnetic system.

5.1 Modeling of the SRM

5.1.1 Parameters

In previous chapters, parameters were obtained when phase currents are equal to 1.2 A. If the phase current exceeds about 1.2 A, the magnetic circuit of the prototype SRM becomes saturated when the rotor moves towards the aligned position. Therefore, the inductances are no longer determined only by rotor position. To generalize the previously described concepts of the proposed TDF and the controllers, the general forms of the inductances at any operating condition are represented as (5.1) and (5.2).

$$L_x = L_x(i_x, \theta)$$
$$L_y = L_y(i_y, \theta) \tag{5.1}$$

$$M_{xy} = M_{xy}(i_x, i_y, \theta) \tag{5.2}$$

Note here that because the leakage path of the magnetic circuit predominantly determines the mutual inductance, the self inductance of a phase is not severely affected by the adjacent phase current. Therefore, only the rotor position and related phase current determine the self inductance of a phase. However, rotor position and two adjacent phase currents determine the mutual inductance as given in (5.2) although the variation in the mutual inductance due to the phase currents is practically negligible. There is no variation in the self inductance when the rotor is unaligned but it significantly decreases when the rotor is near the aligned position. The variation in the mutual inductance is not significant compared with the variation in the self inductance. For example, $L_{a,\max}$ at $i_a = 2.0\text{A}$ and $M_{da,\max}$ at $i_d = 0\text{A}$ and $i_a = 2.0\text{A}$ are 79.4% of $L_{a,\max}$ at $i_a = 1.2\text{A}$ and 95.9% of $M_{da,\max}$ at $i_d = 0\text{A}$ and $i_a = 1.2\text{A}$, respectively.

The torque functions are equivalent to the rates of change of inductances with respect to rotor position when the SRM is operated in the linear magnetic region. If the magnetic circuit is saturated, the torque equation given in (2.18) no longer holds because inductances are now functions of the phase currents and rotor position. As a result, the coenergy cannot be explicitly

expressed unless the inductances are explicitly expressed in terms of the phase currents and rotor position as,

$$\begin{aligned} W_c(i_x, i_y, \theta) &= \int_0^{i_y} \lambda_y(0, \xi, \theta)\, d\xi + \int_0^{i_x} \lambda_x(\xi, i_y, \theta)\, d\xi \\ &= \int_0^{i_y} L_y(\xi, \theta)\xi\, d\xi + \int_0^{i_x} \left(L_x(\xi, \theta)\xi + M_{xy}(\xi, i_y, \theta) i_y\right) d\xi \\ &= \int_0^{i_x} L_x(\xi, \theta)\xi\, d\xi + \int_0^{i_y} L_y(\xi, \theta)\xi\, d\xi + \int_0^{i_x} M_{xy}(\xi, i_y, \theta) i_y\, d\xi \end{aligned} \tag{5.3}$$

Where ξ is an integration variable. Therefore, the torque function should be redefined in a more general way. The coenergy has three distinct components and each represents the coenergy related to the three inductances. It is apparent that the first and second component are the coenergies related to L_x and L_y, and the last one is the coenergy related to M_{xy}. To have the similar form of the output torque expression given in (2.18), these components are expressed as,

$$\begin{aligned} &\int_0^{i_x} L_x(\xi, \theta)\xi\, d\xi = \frac{1}{2} K_x(i_x, \theta) i_x^2 \\ &\int_0^{i_y} L_y(\xi, \theta)\xi\, d\xi = \frac{1}{2} K_y(i_y, \theta) i_y^2 \\ &\int_0^{i_x} M_{xy}(\xi, i_y, \theta) i_y\, d\xi = K_{xy}(i_x, i_y, \theta) i_x i_y \end{aligned} \tag{5.4}$$

Where $K_x(i_x, \theta)$, $K_y(i_y, \theta)$, and $K_{xy}(i_x, i_y, \theta)$ are arbitrary functions determined by each integral given in (5.4). Then, T_e is calculated as,

$$T_e = \left.\frac{\partial W_c(i_x, i_y, \vartheta)}{\partial \theta}\right|_{i_x, i_y \text{ fixed}} = T_x(i_x, \theta) + T_y(i_y, \theta) + T_{xy}(i_x, i_y, \theta) \tag{5.5}$$

where,

$$
\begin{aligned}
T_x(i_x,\theta) &= \frac{1}{2}\frac{\partial K_x(i_x,\theta)}{\partial\theta} i_x^2 \\
T_y(i_y,\theta) &= \frac{1}{2}\frac{\partial K_y(i_y,\theta)}{\partial\theta} i_y^2 \\
T_{xy}(i_x,i_y,\theta) &= \frac{\partial K_{xy}(i_x,i_y,\theta)}{\partial\theta} i_x i_y
\end{aligned}
\tag{5.6}
$$

The new torque functions are defined as,

$$
\begin{aligned}
\mathrm{g}'_{\mathrm{x}}(i_x,\theta) &= \frac{\partial K_x(i_x,\theta)}{\partial\theta} \\
\mathrm{g}'_{\mathrm{y}}(i_y,\theta) &= \frac{\partial K_y(i_y,\theta)}{\partial\theta} \\
\mathrm{g}'_{\mathrm{xy}}(i_x,i_y,\theta) &= \frac{\partial K_{xy}(i_x,i_y,\theta)}{\partial\theta}
\end{aligned}
\tag{5.7}
$$

Note that g'_x and g'_y are the self torque functions and g'_{xy} is the mutual torque function. There are two ways to obtain these torque functions. One way is through numerical integration and partial differentiation using (5.4) and (5.7), respectively. Another way is through the algebraic calculation given in (5.8). Individual torque components $T_x(i_x,\theta)$, $T_y(i_y,\theta)$, and $T_{xy}(i_x,i_y,\theta)$ are obtainable from the FEA results. If $i_x \neq 0$ and $i_y \neq 0$, the new torque functions are calculated as,

$$
\begin{aligned}
g'_x(i_x,\theta) &= \frac{2T_x(i_x,\theta)}{i_x^2} \\
g'_y(i_y,\theta) &= \frac{2T_y(i_y,\theta)}{i_y^2} \\
g'_{xy}(i_x,i_y,\theta) &= \frac{T_{xy}(i_x,i_y,\theta)}{i_x i_y}
\end{aligned}
\tag{5.8}
$$

The self and mutual inductance at various current levels are shown in Fig. 5.1(a) and Fig. 5.1(b), respectively. The lower and upper current levels are 1.2 and 2.0 A, respectively; the current being successively incremented by 0.2 A. When the magnetic circuit is saturated, the self

inductance severely decreases around the aligned position, whereas the mutual inductance decreases slightly. Practically, the mutual inductance can be considered as a function of rotor position due to the small variation in the mutual inductance. It can be captured in two-dimensional tables unlike other parameters that are functions of two variables such as rotor position and related phase current.

The torque functions at different conditions are shown in Fig. 5.2. It should be noted that at the same phase current levels, these parameters have the same properties described in (2.2) and (2.3). As a result, the same reasoning used in Chapter 3 can be applied to derive a TDF. In addition to the torque functions, the rates of change of inductances with respect to rotor position shown in Fig. 5.3 are also obtained to derive the dynamic equations describing the behavior of the SRM. From Fig. 5.2 and 5.3, it is evident that the torque functions g'_x and g'_{xy} are equal to the rates of change of inductances with respect to rotor positions $\partial L_x / \partial \theta$ and $\partial M_{xy} / \partial \theta$, respectively, when the magnetic circuit is not saturated. Note here that the torque functions are less affected by the phase current than the rates of change of inductances with respect to rotor position. Similarly, the variations in parameters related to the mutual inductances are small enough to be neglected.

To calculate the equivalent self inductance, that will be described in the following section, the rate of change of self inductance with respect to phase current shown in Fig. 5.4(a) is also calculated. The rate of change of mutual inductance with respect to phase current is also shown in Fig. 5.4(b). However, by considering the ratio of the mutual inductance to the related self inductances, the rate of change of mutual inductance with respect to phase current can be neglected due to small variation.

From Figs. 5.1, 5.2, and 5.3, it has been shown that the variations in parameters related to the mutual inductances are small enough to be neglected. Since the variations are different when different set of phase currents is applied, they are examined as phase currents are applied to the related phases. It will be examined in Section 5.2

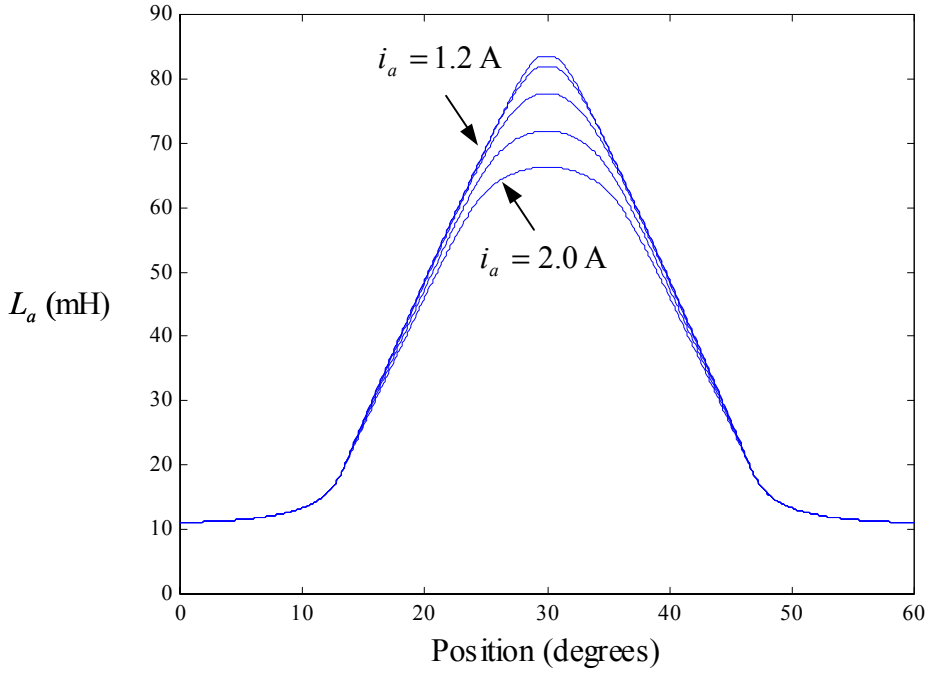

(a) $L_a(i_a, \theta)$

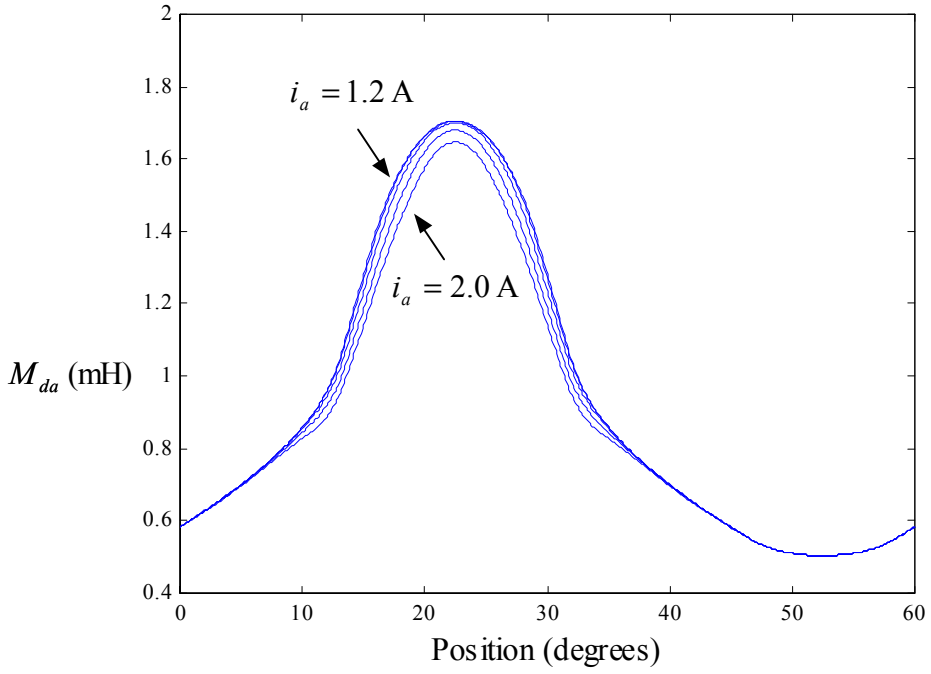

(b) $M_{da}(i_a, 0, \theta)$

Fig. 5.1 Inductances at various current levels

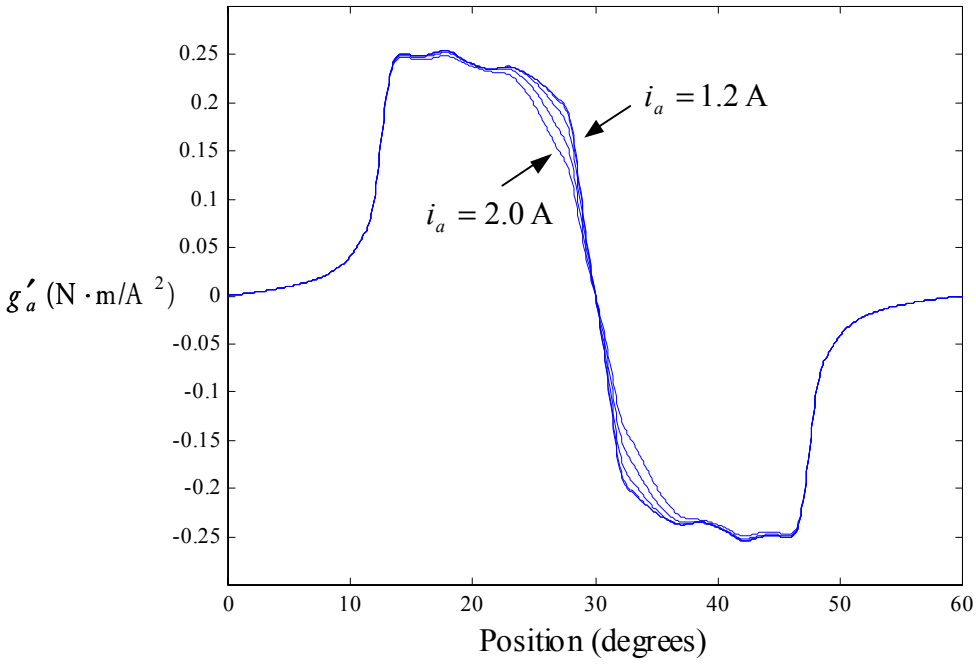

(a) Self torque function $g'_a(i_a, \theta)$

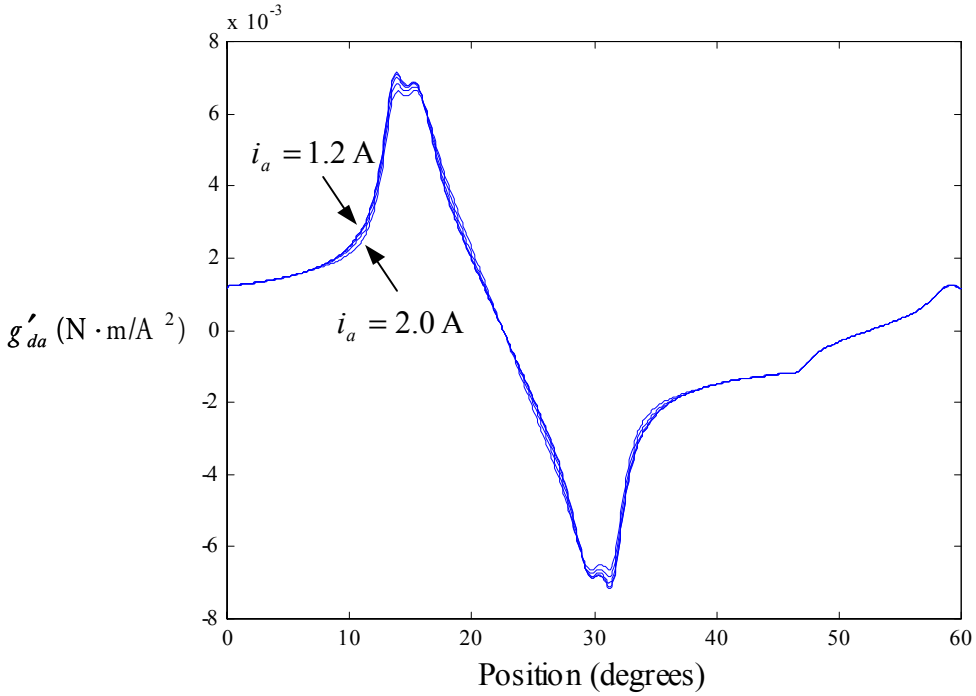

(b) Mutual torque function $g'_{da}(0, i_a, \theta)$

Fig. 5.2 Torque functions at various current levels

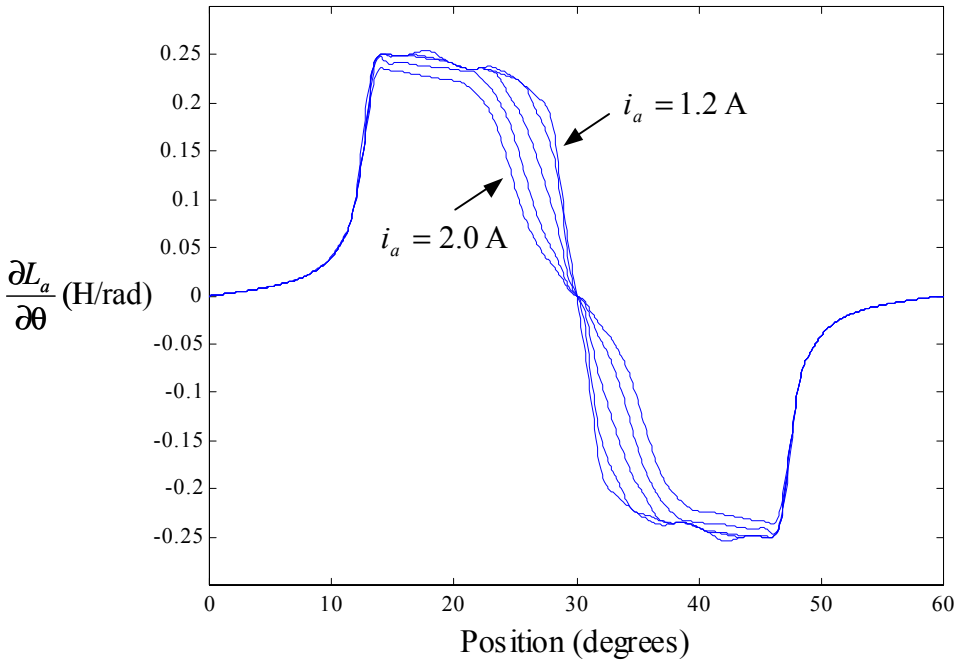

(a) $\partial L_a(i_a, \theta)/\partial\theta$

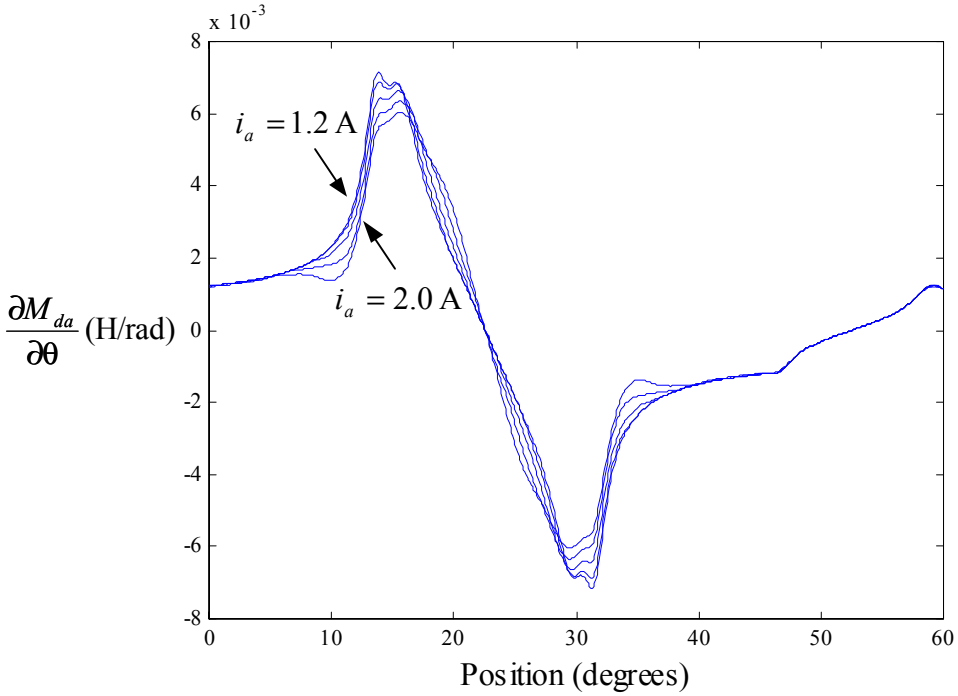

(b) $\partial M_{da}(0, i_a, \theta)/\partial\theta$

Fig. 5.3 Rates of change of inductances with respect to rotor position at various current levels

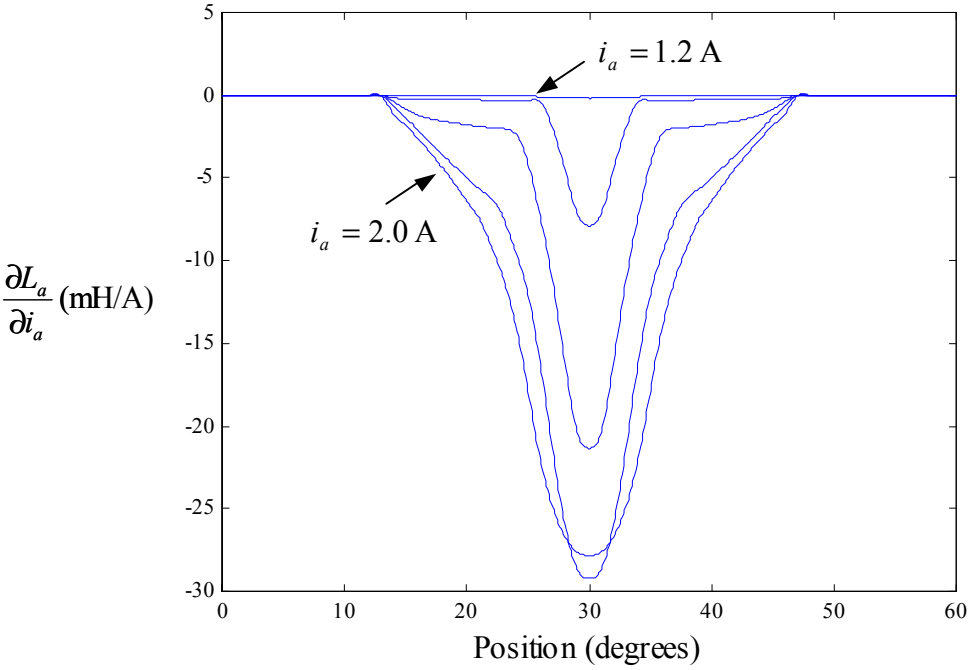

(a) $\partial L_a(i_a, \theta)/\partial i_a$

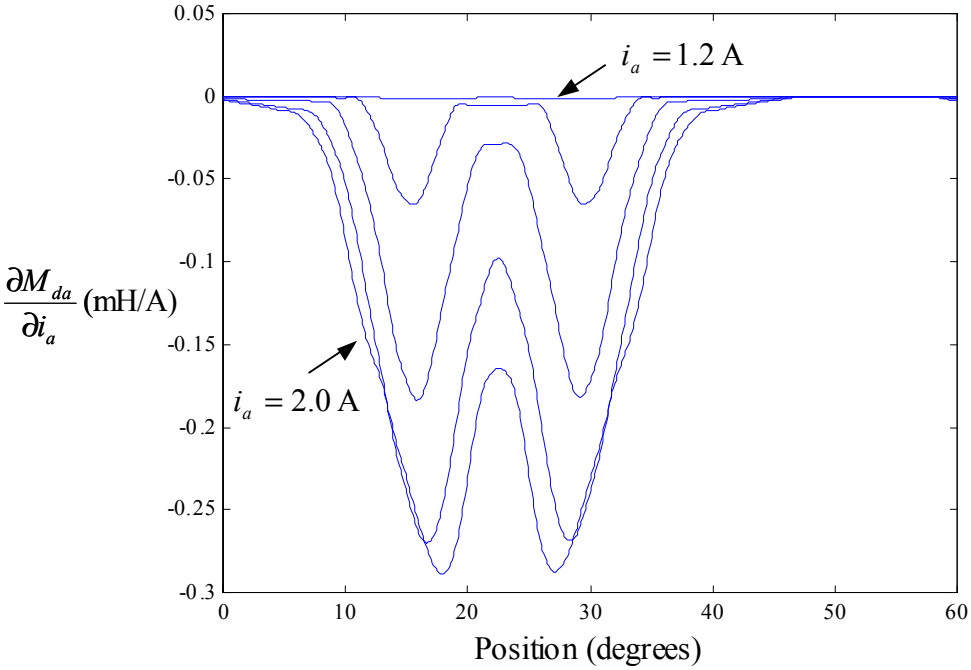

(b) $\partial M_{da}(0, i_a, \theta)/\partial i_a$

Fig. 5.4 Rates of change of inductances with respect to phase current at various current levels

5.1.2 Voltage Equations

First, the voltage equations in terms of the phase current are considered. Equations (2.7) and (2.8) are rewritten for convenience. But the phase flux linkages are now functions of phase currents and rotor position and given as,

$$\begin{aligned} v_x &= R_s i_x + \frac{d\lambda_x}{dt} \\ v_y &= R_s i_y + \frac{d\lambda_y}{dt} \end{aligned} \tag{5.9}$$

where,

$$\begin{aligned} \lambda_x(i_x, i_y, \theta) &\cong L_x(i_x, \theta) i_x + M_{xy}(i_x, i_y, \theta) i_y \\ \lambda_y(i_x, i_y, \theta) &\cong M_{xy}(i_x, i_y, \theta) i_x + L_y(i_y, \theta) i_y \end{aligned} \tag{5.10}$$

The flux linkages can be approximated as (5.10) because the self inductance of a phase is not severely affected by the adjacent phase current, $L_x(i_x, \theta) i_x >> M_{xy}(i_x, i_y, \theta) i_y$, and $L_y(i_y, \theta) i_y >> M_{xy}(i_x, i_y, \theta) i_y$. Since $\partial M_{xy} / \partial i_x$ and $\partial M_{xy} / \partial i_y$ are negligible, by differentiating (5.10) we have

$$\begin{aligned} \frac{d\lambda_x}{dt} &= \left(L_x + \frac{\partial L_x}{\partial i_x} i_x \right) \frac{di_x}{dt} + \frac{\partial L_x}{\partial \theta} \omega i_x + M_{xy} \frac{di_y}{dt} + \frac{\partial M_{xy}}{\partial \theta} \omega i_y \\ \frac{d\lambda_y}{dt} &= M_{xy} \frac{di_x}{dt} + \frac{\partial M_{xy}}{\partial \theta} \omega i_x + \left(L_y + \frac{\partial L_y}{\partial i_y} i_y \right) \frac{di_y}{dt} + \frac{\partial L_y}{\partial \theta} \omega i_y \end{aligned} \tag{5.11}$$

When (5.11) is compared with (2.9), the coefficients of the first term of the first equation and the third term of the second equation in the right hand side are the only differences. The equivalent self inductance is defined to describe the voltage equations in the entire region. If the equivalent self inductances L_x' and L_y' are defined as,

$$L_x' = L_x + \frac{\partial L_x}{\partial i_x} i_x$$
$$L_y' = L_y + \frac{\partial L_y}{\partial i_y} i_y \tag{5.12}$$

It is evident that the equivalent self inductances are equal to the self inductances when the related phase currents are less than 1.2 A. Then, substituting (5.11) into (5.9) yields,

Modified Dynamic Equation I:

$$\frac{di_x}{dt} = -a_1' i_x - a_2' \omega i_x + a_3' i_y + a_4' \omega i_y + a_0' \left(v_x - \frac{M_{xy}}{L_y'} v_y \right)$$
$$\frac{di_y}{dt} = -b_1' i_y - b_2' \omega i_y + b_3' i_x + b_4' \omega i_x + b_0' \left(-\frac{M_{xy}}{L_x'} v_x + v_y \right) \tag{5.13}$$

where,

$$D' = L_x' L_y' - M_{xy}^2 \tag{5.14}$$

$$a_0' = \frac{L_y'}{D'} \qquad b_0' = \frac{L_x'}{D'}$$

$$a_1' = a_0' R_s \qquad b_1' = b_0' R_s$$

$$a_2' = a_0' \left(\frac{\partial L_x}{\partial \theta} - \frac{M_{xy}}{L_y'} \cdot \frac{\partial M_{xy}}{\partial \theta} \right) \qquad b_2' = b_0' \left(\frac{\partial L_y}{\partial \theta} - \frac{M_{xy}}{L_x'} \cdot \frac{\partial M_{xy}}{\partial \theta} \right) \tag{5.15}$$

$$a_3' = a_0' \frac{M_{xy} R_s}{L_y'} \qquad b_3' = b_0' \frac{M_{xy} R_s}{L_x'}$$

$$a_4' = a_0' \left(\frac{M_{xy}}{L_y'} \cdot \frac{\partial L_y}{\partial \theta} - \frac{\partial M_{xy}}{\partial \theta} \right) \qquad b_4' = b_0' \left(\frac{M_{xy}}{L_x'} \cdot \frac{\partial L_x}{\partial \theta} - \frac{\partial M_{xy}}{\partial \theta} \right)$$

The voltage equations in terms of the phase flux linkages are the same form as in (2.14) and (2.15) although the SRM is operating in the entire region. The only difference is that the coefficients are now functions of the phase currents and rotor position.

$$\frac{d\lambda_x}{dt} = -c_1\lambda_x + c_2\lambda_y + v_x$$
$$\frac{d\lambda_y}{dt} = -d_1\lambda_y + d_2\lambda_x + v_y \tag{5.16}$$

where,

$$D = L_x L_y - M_{xy}^2 \tag{5.17}$$

$$c_1 = \frac{L_y}{D}R_s \qquad d_1 = \frac{M_{xy}}{D}R_s$$
$$c_2 = \frac{M_{xy}}{D}R_s \quad d_2 = \frac{L_x}{D}R_s \tag{5.18}$$

5.2 TDF

With the newly defined torque functions, three torque components and TDF are similarly defined as,

$$T_e(i_x, i_y, \theta) = T_x(i_x, \theta) + T_y(i_y, \theta) + T_{xy}(i_x, i_y, \theta) \tag{5.19}$$

where,

$$T_x(i_x, \theta) = \frac{1}{2}g'_x(i_x, \theta)i_x^2 = f_x(i_x, \theta)T_e$$
$$T_y(i_y, \theta) = \frac{1}{2}g'_y(i_y, \theta)i_y^2 = f_y(i_y, \theta)T_e \tag{5.20}$$
$$T_{xy}(i_x, i_y, \theta) = g'_{xy}(i_x, i_y, \theta)i_x i_y = f_{xy}(i_x, i_y, \theta)T_e$$

Then, the modified TDF are defined as,

$$f_x(i_x, i_{y,}\theta) = \frac{g'^2_x(i_{x,}\theta)}{g'^2_x(i_x, \theta) + g'^2_y(i_{y,}\theta) \pm 2g'_{xy}(i_x, i_{y,}\theta)\sqrt{g'_x(i_x, \theta)g'_y(i_{y,}\theta)}}$$
$$f_y(i_x, i_{y,}\theta) = \frac{g'^2_y(i_{y,}\theta)}{g'^2_x(i_x, \theta) + g'^2_y(i_{y,}\theta) \pm 2g'_{xy}(i_x, i_{y,}\theta)\sqrt{g'_x(i_x, \theta)g'_y(i_{y,}\theta)}} \tag{5.21}$$

$$f_{xy}(i_x, i_{y,}\theta) = \frac{2g'_{xy}(i_x, i_{y,}\theta)\sqrt{g'_x(i_x,\theta)g'_y(i_{y,}\theta)}}{g'^2_x(i_x,\theta) + g'^2_y(i_{y,}\theta) \pm 2g'_{xy}(i_x, i_{y,}\theta)\sqrt{g'_x(i_x,\theta)g'_y(i_{y,}\theta)}} \tag{5.22}$$

This TDF also satisfies Constraint II given in (3.13). From (5.19) - (5.22), for a given torque T_e, phase currents are calculated as,

$$\begin{aligned} i_x &= \sqrt{\frac{2T_e g'_x}{g'^2_x + g'^2_y \pm 2g'_{xy}\sqrt{g'_x g'_y}}} \\ i_y &= \sqrt{\frac{2T_e g'_y}{g'^2_x + g'^2_y \pm 2g'_{xy}\sqrt{g'_x g'_y}}} \end{aligned} \tag{5.23}$$

From (5.10) and (5.23), the phase flux linkages are calculated as,

$$\begin{aligned} \lambda_x &= L_x\sqrt{\frac{2g'_x T_e}{g'^2_x + g'^2_y \pm 2g'_{xy}\sqrt{g'_x g'_y}}} + M_{xy}\sqrt{\frac{2g'_y T_e}{g'^2_x + g'^2_y \pm 2g'_{xy}\sqrt{g'_x g'_y}}} \\ \lambda_y &= M_{xy}\sqrt{\frac{2g'_x T_e}{g'^2_x + g'^2_y \pm 2g'_{xy}\sqrt{g'_x g'_y}}} + L_y\sqrt{\frac{2g'_y T_e}{g'^2_x + g'^2_y \pm 2g'_{xy}\sqrt{g'_x g'_y}}} \end{aligned} \tag{5.24}$$

The modified TDF II in an excitation period is summarized in Table 5.1 and shown in Fig. 5.5. The resultant phase currents and flux linkages at T_e^*=0.4 N·m are shown in Fig. 5.6. When compared with the resultant phase currents and flux linkages at T_e^*=0.2 N·m shown in Fig. 3.5, the waveforms of the phase current and flux linkages become less smooth especially around the interval where the two adjacent phase currents or flux linkages intersect. From these figures, it can be deduced that the performance of the current controller or the flux linkage controller can be degraded by the increased di/dt or $d\lambda/dt$ at T_e^*=0.4 N·m. The resultant inductances by the phase currents given in Fig. 5.6 in an excitation period at T_e^*=0.4 N·m are shown in Fig. 5.7. Since the phase *a* is excited only for the first half of the excitation period, there are no variations in the second half of the excitation period.

TABLE 5.1 Modified TDF II in an excitation period

	$T_e^* \geq 0$		$T_e^* < 0$	
f_a	$\frac{g_a'^2}{g_d'^2 + g_a'^2 + 2g_{da}' \sqrt{g_d' g_a'}}$	for $0^\circ \leq \theta < 15^\circ$	0	for $0^\circ \leq \theta < 15^\circ$
	$\frac{g_a'^2}{g_a'^2 + g_b'^2 + 2g_{ab}' \sqrt{g_a' g_b'}}$	for $15^\circ \leq \theta < 30^\circ$	0	for $15^\circ \leq \theta < 30^\circ$
	0	for $30^\circ \leq \theta < 45^\circ$	$\frac{g_a'^2}{g_d'^2 + g_a'^2 - 2g_{da}' \sqrt{g_d' g_a'}}$	for $30^\circ \leq \theta < 45^\circ$
	0	for $45^\circ \leq \theta < 60^\circ$	$\frac{g_a'^2}{g_a'^2 + g_b'^2 - 2g_{ab}' \sqrt{g_a' g_b'}}$	for $45^\circ \leq \theta < 60^\circ$
f_b	0	for $0^\circ \leq \theta < 15^\circ$	$\frac{g_b^2}{g_b'^2 + g_c'^2 - 2g_{bc}' \sqrt{g_b' g_c'}}$	for $0^\circ \leq \theta < 15^\circ$
	$\frac{g_b'^2}{g_a'^2 + g_b'^2 + 2g_{ab}' \sqrt{g_a' g_b'}}$	for $15^\circ \leq \theta < 30^\circ$	0	for $15^\circ \leq \theta < 30^\circ$
	$\frac{g_b^2}{g_b'^2 + g_c'^2 + 2g_{bc}' \sqrt{g_b' g_c'}}$	for $30^\circ \leq \theta < 45^\circ$	0	for $30^\circ \leq \theta < 45^\circ$
	0	for $45^\circ \leq \theta < 60^\circ$	$\frac{g_b'^2}{g_a'^2 + g_b'^2 - 2g_{ab}' \sqrt{g_a' g_b'}}$	for $45^\circ \leq \theta < 60^\circ$
f_c	0	for $0^\circ \leq \theta < 15^\circ$	$\frac{g_c'^2}{g_b'^2 + g_c'^2 - 2g_{bc}' \sqrt{g_b' g_c'}}$	for $0^\circ \leq \theta < 15^\circ$
	0	for $15^\circ \leq \theta < 30^\circ$	$\frac{g_c'^2}{g_c'^2 + g_d'^2 - 2g_{cd}' \sqrt{g_c' g_d'}}$	for $15^\circ \leq \theta < 30^\circ$
	$\frac{g_c'^2}{g_b'^2 + g_c'^2 + 2g_{bc}' \sqrt{g_b' g_c'}}$	for $30^\circ \leq \theta < 45^\circ$	0	for $30^\circ \leq \theta < 45^\circ$
	$\frac{g_c'^2}{g_c'^2 + g_d'^2 + 2g_{cd}' \sqrt{g_c' g_d'}}$	for $45^\circ \leq \theta < 60^\circ$	0	for $45^\circ \leq \theta < 60^\circ$
f_d	$\frac{g_d'^2}{g_d'^2 + g_a'^2 + 2g_{da}' \sqrt{g_d' g_a'}}$	for $0^\circ \leq \theta < 15^\circ$	0	for $0^\circ \leq \theta < 15^\circ$
	0	for $15^\circ \leq \theta < 30^\circ$	$\frac{g_d'^2}{g_c'^2 + g_d'^2 - 2g_{cd}' \sqrt{g_c' g_d'}}$	for $15^\circ \leq \theta < 30^\circ$
	0	for $30^\circ \leq \theta < 45^\circ$	$\frac{g_d'^2}{g_d'^2 + g_a'^2 - 2g_{da}' \sqrt{g_d' g_a'}}$	for $30^\circ \leq \theta < 45^\circ$
	$\frac{g_d'^2}{g_c'^2 + g_d'^2 + 2g_{cd}' \sqrt{g_c' g_d'}}$	for $45^\circ \leq \theta < 60^\circ$	0	for $45^\circ \leq \theta < 60^\circ$

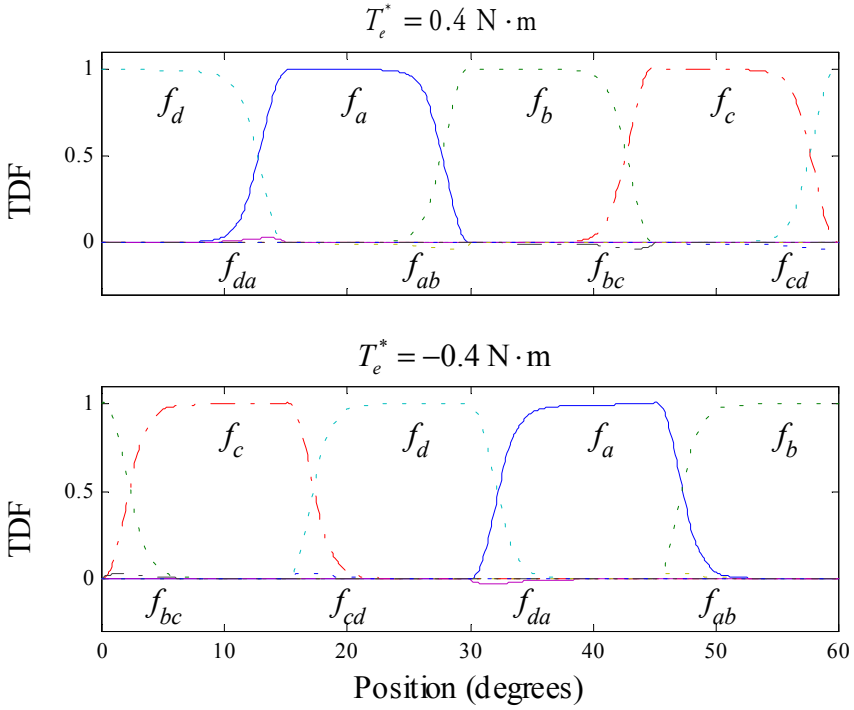

Fig. 5.5 Modified TDF II in an excitation period

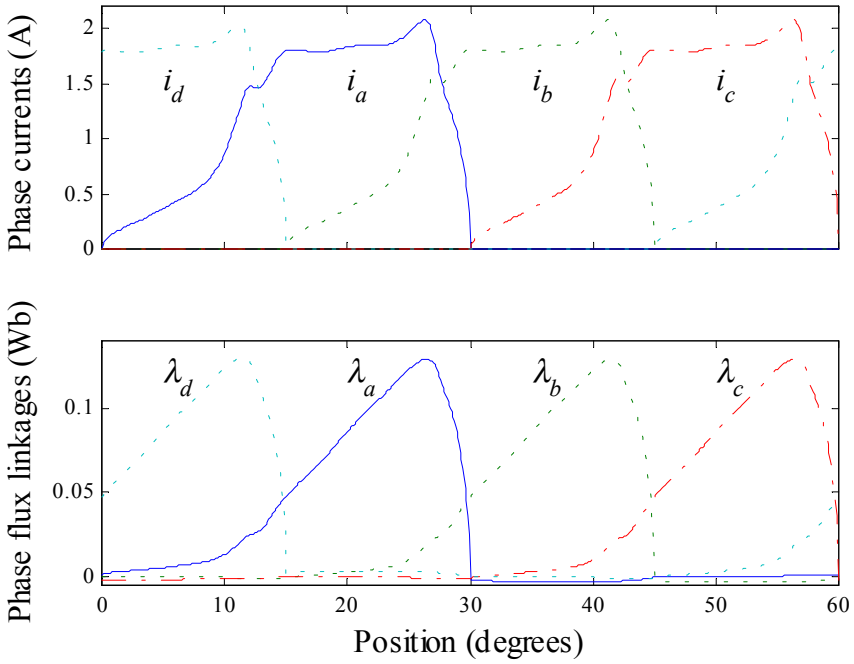

Fig. 5.6 Resultant phase currents and flux linkages by the modified TDF II at T_e^*=0.4 N·m

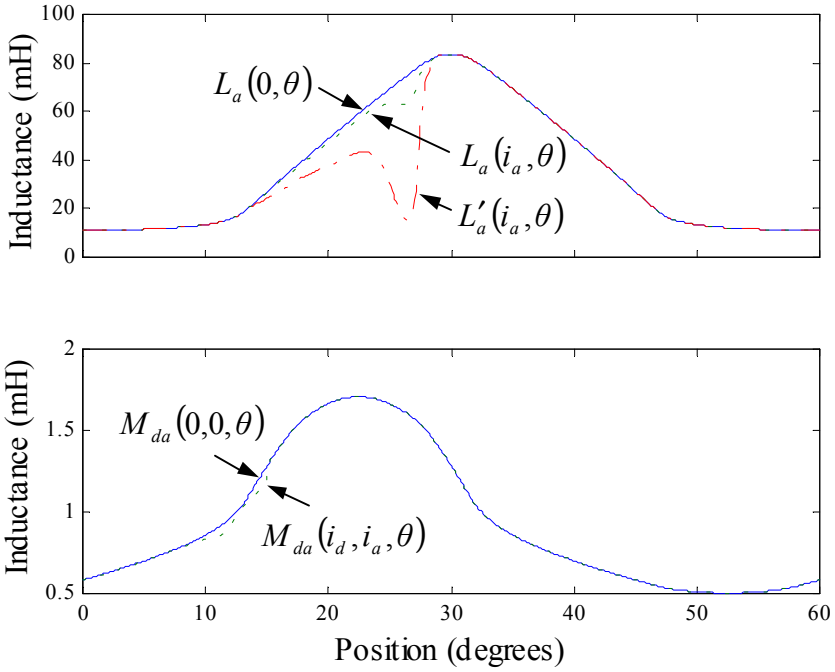

Fig. 5.7 Inductances in an excitation period at T_e^*=0.4 N·m

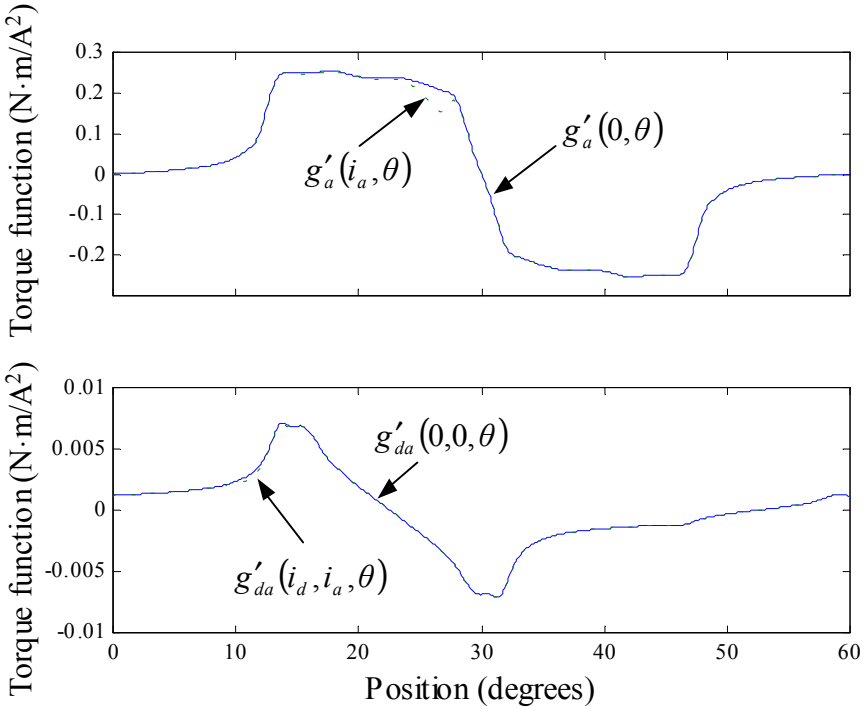

Fig. 5.8 Torque functions in an excitation period at T_e^*=0.4 N·m

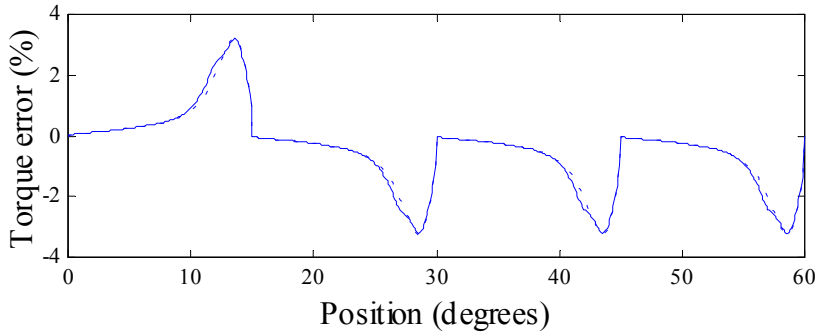

Fig. 5.9 Torque error by the modified TDF I at T_e^*=0.4 N·m

As illustrated in Fig. 5.7, the self inductance and the equivalent self inductance are significantly reduced as the phase current increases and return to their unsaturated values as the phase current decays. Especially, the equivalent self inductance is reduced up to about 20% of the unsaturated self inductance during the excitation period. Therefore, it is essential to consider the variation in the equivalent self inductance in deriving the dynamic equations. On the other hand, the variation in the mutual inductance shown in Fig. 5.7 is negligible.

The self and mutual torque functions in an excitation period are shown in Fig. 5.8. The self torque function is also significantly reduced when the phase current is above 1.2 A whereas the variation in the mutual torque function is small. It should be noted that the variations in the mutual inductance and mutual torque function of the prototype SRM are practically negligible. Therefore, one-dimensional tables can be used for parameters related to the mutual inductance instead of bulky three-dimensional tables. As a result, two-dimensional tables can represent all parameters. It is very important because the three-dimensional tables are not easy to implement due to huge memory requirements.

Fig. 5.9 shows the torque error caused by the modified TDF I at T_e^*=0.4 N·m. The dotted line is the torque error caused by the TDF I at T_e^*=0.2 N·m. The peak-to-peak torque ripple caused by the modified TDF I at T_e^*=0.4 N·m is similar to the ripple caused by the TDF I at T_e^*=0.2 N·m. The modified TDF I is not listed in this section because it can be easily derived from Table 5.4 by letting the mutual torque functions be zeros.

5.3 Torque Control

5.3.1 Torque Control Based on Phase Currents

For the proposed current controller, using the introduced equivalent self inductance, the input transformation matrix $\boldsymbol{E}$ and the control law $\boldsymbol{u} = \begin{bmatrix} u_x & u_y \end{bmatrix}^T$ are generalized as,

$$\boldsymbol{E} = \begin{bmatrix} 1 & -M_{xy}/L'_y \\ -M_{xy}/L'_x & 1 \end{bmatrix} \tag{5.25}$$

$$\begin{bmatrix} u_x \\ u_y \end{bmatrix} = \begin{bmatrix} \left(a'_2 \omega i_x - a'_3 i_y - a'_4 \omega i_y\right)/a'_0 \\ \left(b'_2 \omega i_y - b'_3 i_x - b'_4 \omega i_x\right)/b'_0 \end{bmatrix} + \begin{bmatrix} \bar{u}_x \\ \bar{u}_y \end{bmatrix} \tag{5.26}$$

After similar steps described in Section 4.1, the system transfer functions $G_{cx}(s)$ and $G_{cy}(s)$ are derived as follows.

$$\begin{aligned} G_{cx}(s) \equiv \frac{i_x(s)}{i_x^*(s)} &\cong \frac{1}{H_c} \cdot \frac{K'_{1x}K_{px}s + K'_{1x}K_{px}K_{ix}}{s^2 + K'_{1x}K_{px}s + K'_{1x}K_{px}K_{ix}} \quad \text{for } a'_0 H_c K_r K_{px} >> a'_1 \\ G_{cy}(s) \equiv \frac{i_y(s)}{i_y^*(s)} &\cong \frac{1}{H_c} \cdot \frac{K'_{1y}K_{py}s + K'_{1y}K_{py}K_{iy}}{s^2 + K'_{1y}K_{py}s + K'_{1y}K_{py}K_{iy}} \quad \text{for } b'_0 H_c K_r K_{py} >> b'_1 \end{aligned} \tag{5.27}$$

where,

$$\begin{aligned} K'_{1x}(i_x, i_y, \theta) &= a'_0(i_x, i_y, \theta) H_c K_r \\ K'_{1y}(i_x, i_y, \theta) &= b'_0(i_x, i_y, \theta) H_c K_r \end{aligned} \tag{5.28}$$

Therefore, the controller gains are calculated as,

$$\begin{aligned} K_{px}(i_x, i_y, \theta) &= \frac{2\zeta_c \omega_c}{\sqrt{\left(1 + 2\zeta_c^2\right) + \sqrt{\left(1 + 2\zeta_c^2\right)^2 + 1}}} \cdot \frac{1}{K'_{1x}(i_x, i_y, \theta)} \\ K_{ix} &= \frac{\omega_c}{2\zeta_c \sqrt{\left(1 + 2\zeta_c^2\right) + \sqrt{\left(1 + 2\zeta_c^2\right)^2 + 1}}} \end{aligned} \tag{5.29}$$

$$K_{py}(i_x, i_y, \theta) = \frac{2\zeta_c \omega_c}{\sqrt{\left(1+2\zeta_c^2\right)+\sqrt{\left(1+2\zeta_c^2\right)^2+1}}} \cdot \frac{1}{K'_{1y}(i_{x,} i_y, \theta)}$$
$$K_{iy} = \frac{\omega_c}{2\zeta_c \sqrt{\left(1+2\zeta_c^2\right)+\sqrt{\left(1+2\zeta_c^2\right)^2+1}}} \tag{5.30}$$

When (5.29) and (5.30) are compared with (4.11) and (4.12), $K_{1x}(\theta)$ and $K_{1y}(\theta)$ are replaced by $K'_{1x}(i_x, i_y, \theta)$ and $K'_{1y}(i_x, i_y, \theta)$, respectively.

5.3.2 Torque Control Based on Phase Flux Linkages

For the proposed flux linkage controller, nothing needs to be changed. The only difference is that parameters of (5.10) are now functions of rotor position and phase currents. The flux linkage controller described in Chapter 4 can be used without any modification. This is the main advantage of the proposed flux linkage controller.

CHAPTER 6: CONVERTER TOPOLOGY AND SWITCHING STRATEGIES

In this chapter, two converter topologies, which are capable of operating in two quadrants, are compared and chosen. Although a number of different configurations of converters have been proposed in literature and have been summarized in [6], two of the most popular configurations are only considered. The asymmetric half-bridge converters considered here do not contribute to new innovations in this dissertation but are the most practical and commonly used configurations. They are also the most convenient configurations to test a new switching strategy for the converter. This strategy is named as unipolar switching strategy. It is an original innovation and its advantages are described in this section. The reference is with respect to phase current unless otherwise stated.

6.1 Converter Topology

The converter for the prototype SRM should have the ability to provide a positive voltage loop to increase phase current, a negative voltage loop to decrease phase current, and a zero voltage loop to maintain the desired current level. From the existing converter topologies, the two most popular converter topologies for an 8/6 SRM are the asymmetric half-bridge converters shown in Fig. 6.1. They are capable of providing the three voltage loops [5].

Both converters are capable of operating in two quadrants. The switches and freewheeling diodes for both converters should be rated to withstand the supply voltage and switching transients. However, the current ratings of the upper switches T_{ac} and T_{bd} of the shared switch half-bridge converter must be determined to carry the sum of two phase currents. The upper switches T_{ac} and T_{bd} shown in Fig. 6.1(a) are connected to two phase windings rather than one in the asymmetric half-bridge shown in Fig. 6.1(b).

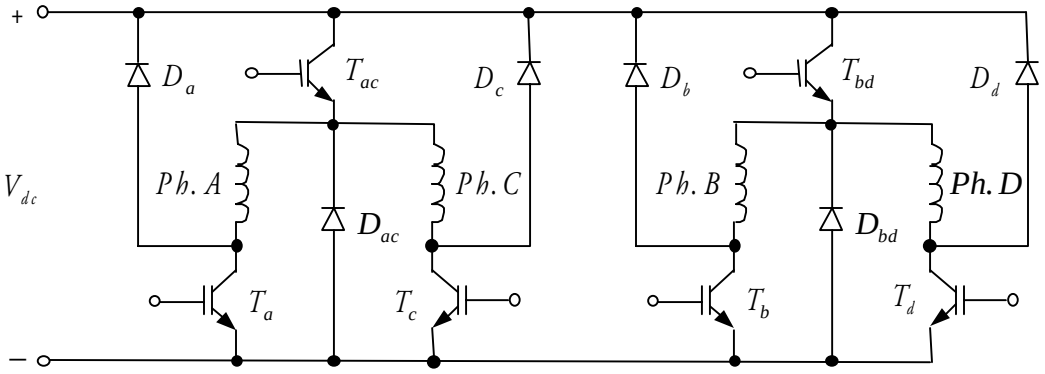

(a) Shared switch asymmetric half-bridge converter

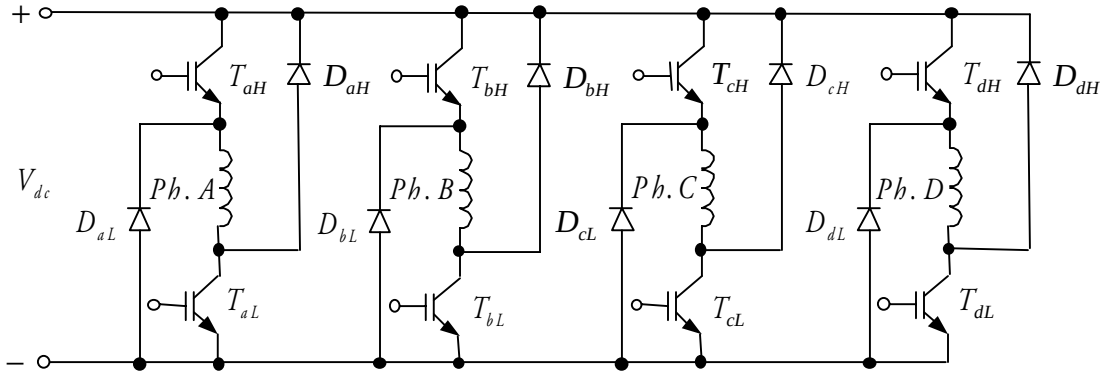

(b) Asymmetric half-bridge converter

Fig. 6.1 Possible converter topologies for the prototype SRM

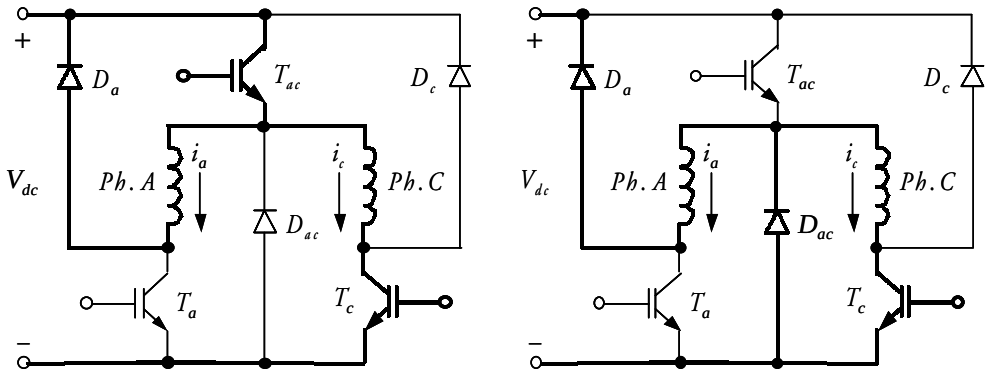

Fig. 6.2 Example of a limited operation of the shared switch asymmetric half-bridge converter

With this configuration, the number of switches and diodes is reduced to six from eight, but it has some operational limitations. The operation of upper switches T_{ac} and T_{bd} affects both the connected phase windings. This imposes a restriction on the operation of the converter because, for example, three phases cannot be operated simultaneously if the situation demands it. In other words, it is not possible to rapidly increase the current in one phase winding while rapidly decreasing the current in the other [5]. For example, when phase *c* is turned on while phase *a* current is remaining, the extinction of phase *a* is largely dependent on the operation of phase *c* as shown in Fig. 6.2. The phase *a* current has an increased fall time, dependent upon the chopping duty cycle of phase *c*. Moreover, when there is a fault in one common switch, the related two phases are not operational while the operation of each phase is independent from that of other phases in the asymmetric half-bridge converter. After reviewing the merits and demerits of these converters, the asymmetric half-bride converter is chosen for the prototype SRM.

6.2 Switching Strategies

To obtain less current ripple and a better frequency response in the inner current control loop of the drive system, a unipolar switching strategy for the half-bridge converter was proposed by the author in [24] and [29].

With the converter shown in Fig. 6.1(b), there are four possible modes of operation for each phase. As an illustration, these modes of operation for phase *a* are shown in Fig. 6.3. In the first mode, switches (T_{aL}, T_{aH}) are turned on with diodes (D_{aL}, D_{aH}) turned off. In this mode, v_a is equal to V_{dc} and the current in the phase winding increases rapidly, supplying energy to the phase winding. In the second mode, if $i_a > 0$, diodes (D_{aL}, D_{aH}) are turned on with switches (T_{aL}, T_{aH}) turned off in which case v_a is equal to $-V_{dc}$. Phase *a* current is forced to flow through both freewheeling diodes and it decreases rapidly as energy is returned from the phase winding to the supply. And if $i_a = 0$, diodes (D_{aL}, D_{aH}) and switches (T_{aL}, T_{aH}) are all turned off in which case v_a is equal to zero. In the last two modes, if $i_a > 0$ switch and diode (T_{aL}, D_{aL}) or

(T_{aH}, D_{aH}) are turned on with switch and diode (T_{aH}, D_{aH}) or (T_{aL}, D_{aL}) turned off, respectively. The phase current continues to flow and decay slowly through one switch and one diode and energy is neither taken from nor returned to the DC supply. And if $i_a = 0$, diodes (D_{aL}, D_{aH}) and switches (T_{aL}, T_{aH}) are all turned off. In both cases, v_a is equal to zero.

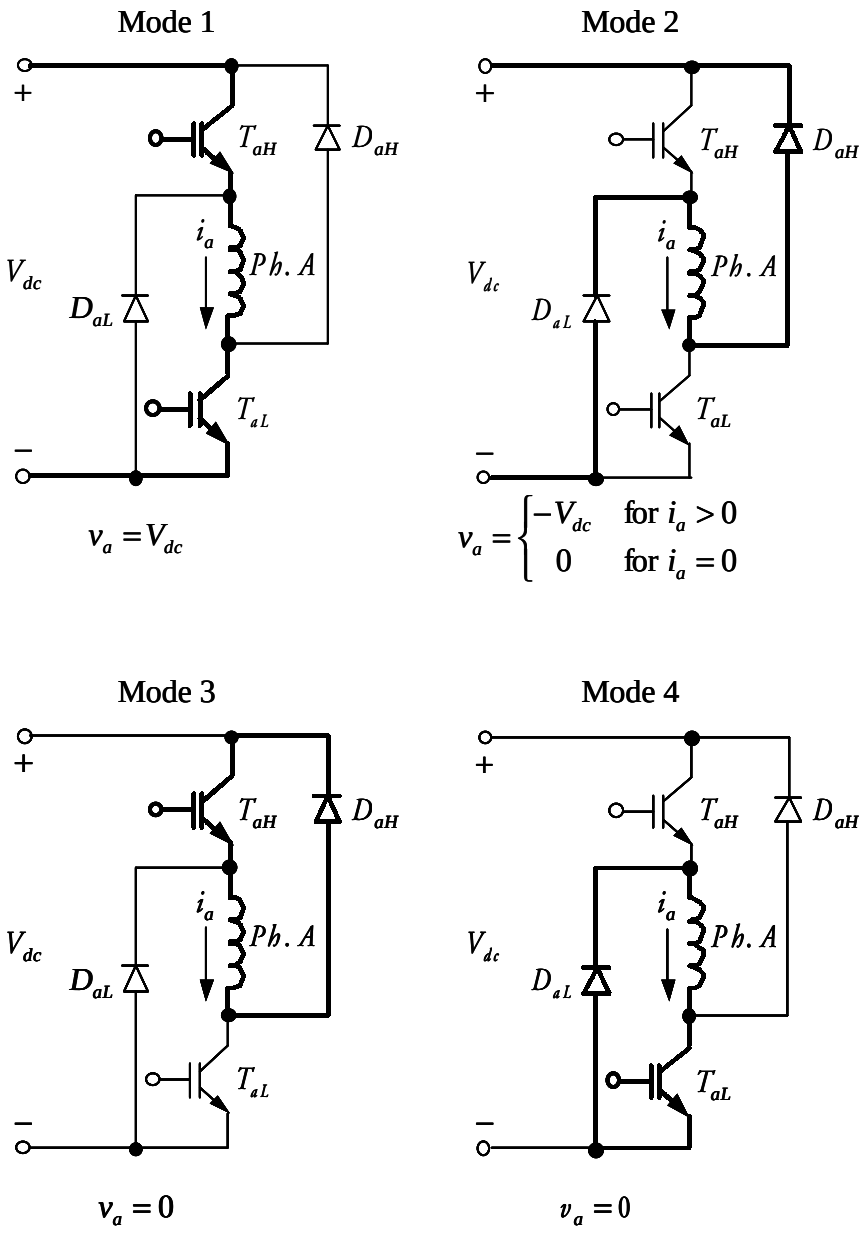

Fig. 6.3 Four possible modes of operation for phase *a*

How to exploit the modes described in Fig. 6.3 entirely depends on design specification but all possible switching strategies applicable to the converter may use some or all of the modes. The last two modes called zero voltage loops are very important in minimizing the ripple contents of the phase current at any given switching frequency. Therefore, they can reduce the hysteresis losses in the motor and the power dissipation in the DC link capacitor during any period when switches in the converter are turned on and off to reduce the net applied voltage to the phase winding.

First, the existing switching strategies, *i.e.* the bipolar and the modified switching strategy are reviewed and then the unipolar switching strategy will be described. For phase *a* operation, switches (T_{aL}, T_{aH}) are activated to control the phase *a* voltage. If switches (T_{aL}, T_{aH}) are treated as a pair, the voltage applied across the phase *a* winding would be V_{dc} for both the switches being on and $-V_{dc}$ for both switches being off with the phase *a* current being greater than zero. This operation is shown in figure 6.4. This switching strategy is identified as the bipolar switching strategy because the phase *a* voltage v_a in Fig. 6.4(a) shows that the voltage is either V_{dc} or $-V_{dc}$ for a given switching cycle. Hence, this switching strategy uses only the first two modes shown in Fig. 6.3. The main drawback of this strategy is there is a larger current ripple when compared with the other two strategies as shown in Fig. 6.5(b) and 6.6(b). The algorithm for the bipolar switching and the average output voltage $[v_a]$ are as follows.

$$v_a = \begin{cases} V_{dc} & \text{for } v_c \geq v_{ramp} \\ -V_{dc} & \text{for } v_c < v_{ramp} \ \& \ i_a > 0 \\ 0 & \text{for } v_c < v_{ramp} \ \& \ i_a = 0 \end{cases} \tag{6.1}$$

$$[v_a] = \frac{V_{dc}}{V_{ramp}} v_c \text{ for } -V_{ramp} \leq v_c \leq V_{ramp}$$
$$-V_{dc} \leq [v_a] \leq V_{dc} \tag{6.2}$$

where,

V_{dc} : DC link voltage

V_{ramp} : peak voltage of the triangular waveform

To examine the response of the bipolar switching strategy, a simulation result is shown in Fig. 6.4(b). The simulation result is obtained at $T_e^* = 0.2\ \mathrm{N \cdot m}$ and $\omega = 1000\ \mathrm{rpm}$ during the first excitation region. The phase current commands, which are indicated by dashed lines in Fig. 6.4(b), are obtained using the TDF II strategy listed in Table 3.2. When the phase winding inductance is small, the ripple contents of the phase currents are too large to be acceptable in applications where high performance is required. Even when the phase winding inductance is large, the ripple contents are still large compared with other two switching strategies.

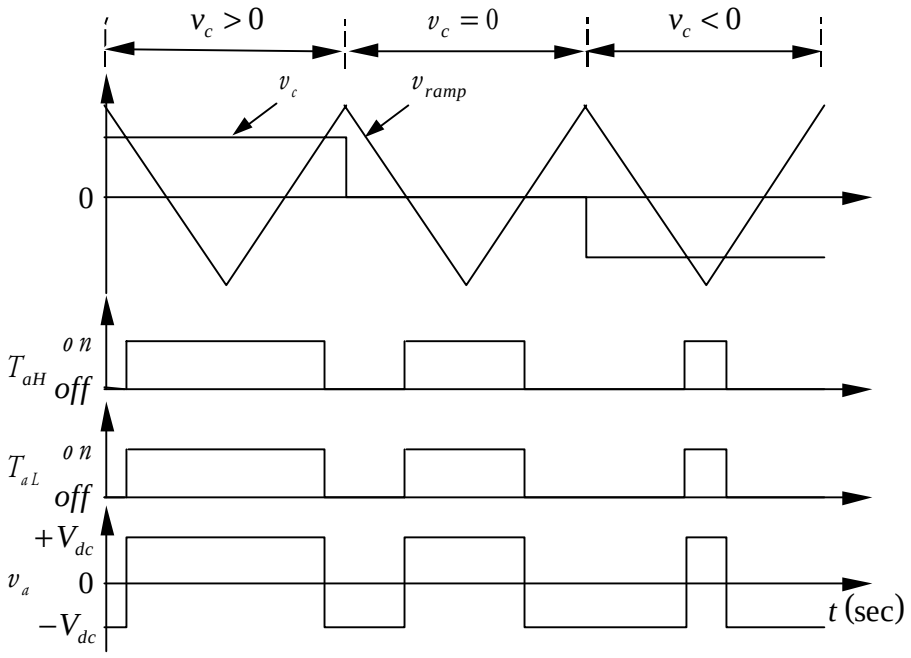

(a) Operational principle

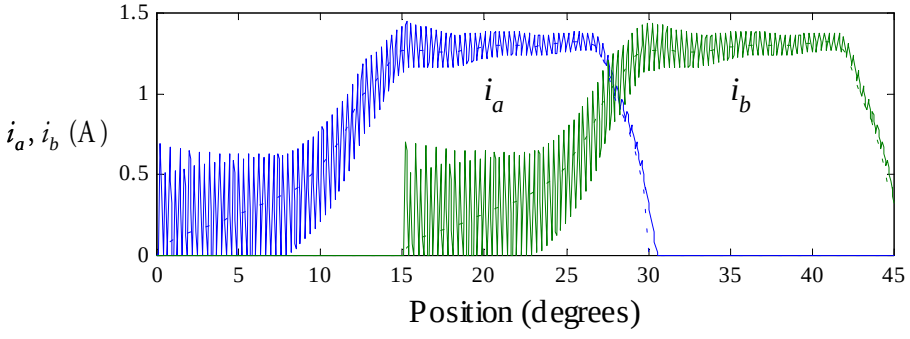

(b) Simulation results

Fig. 6.4 Bipolar switching strategy

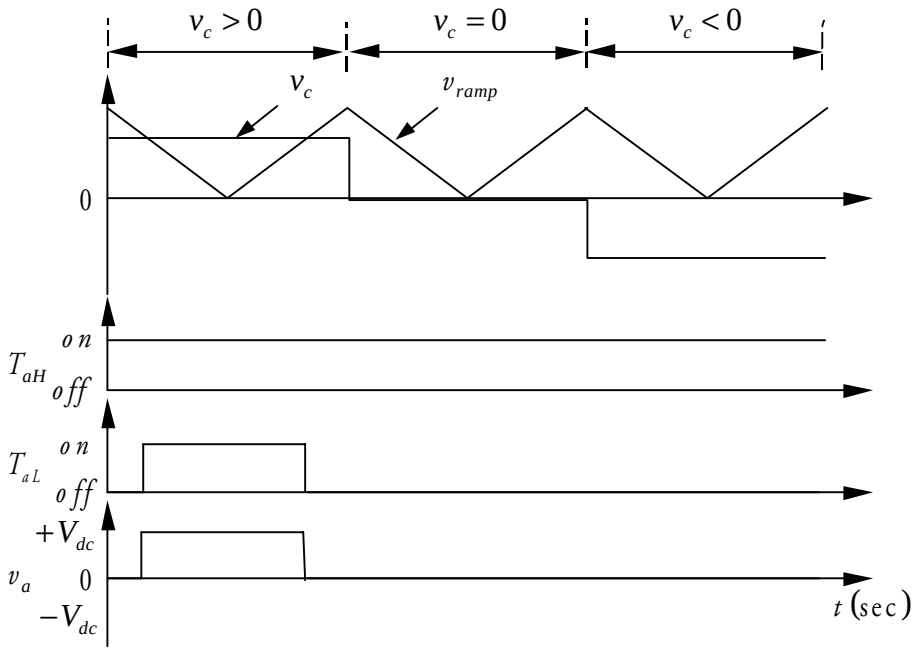

(a) Operational principle

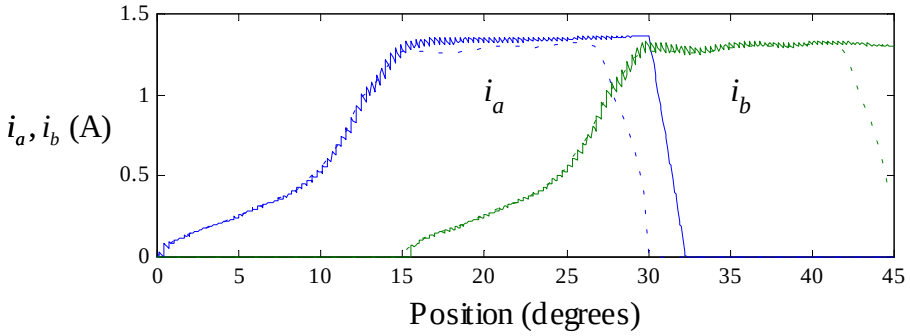

(b) Simulation results

Fig. 6.5 Modified switching strategy

The second switching strategy suggested in [6] is one that allows simultaneous switching of the switches only during the commutation of phases and introduces zero voltage loops. Zero voltage is applied by keeping one switch on but the other turned off, say in this case, with T_{aL} on and T_{aH} being off. This condition allows the phase current to circulate through the winding, switch T_{aL} and diode D_{aL} with zero voltage across the winding, neglecting the diode and switch voltage drops. Therefore, this strategy uses only the first and the third modes. This would allow smaller current ripple than the bipolar switching strategy but it also has a major drawback in that

$-V_{dc}$ cannot be applied except during the commutation period. Therefore, it does not decrease the current rapidly as shown in Fig. 6.5(b). The algorithm for the modified switching and the average output voltage $[v_a]$ are as follows.

$$v_a = \begin{cases} V_{dc} & \text{for } v_c \geq v_{ramp} \\ 0 & \text{for } v_c < v_{ramp} \end{cases} \tag{6.3}$$

$$[v_a] = \frac{V_{dc}}{V_{ramp}} v_c \text{ for } 0 \leq v_c \leq V_{ramp}$$
$$0 \leq [v_a] \leq V_{dc} \tag{6.4}$$

A modification to the first and the second strategy can give both zero and negative voltage across the machine winding. This is identified hereafter as unipolar switching strategy and as such is utilized in other drive systems [24]. The idea of the unipolar switching was first applied to a full-bridge converter consisting of four switches and four diodes. The full bridge converter can handle four-quadrant operation but in this application only two-quadrant operation is necessary. Therefore, with the asymmetric half-bridge converter shown in Fig. 6.1(b) the same performance can be achieved with the proposed switching strategy. All possible modes are exploited in this strategy to incorporate the advantages of both the strategies described before. Simulation results and experimental results are shown in Fig. 6.6(b) and Fig. 6.6(c), respectively. Due to the effectively doubled switching frequency, the ripple contents of the phase currents in the unipolar switching are half of the ripple contents of the phase currents in the modified switching. In addition, fast response can be observed when the phase current is decreasing. The algorithm for unipolar switching and the average output voltage $[v_a]$ are as follows.

$$v_a = \begin{cases} V_{dc} & \text{for } v_c \geq v_{ramp} \ \& \ -v_c < v_{ramp} \\ -V_{dc} & \text{for } v_c < v_{ramp} \ \& \ -v_c \geq v_{ramp} \ \& \ i_a > 0 \\ 0 & \text{elsewhere} \end{cases} \tag{6.5}$$

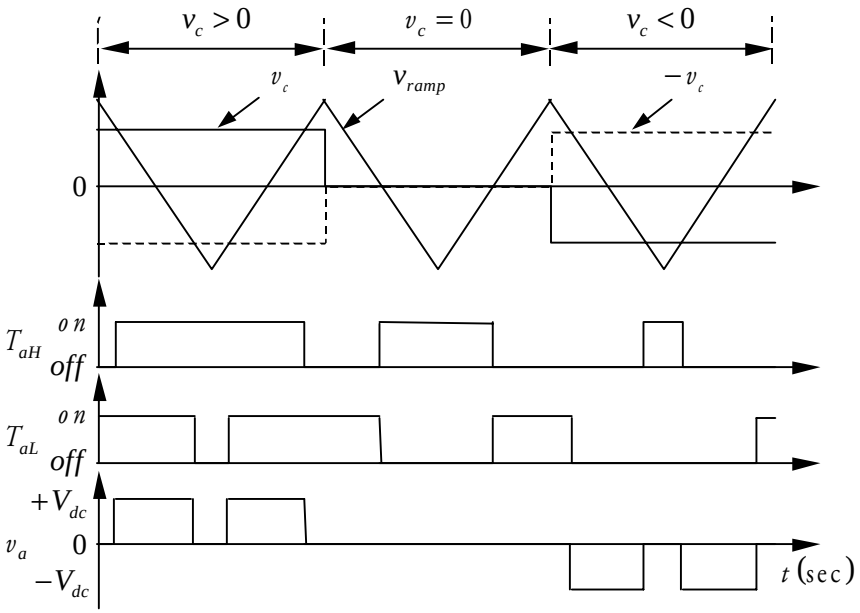

(a) Operational principle

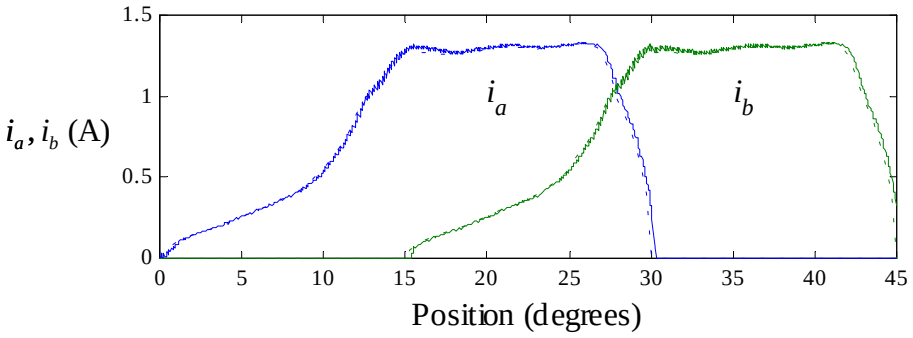

(b) Simulation results

(Vertical div.=0.5 A, horizontal div.=1 ms)

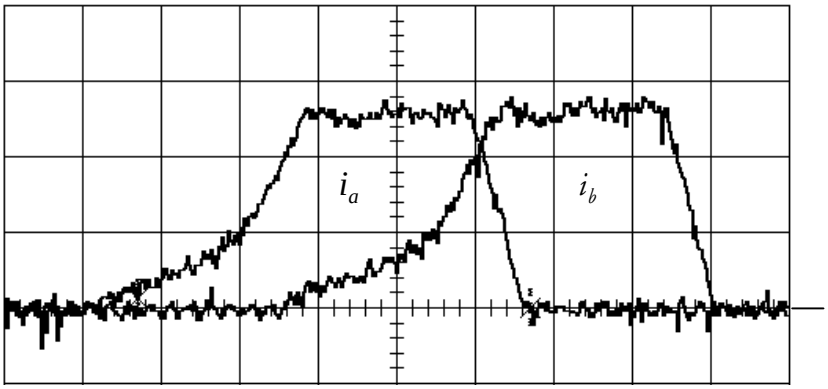

(c) Experimental results

Fig 6.6 Unipolar switching strategy

$$[v_a] = \frac{V_{dc}}{V_{ramp}} v_c \text{ for } -V_{ramp} \le v_c \le V_{ramp}$$
$$-V_{dc} \le [v_a] \le V_{dc} \tag{6.6}$$

Each switching strategy has its own merits and demerits. For instance, the switching loss of the modified switching strategy is relatively small compared with the switching losses of the other two strategies because only one switch is switching while the other switch is continuously turned on. When the switching loss of a switch is larger than the conduction loss of a switch, the total loss of the modified strategy is smaller than the total losses of the other two strategies or vice versa. The control algorithm and its realization for the bipolar switching strategy are relatively simple when two-quadrant operational converter is necessary.

The unipolar switching strategy effectively doubles the switching frequency without increasing the actual switching frequency of the switches. This contributes to the mitigation of current ripple and hence to the reduction of the torque ripple. If current ripple is halved the torque ripple caused by this current ripple is reduced to one fourth of the original one because the generated torque is proportional to the square of current. Moreover since the dynamics of mechanical system can be viewed as a low pass filter the dominant frequency of the torque ripple is also important in that speed ripple is further deduced due to roll off over the cutoff frequency of the mechanical system. Due to these advantages, this switching strategy is applied in this dissertation to achieve high performance in current control and thus, torque control of the SRM.

CHAPTER 7: SIMULATION AND EXPERIMENTAL RESULTS

To verify the proposed torque control algorithms and the unipolar switching strategy applied to the asymmetric half-bride converter, dynamic simulations using MATLAB® software package and experiments using a TI TMS 320F240 DSP-based control system have been performed. The proposed torque control algorithm has also been applied to a linear SRM described in Appendix A. Torque in the prototype SRM corresponds to force in the linear SRM and the linear SRM is differently configured. Therefore, appropriate modifications described in Appendix A are necessary. Simulation results for the linear SRM with the theory of operation are also given in Appendix A and experimental results are given in this chapter.

Operations at representative conditions are simulated and discussion of the results follows. Experimental results of the torque control algorithm based on phase currents are given. Note that such a treatment is consistent with industrial practice.

7.1 Simulations

As a way of verifying the proposed torque control algorithms and the unipolar switching strategy applied to the asymmetric half-bride converter, a series of dynamic simulations have been performed using MATLAB® software package. The dynamic model for the SRM used in the simulation is the model derived in Chapter 5. This general model has been applied to explain the behavior of the SRM in entire region. Operations in six different conditions at two representative output torque commands at three different speeds have been simulated to examine the characteristics of the proposed controllers in various conditions. Two different torque control schemes, which are based on phase currents and flux linkages, have been evaluated with the same conditions. To simulate possible implementation, the sampling time of control loop was set to 50 μs assuming the switching frequency is 20 kHz and the supply voltage is DC 220 V.

Shown in Figs. 7.1, 7.2, and 7.3 are the resultant output torque and phase currents in the six different conditions when the phase currents are the controlled states. Figs. 7.4, 7.5, and 7.6 illustrate the resultant output torque and flux linkages in the same conditions. In Table 7.1, torque error by both controls at various speed and torque levels are summarized. Peak-to-peak torque error after reaching steady state is defined as torque error in Table 7.1. At low speed, both controllers show good performance because the current and flux linkage controller can track commands with negligible error due to smooth waveforms of the commands. For example, at 100 rpm, the torque errors are only 1.3% - 1.6% in entire operating region. At 1000 rpm, however, the torque errors increase up to 8.9% - 17.7%. This originates from the fact that at higher speed the current or flux linkage control loop bandwidth is not high enough to track the steep current or flux linkage command. The fundamental frequency of the current or flux linkage command is low compared with the current or flux linkage control loop bandwidth but the frequencies of the higher order harmonics are approaching the bandwidth of the current or flux linkage control loop. For example, at ω=1000 rpm the fundamental frequency of the phase current or flux linkage command, f_f is,

$$f_f = 1000 \frac{\text{rev}}{\text{min}} \cdot \frac{1}{60} \frac{\text{min}}{\text{sec}} \cdot 6 \text{ phases} = 60 \text{ Hz} \tag{7.1}$$

However, the highest order of meaningful harmonics of the command is much higher than the fundamental. This can be verified by examining Fourier series expansion of the phase current or flux linkage command. Figs. 7.7 and 7.8 show the magnitude of the Fourier series coefficients. At lower current, the torque control based on phase currents shows better performance at all speeds than the torque control based on phase flux linkages due to the smaller total harmonic distortion. However, at higher current, the latter shows better performance due to the abrupt changes in the two adjacent current commands around their intersection. At higher current and speed, both di/dt and $d\lambda/dt$ become too steep to track the commands. As a result, the torque errors become substantial. This shows that in this application some tracking error is inevitable because of the limited bandwidth of the control loops. To further reduce the torque ripple, this practical limitation should be considered in designing the SRM because overall system performance is determined by the characteristics of the machine as well as the controller.

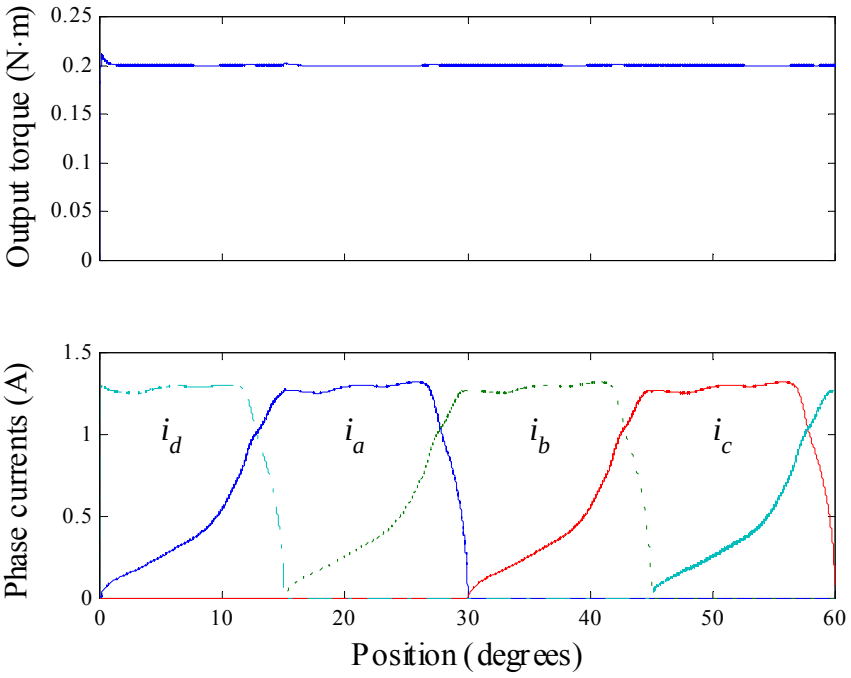

(a) T_e^*=0.2 N·m

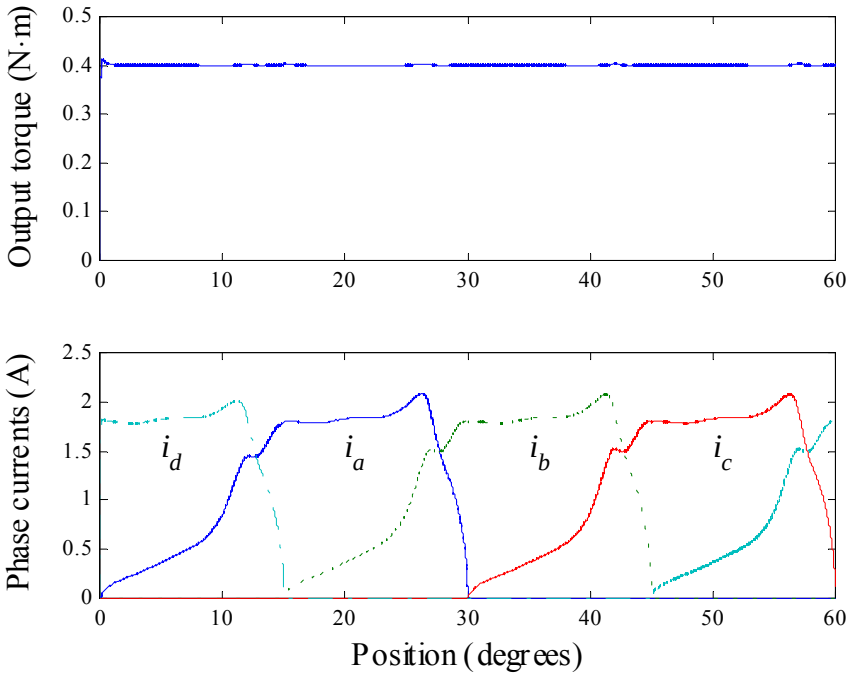

(b) T_e^*=0.4 N·m

Fig. 7.1 Torque control based on phase currents at ω^*=100 rpm

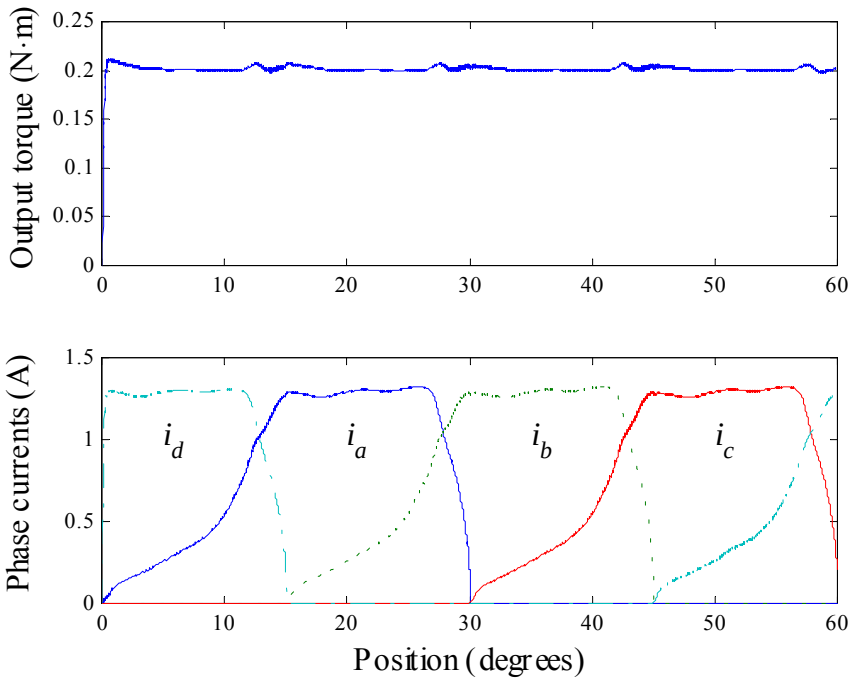

(a) T_e^*=0.2 N·m

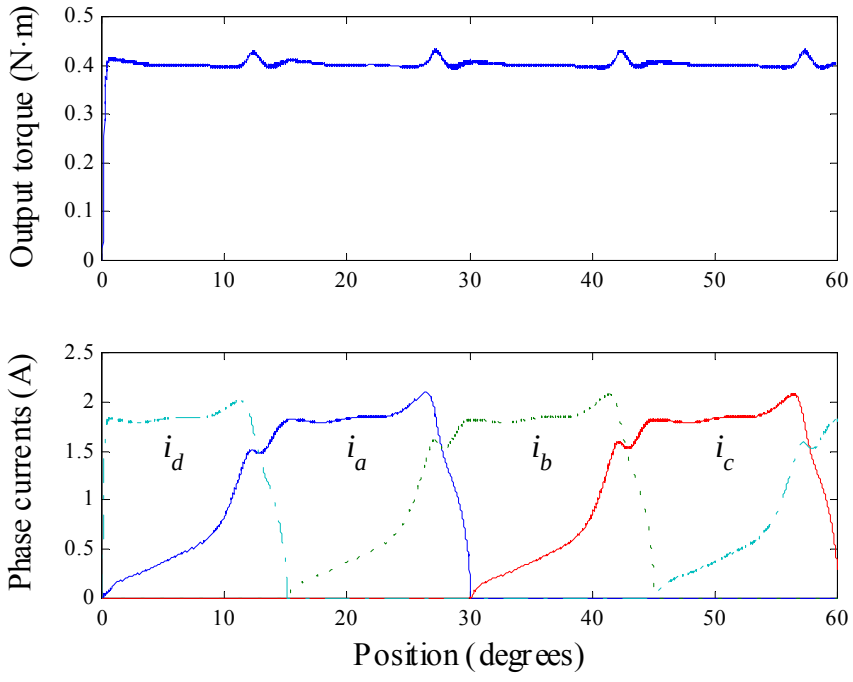

(b) T_e^*=0.4 N·m

Fig. 7.2 Torque control based on phase currents at ω^*=500 rpm

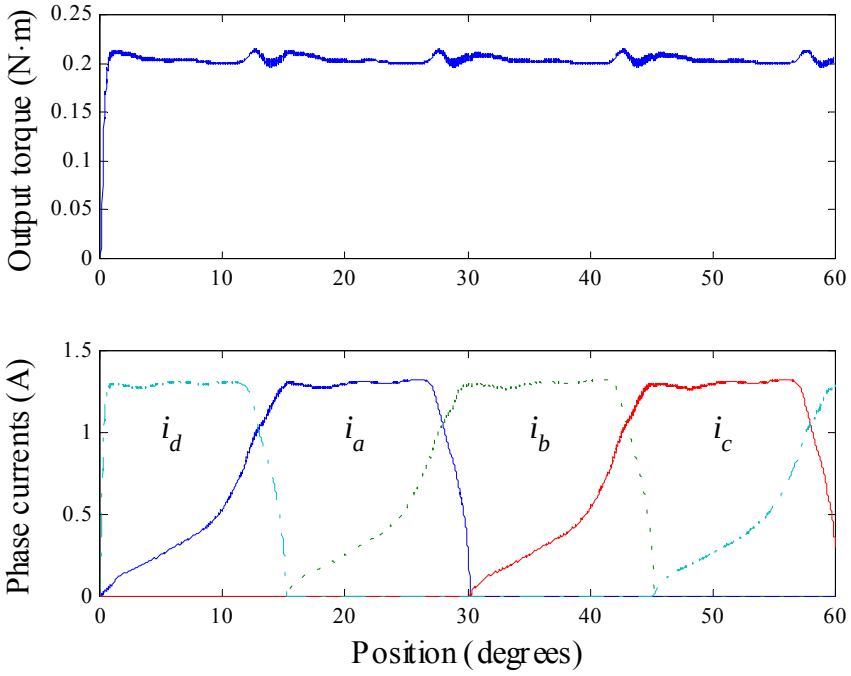

(a) T_e^*=0.2 N·m

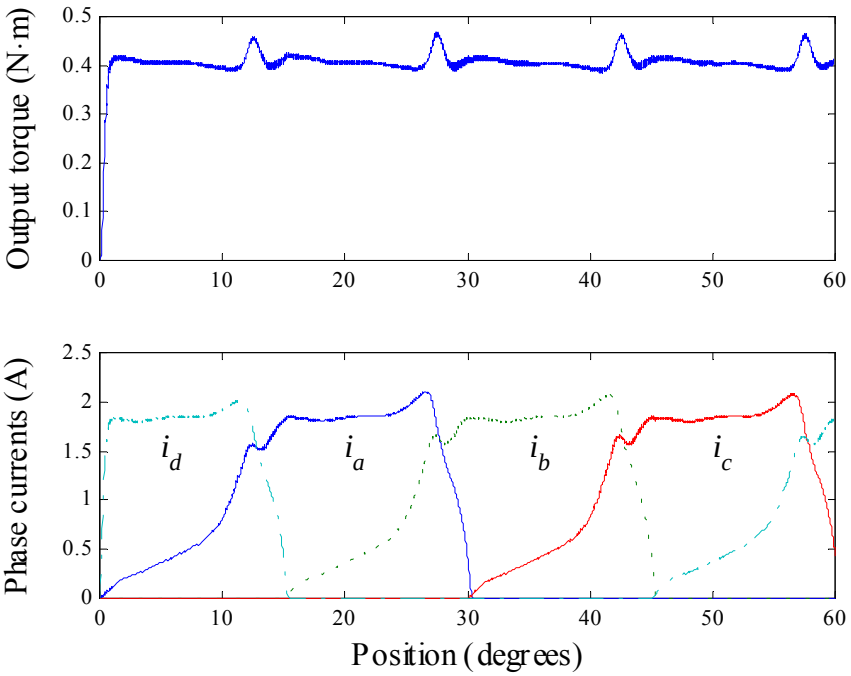

(b) T_e^*=0.4 N·m

Fig. 7.3 Torque control based on phase currents at ω^*=1000 rpm

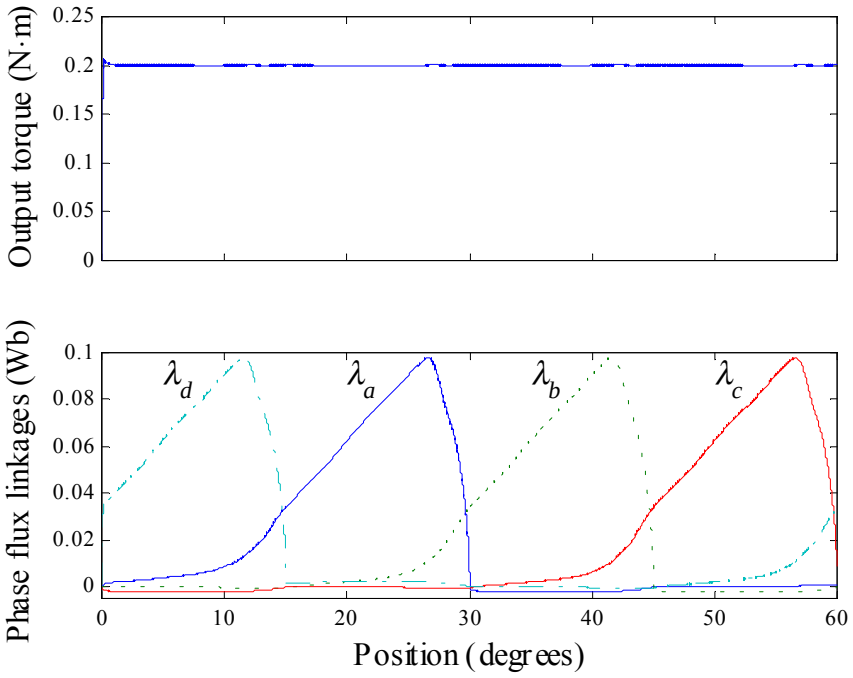

(a) T_e^*=0.2 N·m

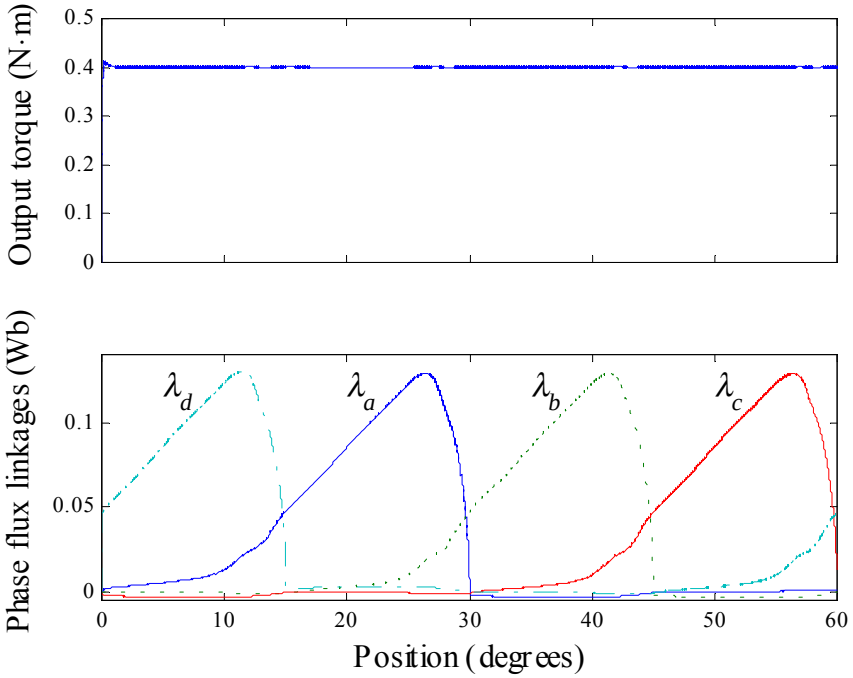

(b) T_e^*=0.4 N·m

Fig. 7.4 Torque control based on phase flux linkages at ω^*=100 rpm

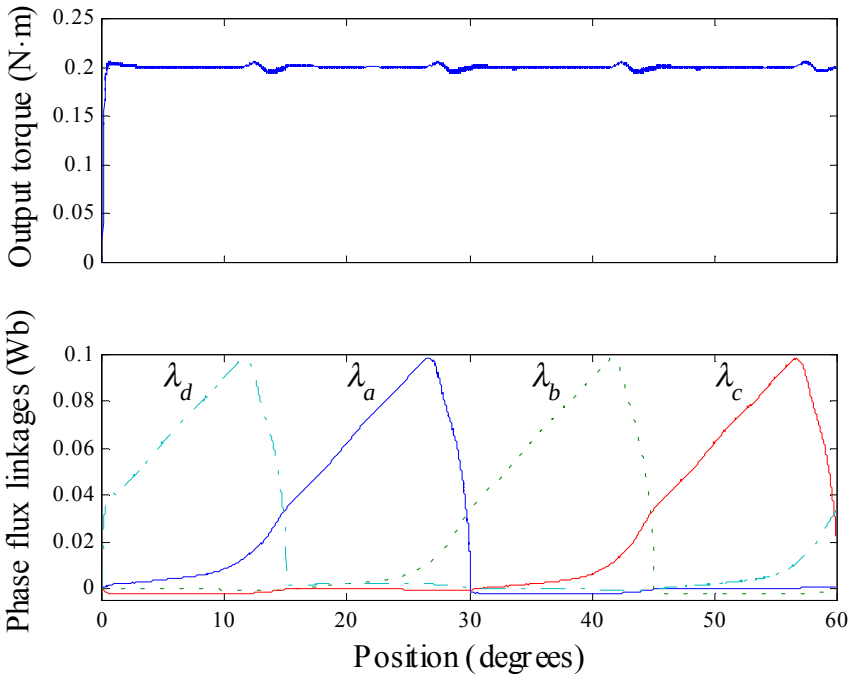

(a) T_e^*=0.2 N·m

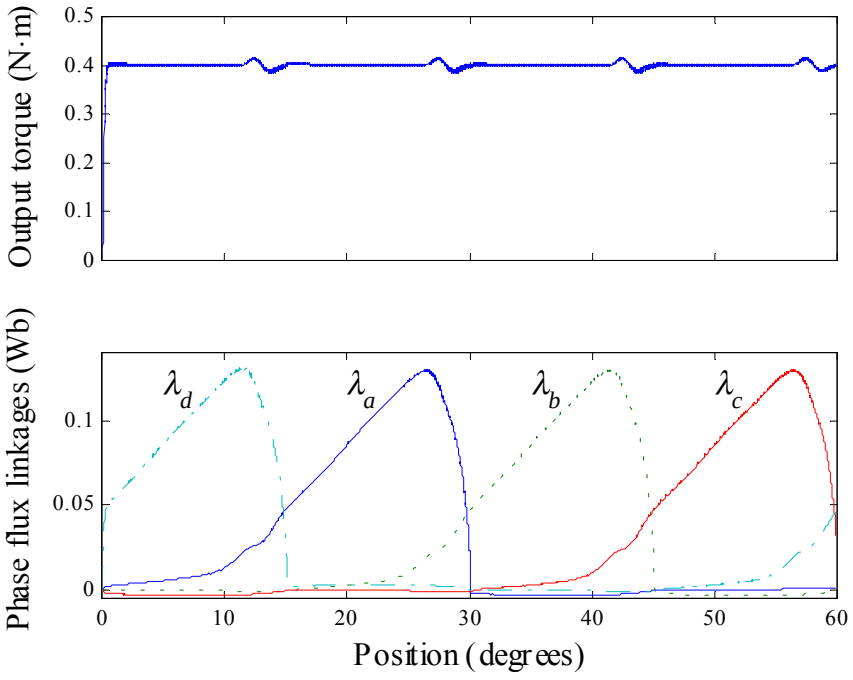

(b) T_e^*=0.4 N·m

Fig. 7.5 Torque control based on phase flux linkages at ω^*=500 rpm

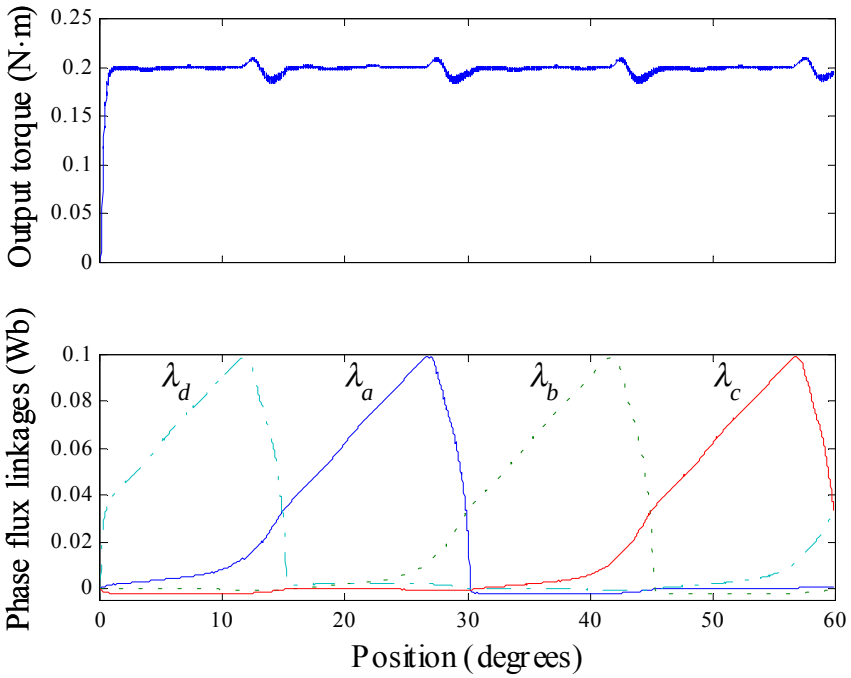

(a) T_e^*=0.2 N·m

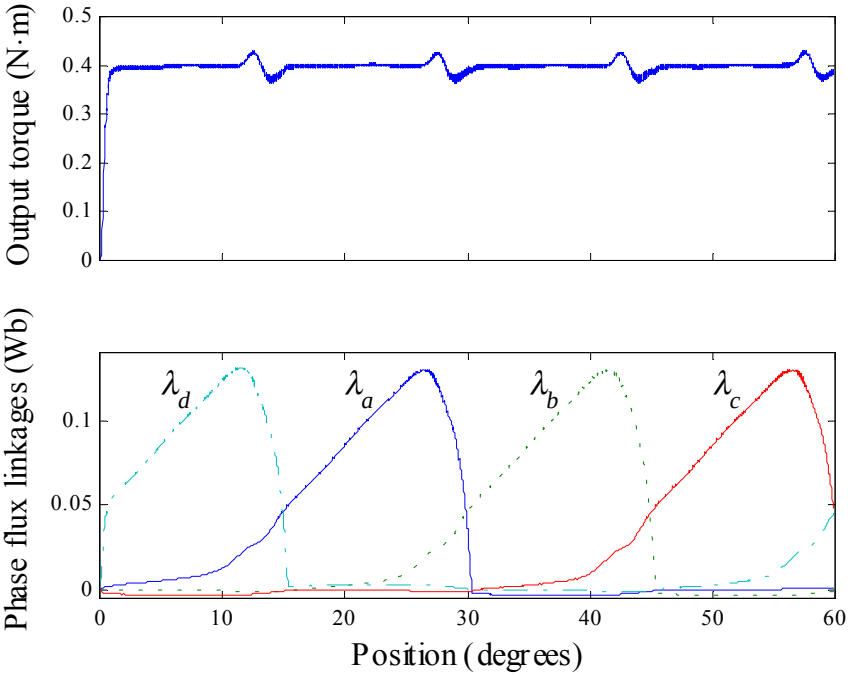

(b) T_e^*=0.4 N·m

Fig. 7.6 Torque control based on phase flux linkages at ω^*=1000 rpm

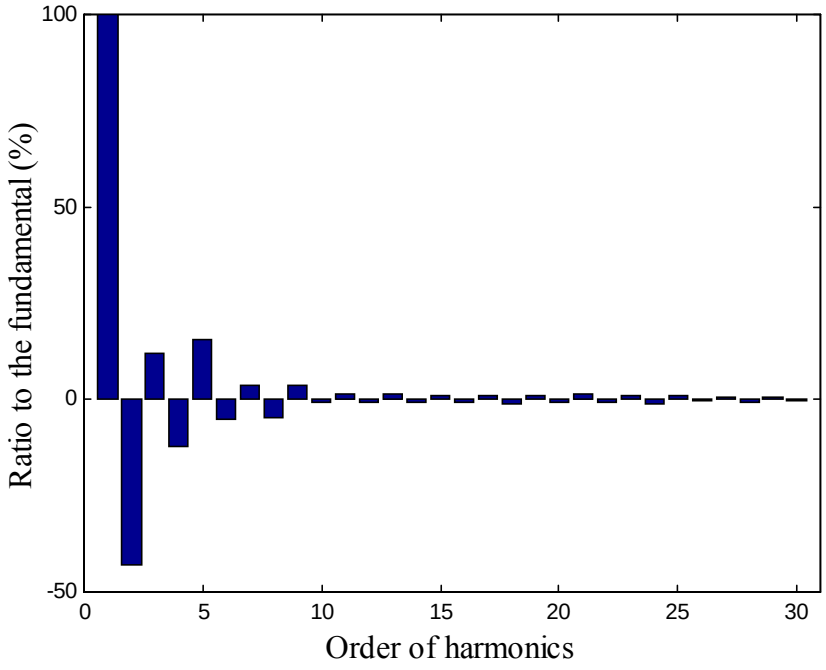

(a) T_e^*=0.2 N·m

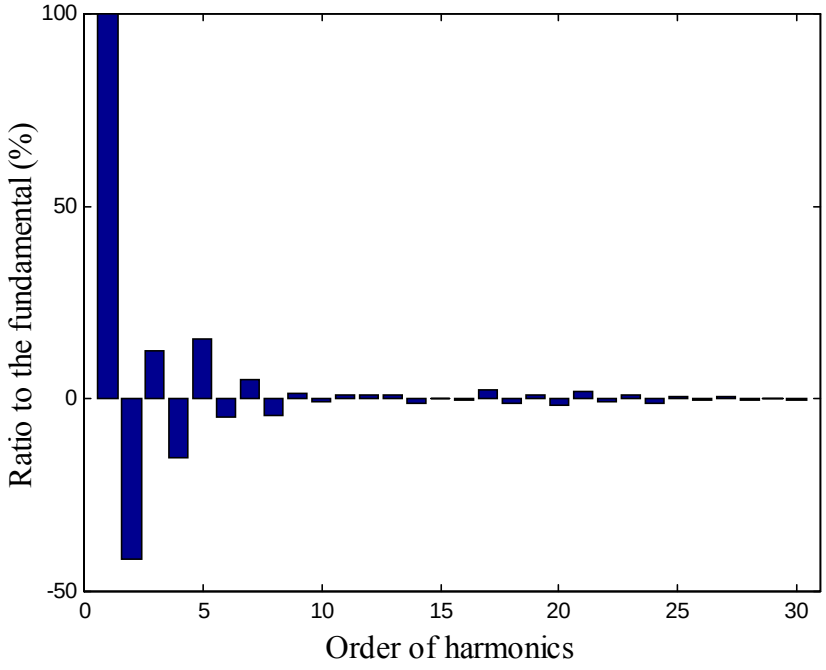

(b) T_e^*=0.4 N·m

Fig. 7.7 Coefficient values of the harmonics of a phase current command

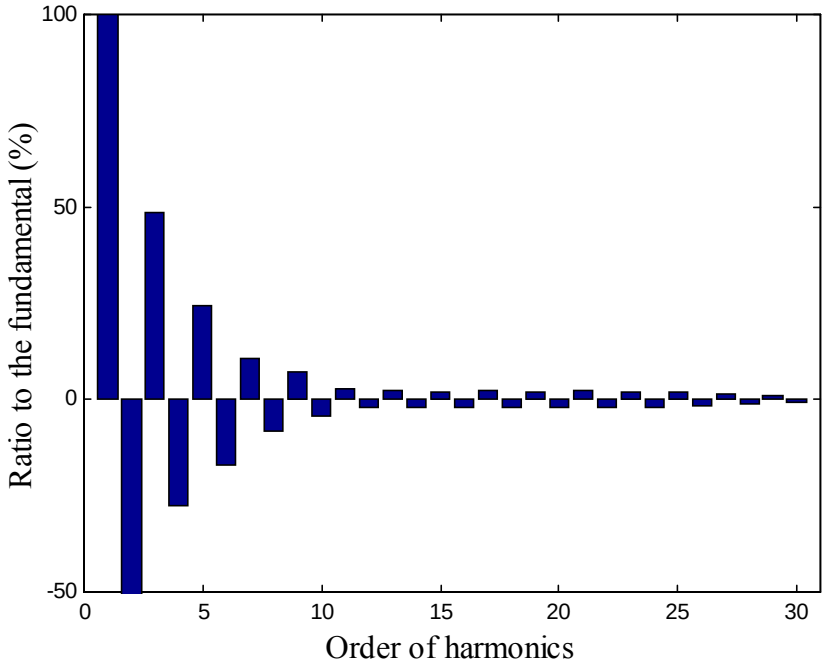

(a) T_e^*=0.2 N·m

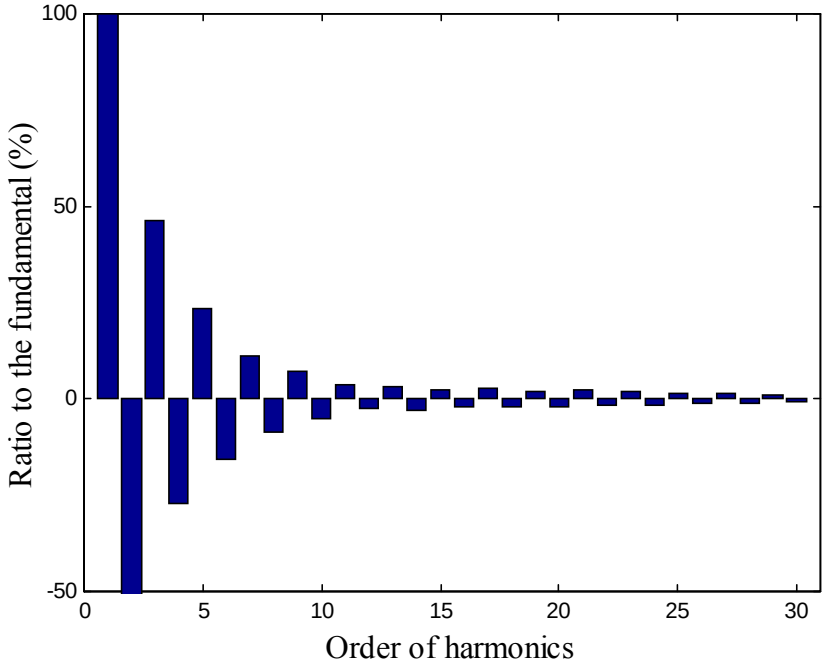

(b) T_e^*=0.4 N·m

Fig. 7.8 Coefficient values of the harmonics of a phase flux linkage command

TABLE 7.1 Torque errors by both controls at various speed and torque levels

Speed [rpm]	Torque error by the torque control based on phase currents [%]		Torque error by the torque control based on phase flux linkages [%]	
	T_e^* =0.2 N·m	T_e^* =0.4 N·m	T_e^* =0.2 N·m	T_e^* =0.4 N·m
100	1.3	1.6	1.4	1.5
500	4.7	8.7	6.1	7.9
1000	8.9	17.7	13.0	16.0

In a position control system, the torque ripple at very low speed is one of the most important factors to characterize the system and small ripple at high speed is usually acceptable. In addition, in a velocity control system, torque ripple at high speed is easily filtered by the inertia of the mechanical system.

7.2 Experimental Results for the Prototype SRM

The torque control based on phase currents, a more common practice in industry, has been implemented on a DSP-based control system. The control board based on the Texas Instrument TMS320F240, a fixed-point processor running at 20 MHz, has been used to perform all control tasks including the unipolar PWM. Because TMS320F240 does not have enough memory space for larger tables and it does not have powerful computation capability such as floating-point calculations, operation is limited within the linear region. However, the dynamic simulations performed in the previous section already verified the feasibility of the proposed controllers in the entire operating range so that it is not necessary to present experimental results in the entire operating range for the verification of the proposed controllers. The dynamic performance has been evaluated through the output torque estimation and velocity measurement because the available instrumentation does not allow a measurement of the dynamic electromagnetic torque.

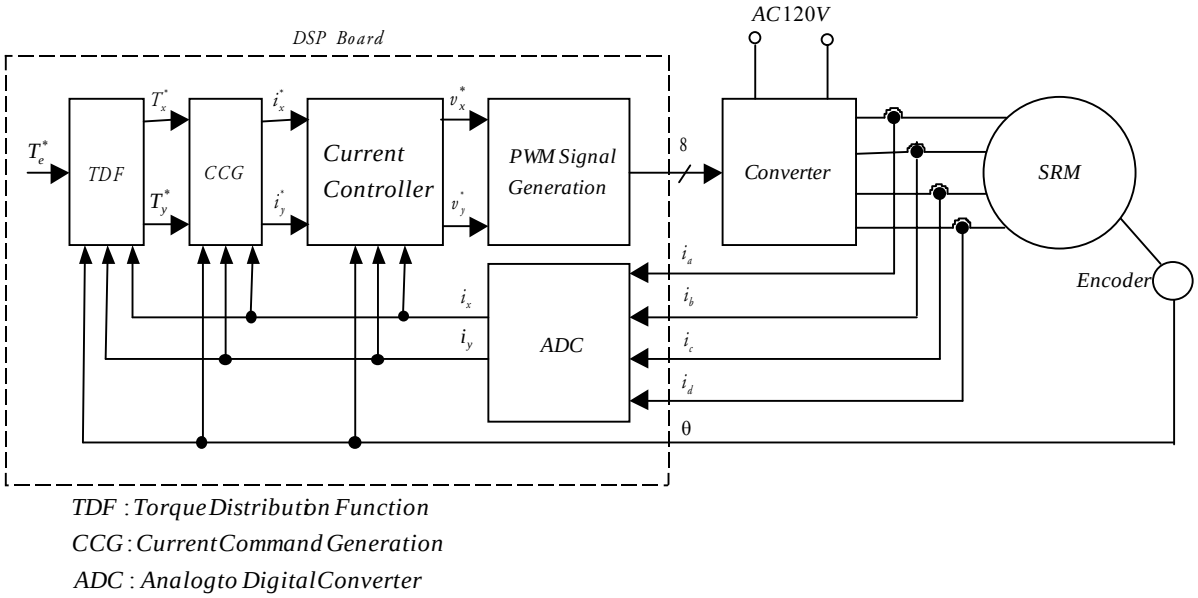

Fig. 7.9 Implementation of the torque control loop using a DSP board

The overall system is composed of a DSP board and an asymmetric half-bridge converter for four phases as shown in Fig. 7.9. All control tasks such as calculation of TDF, generation of phase current commands and implementation of the proposed current controller and the unipolar switching strategy are performed by the DSP board. Each phase current is sensed by a current sensor and sent to the DSP board. Among the four phase currents, only two active phase currents are digitally converted through ADC according to rotor position and the sign of torque command. Similarly, only four PWM signals related to the two active phases are activated whereas other four PWM signals are disabled. Detailed hardware implementation is shown in Fig. 7.10. The DSP board sends PWM signals to the converter and receives phase current feedback and alarm signals from the converter. An optical incremental encoder is attached to the shaft of the SRM to obtain position and velocity feedback. The resolution of the encoder is 2000 pulse/rev. The phase currents are sampled at every 100 μs, and the control loop and PWM signals are also updated at 100 μs to have 1 kHz of the current control loop bandwidth and 10 kHz of switching frequency. To run the SRM at a constant velocity, the outer velocity control loop has been implemented in addition to the torque control loop. The converter is composed of a rectifying circuit, a shunt regulator, four current sensing circuits, and an asymmetric half-bridge converter for four phases. To apply constant external load, a dynamic brake is directly attached to the shaft of the SRM through a mechanical coupling.

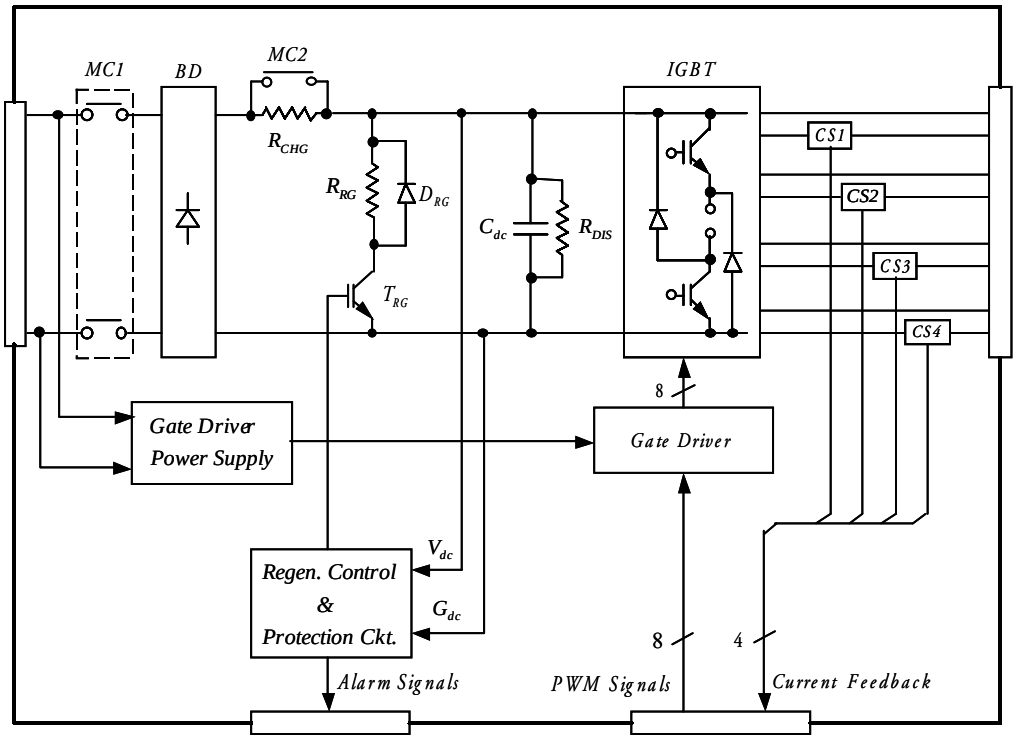

(a) Converter

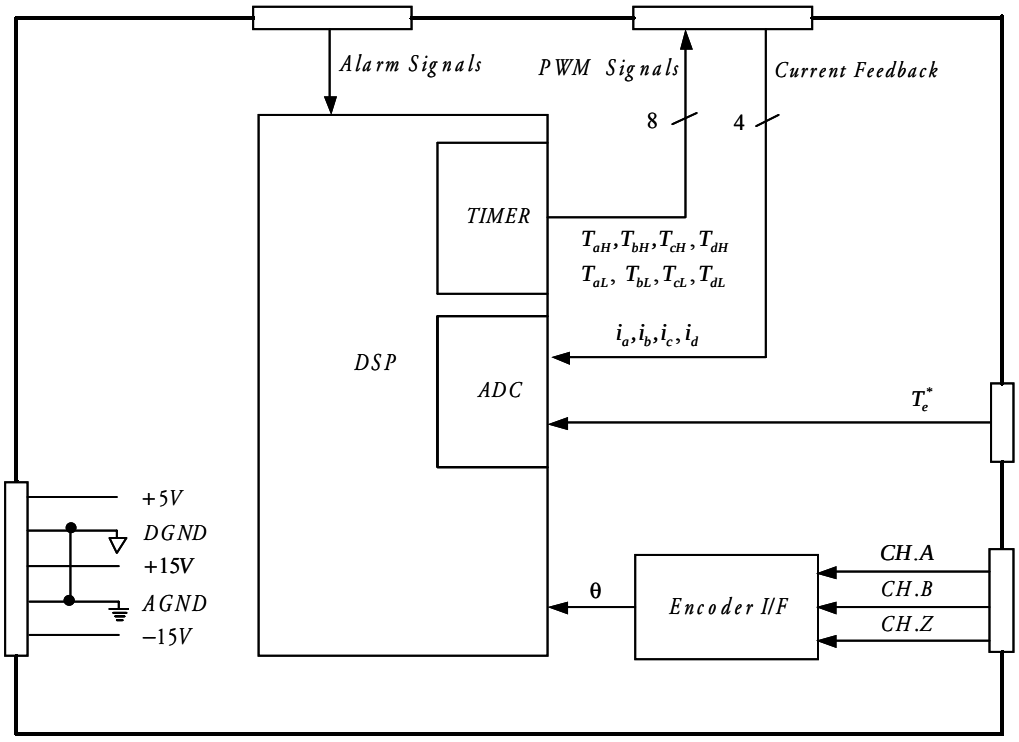

(b) DSP board

Fig. 7.10 Block diagram of the hardware implementation

TABLE 7.2 Comparison torque errors of simulation and experimental results

Speed [rpm]	Torque errors [%]	
	Simulation	Experiment
100	1.3	4.2
500	4.7	9.5
1000	8.9	17.6

In Figs. 7.11, 7.12, and 7.13, the phase current command, feedback, and estimated output torque $\hat{T}_e$ at three different speeds are shown. The commanded output torque is 0.2 N·m to guarantee a linear magnetic circuit. In each figure, the first plot shows the response of the current control loop and the second plot shows the output torque and phase *a* current. The output torque is estimated from the phase currents and the torque functions stored in memory using the relationship given in (2.18). As expected from the simulation results, increased tracking error can be observed at higher speed. The torque errors at three different speeds are listed with the corresponding simulation results in Table 7.2. Due to lower bandwidth of the current control loop, the experimental results show increased torque errors when compared with the simulation results. In addition, due to the cogging torque and the huge inertia of the brake, the performance of the velocity control loop is degraded. Therefore, the waveform of the current command is slightly distorted at high speed. These experimental results strongly match the simulation results except that some measurement noise is added to the real signal and some degradation is found as mentioned earlier.

Alternate test of the system in the form of the step response of the velocity control loop is shown along with the phase current in Fig. 7.14. Again, the maximum output torque is limited to 0.2 N·m to ensure that the SRM is operated in linear range. For this experiment, the dynamic brake is disconnected from the motor shaft to provide unloaded condition. Reasonable rise time and damping can be observed in this figure. When the velocity command changes from –1000 rpm to 1000 rpm, the SRM starts to operate in regeneration mode until the velocity of the SRM reaches zero. Then, the SRM is running in motoring mode. The phase current clearly shows the behavior of torque controller during torque reversal.

Vertical div.=0.5 A, horizontal div.=20 ms

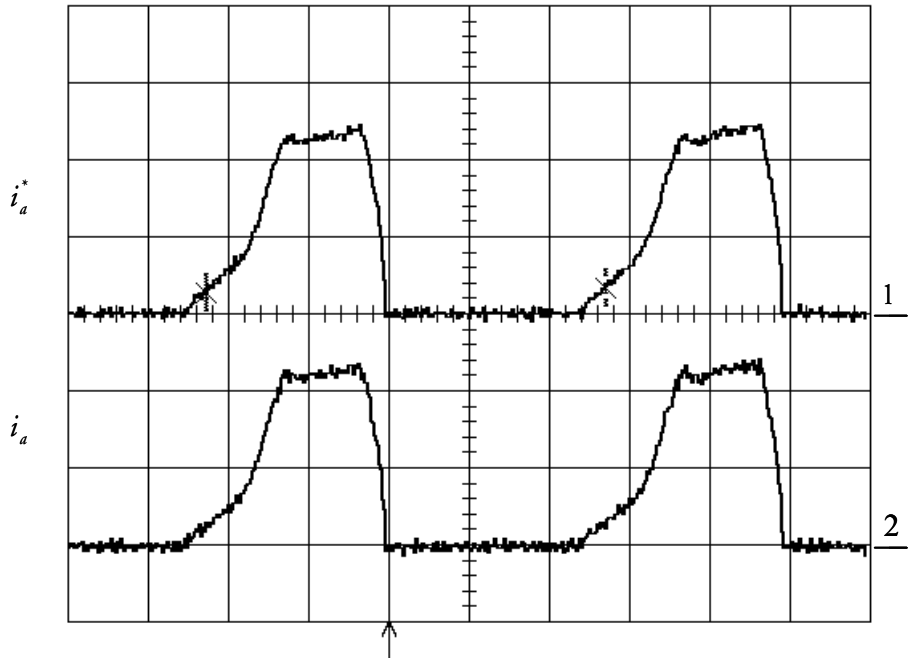

(a) i_a^* and i_a

Vertical div.1=0.1 Nm, vertical div.2=0.5 A, horizontal div.=20 ms

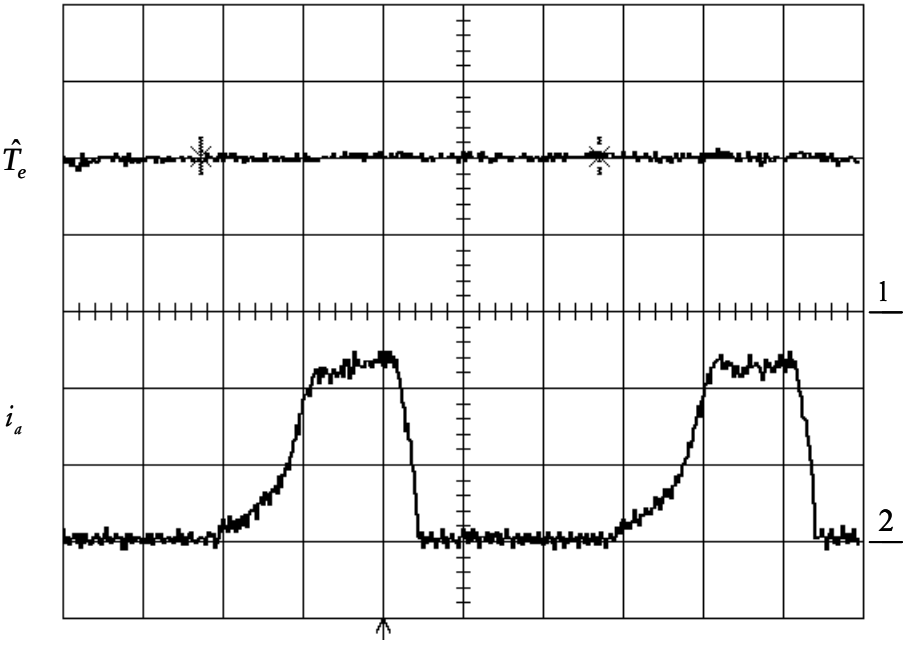

(b) $\hat{T}_e$ and i_a

Fig. 7.11 Response of the current control loop and the estimated output torque at ω^*=100 rpm and T_e^*=0.2 N·m

Vertical div.=0.5 A, horizontal div.=5 ms

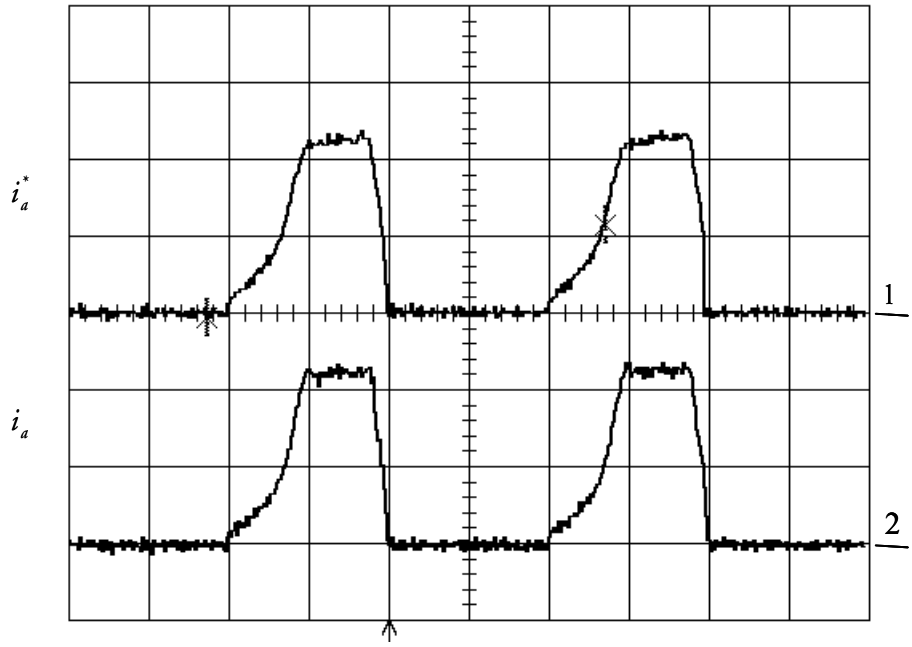

(a) i_a^* and i_a

Vertical div.1=0.1 Nm, vertical div.2=0.5 A, horizontal div.=5 ms

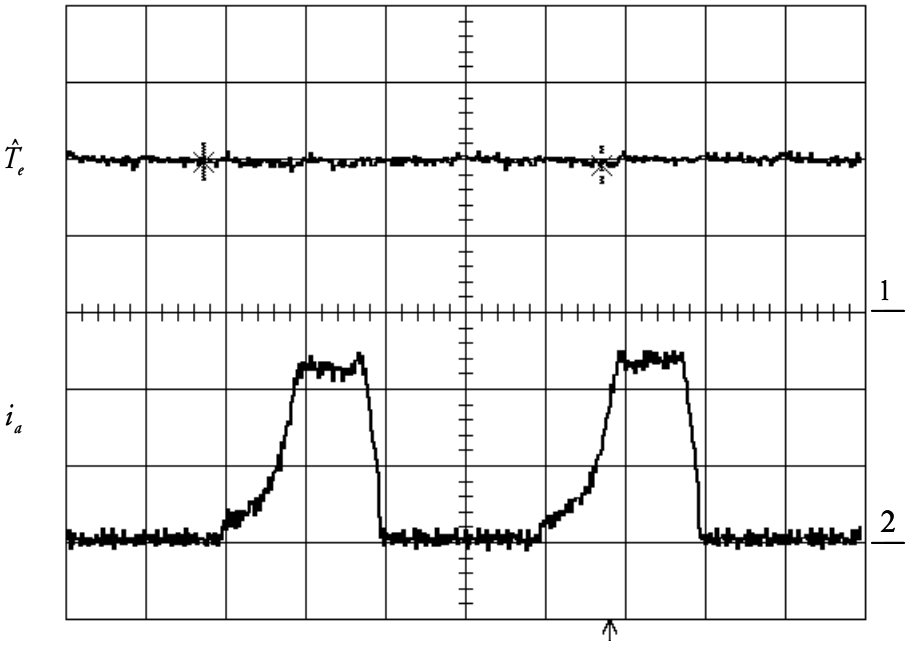

(b) $\hat{T}_e$ and i_a

Fig. 7.12 Response of the current control loop and the estimated output torque at ω^*=500 rpm and T_e^*=0.2 N·m

Vertical div.=0.5 A, horizontal div.=5 ms

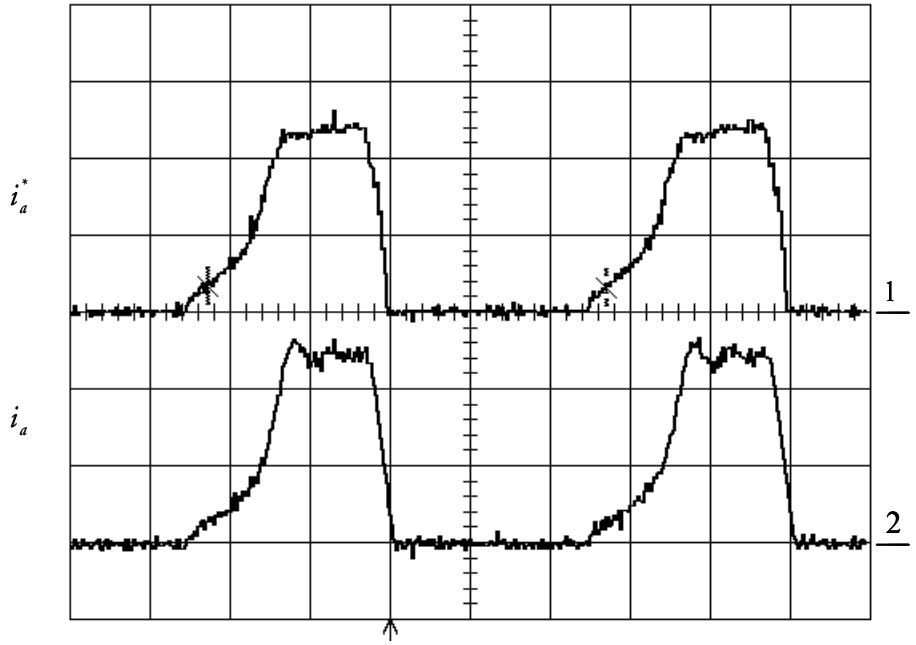

(a) i_a^* and i_a

Vertical div.1=0.1 Nm, vertical div.2=0.5 A, horizontal div.=2 ms

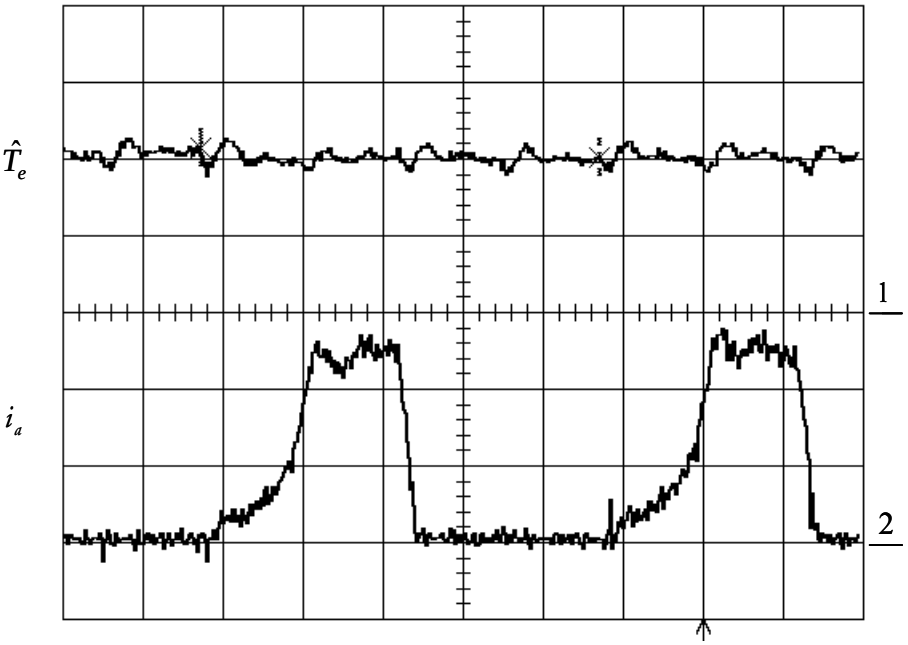

(b) $\hat{T}_e$ and i_a

Fig. 7.13 Response of the current control loop and the estimated output torque at ω^*=1000 rpm and T_e^*=0.2 N·m

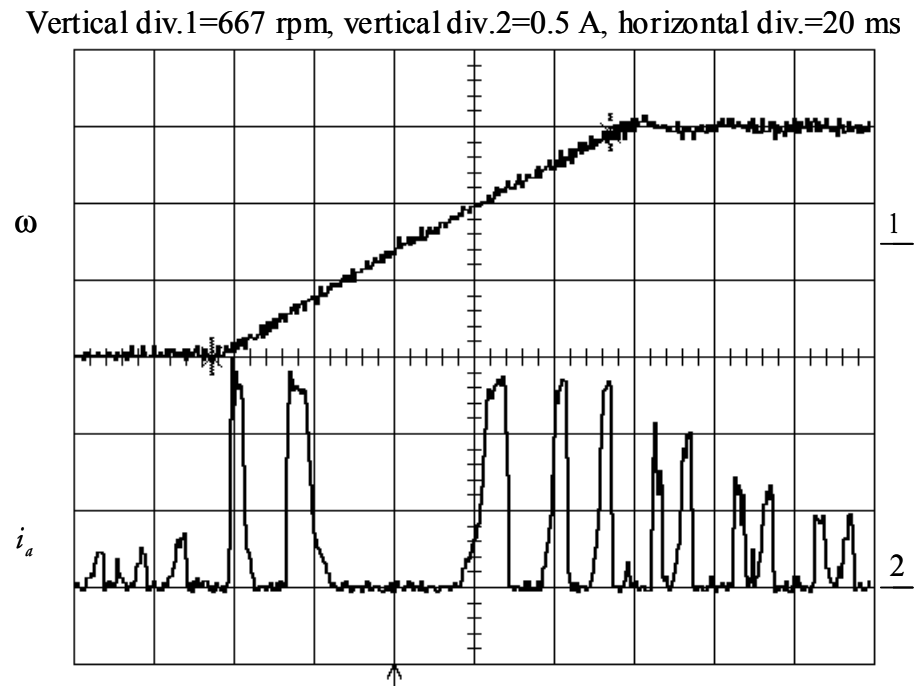

Fig. 7.14 Step response of the velocity control loop when ω^*=-1000 rpm to ω^*=1000 rpm

7.3 Experimental Results of the Linear SRM

For the verification of the application of the proposed torque control algorithm to the linear SRM described in Appendix A, experimental results are shown in this section. The theory of operation, simulation results, and the experimental set-up are described in Appendix A.

Fig. 7.15 shows the phase current command, feedback, and the estimated output force $\hat{F}_e$ at $\dot{x}^*$=0.2 m/s. The first plot shows the response of the current control loop and the second plot shows the output force and phase *a* current. Unlike the rotary SRM, it is not possible to apply a dynamic load to the LSRM with the available equipment. Hence, only the friction produced by the normal force at this speed is applied as a dynamic load. It is seen that the actual phase current follows the commanded value closely. The output force is estimated from the phase currents and the force functions stored in memory using the relationship given in (A.4). This shows a nearly ripple free force profile.

Vertical div.=1 A, horizontal div.=20 ms

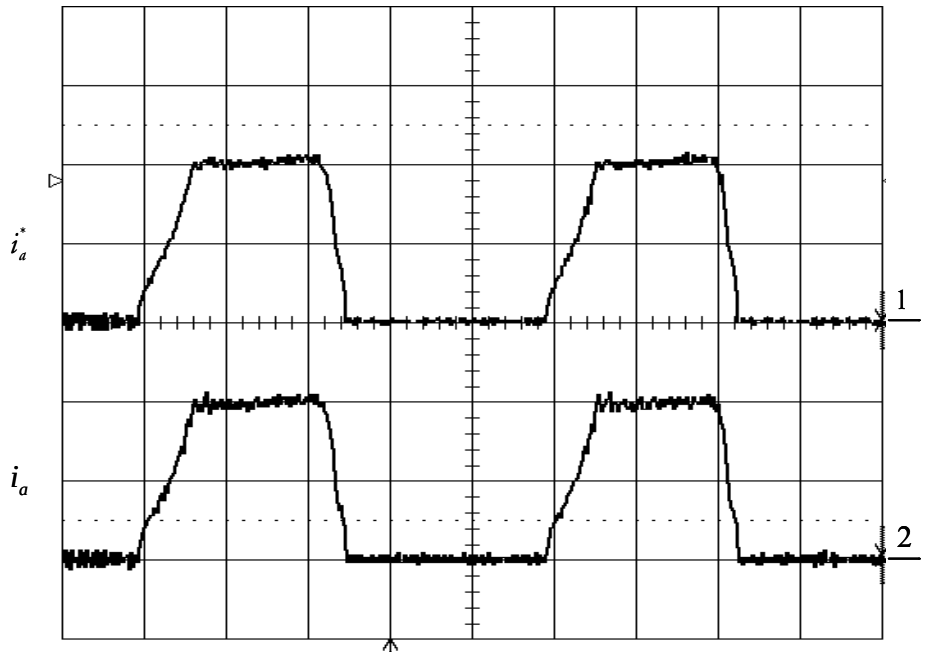

(a) i_a^* and i_a

Vertical div.1=2.5 N, vertical div.2=1 A, horizontal div.=20 ms

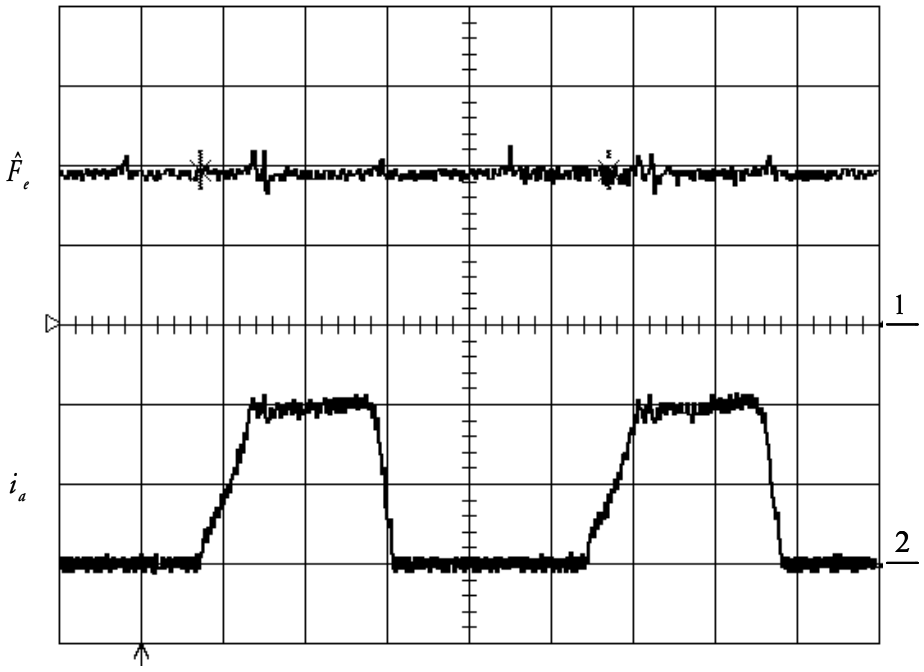

(b) $\hat{F}_e$ and i_a

Fig. 7.15 Response of the current control loop and the estimated output force at $\dot{x}^*$ =0.2 m/s

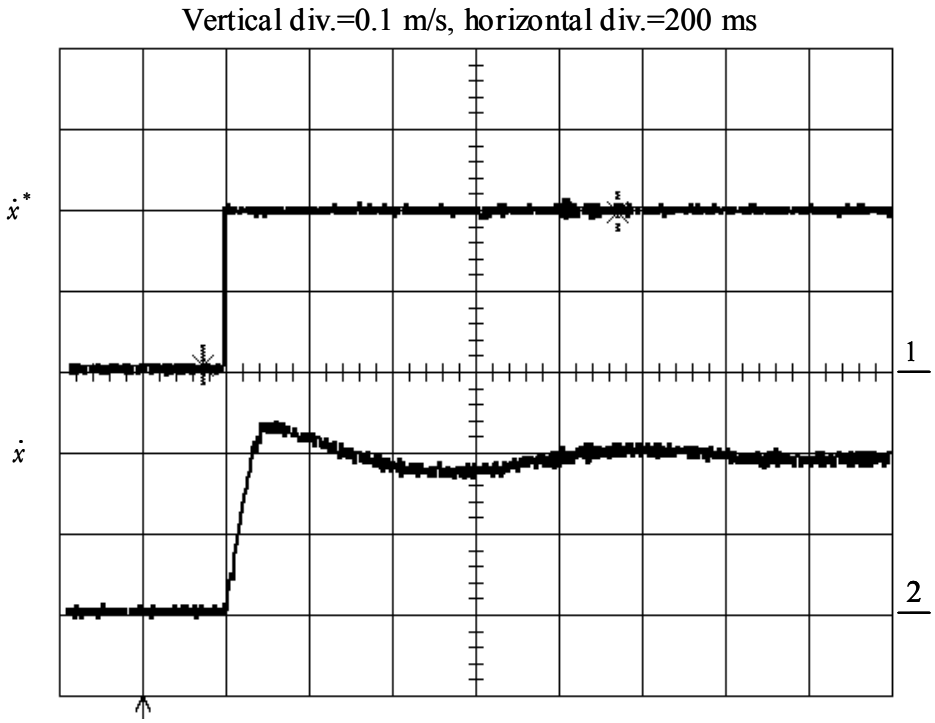

Fig. 7.16 Step response of the velocity control loop when $\dot{x}^*$=0 m/s to $\dot{x}^*$=0.2 m/s

Similarly, the step response of the velocity control loop is shown in Fig. 7.16. Reasonable rise time and damping are observed in this figure.

CHAPTER 8: CONCLUSIONS

This chapter summarizes the key tasks and contributions of this research, which have been accomplished. This dissertation has effectively addressed and solved the problems outlined in the introduction.

1) A thorough literature survey has been performed on the SRM drives. It shows the existence of research material that identifies the prediction of self-inductance by analytical as well as finite element methods and their experimental verification. However, there is very little material that accounts for the mutual inductance between the phases. Frequently, the mutual inductances have been neglected by assuming that their magnitudes are small enough to have no effects on the operation of the machine. However, one of the primary assertions of this dissertation is that in many cases the mutual inductances are not insignificant and can sometimes be as much as 10% of the self inductance. Their effects cannot be ignored in the torque ripple-free operation of the SRM requiring precise control. In this dissertation, the mutual inductances are obtained by finite element analysis and they are verified by measurements. There is a strong correlation between the predicted finite element results and measured values.

2) Conventionally, only one phase has been considered at a time when deriving the voltage and torque equations. However, the effects of mutual coupling cannot be included with these equations. Therefore, two adjacent phases, which are excited intentionally or unintentionally, have been considered simultaneously. The dynamic equations of the SRM for two-phase excitation including the effects of mutual coupling have been newly derived. The effects of the mutual coupling have been represented in terms of mutual inductances in these equations. Two different dynamic equations in terms phase current and flux linkages have been derived. They have been compared to determine the advantages and disadvantages of their use.

3) Only one phase, which has the strongest torque function at a given position, has been utilized in the conventional operation of the SRM. In this dissertation, two phases have been excited

simultaneously to obtain a minimum ripple performance using a new torque control algorithm. Conventionally, the SRM has been operated with step-wise phase currents or flux linkages. With the step-wise currents or flux linkages, the output torque of the SRM, which depends on phase currents and rotor position, shows significant ripple since the torque is developed based on individual phase excitations. As a result, this form of control that produces an average torque output is not acceptable in high performance operation. To achieve a high bandwidth torque control in applications that require good transient performance, it is necessary to employ instantaneous torque control. Moreover, the conventional commutation has to be replaced by a control scheme that profiles the phase currents or flux linkages to produce the desired total output torque by coordinating the output torque produced by individual phases. If the individual phase currents or flux linkages can be controlled with a high bandwidth, then choosing the appropriate current or flux linkage waveforms will guarantee low torque ripple. It has been proved that at any position two adjacent phases contribute to generate desired torque and the excitation interval of a phase can be broadened to 30 degrees whereas it is 15 degrees in conventional drives. Therefore, if precise current or flux linkage control is assumed, torque control implies the distribution of the desired torque to each phase and the generation of phase currents or flux linkages from the distributed torque. Considering several feasible performance indices, a novel Torque Distribution Function (TDF) has been proposed. This reduces the rate of change of phase currents or flux linkages and the peak current or flux linkage magnitude. Initially, the operation of the SRM in the linear magnetic region neglecting the effects of the mutual coupling has been analyzed and simulated. The output torque is found to have approximately 7% peak to peak ripple value. Then, a new TDF that includes the effects of the mutual coupling has been proposed. The simulation results of the proposed TDF in the linear magnetic region have shown that the output torque has no ripple when an ideal current or flux linkage controller is used. A modified TDF for the operation of the SRM including the magnetic saturation has also been proposed. This is necessary as most machines operate in the saturated region at rated condition. Although the waveforms of the phase currents or flux linkages become less smooth, the output torque is still ripple-free. With the proposed TDF, the amount of memory is significantly reduced because only two-dimensional tables are

necessary in entire operating range while the existing torque control algorithms require three-dimensional tables.

4) The two different torque controllers based on the phase currents and flux linkages, showing identical dynamic responses at all positions even with significantly varying inductances and compensating the effect of mutual coupling, have been proposed. They have been extensively simulated and verified by experiments. A feedback linearizing current controller has been proposed to linearize and decouple the current control loop. A gain scheduling scheme, which changes the gain of the current controller based on rotor position and phase currents, has also been introduced. It has been shown that with the conventional current controller, it is not possible to obtain a high-performance current control. By implementing the current controller with the gain scheduling, a good dynamic response at all positions has been achieved. A feedback linearizing flux linkage controller has also been considered by examining the equations in terms of flux linkages. The advantage of this method over the previous method is that the gains of the flux linkage controller are not functions of rotor position and phase currents. Hence, the computation required is much reduced. However, this method requires certain additional computation to estimate the phase flux linkages from the phase currents and related parameters. Therefore, it can be more sensitive to parameter variation. The effects of varying stator resistance have are been considered with the flux linkage control.

5) The significance of separating the operation in the linear and saturated region lies in the fact that in some applications machines are operated only in the linear region. The proposed controller has been used in the operation of a Linear Switched Reluctance Motor (LSRM). The LSRM is strictly operated in the linear portion due the fact extremely high normal forces affect the machine when operated in the saturation region. An implementation of the proposed controller and force distribution function has shown ripple-free force response of the LSRM.

6) From the existing converter topologies, the two most popular converter topologies for an 8/6 SRM have been examined for the prototype SRM. They are the half-bridge converters

capable of providing the three voltage loops and operating in two quadrants. Four possible modes of operation for the converters and the operational limitation of the shared switch asymmetric half-bride converter have been identified. Therefore, the asymmetric half-bridge converter, in which there are operational possibilities even with one or two phase faults, has been chosen. A new switching strategy called the unipolar switching strategy for the selected asymmetric half-bridge converter has been proposed. This strategy effectively doubles the switching frequency without increasing the actual switching frequency of the switches. Therefore, it can reduce the hysteresis losses in the motor and the power dissipation in the DC link capacitor during any period when switches in the converter are controlled to reduce the net applied voltage to the phase winding. This also contributes to the mitigation of phase current or flux linkage ripple and hence to the reduction of the torque ripple. If phase current or flux linkage ripple is halved, the torque ripple caused by this current or flux linkage ripple is reduced to one fourth of the original one because the generated torque is proportional to the square of current or flux linkage. Moreover, since the dynamics of mechanical system can be viewed as a low pass filter, the dominant frequency of the torque ripple is also important in that speed ripple is further reduced due to roll off over the cutoff frequency of the mechanical system. Due to these advantages, this switching strategy has been applied to achieve high performance in current or flux linkage control.

7) The proposed torque control schemes and switching strategy have been extensively simulated and experimentally tested using a Texas Instrument 320F240 DSP based system. It has been shown that the schemes are suitable for low speed as well as for high speed, although the torque ripple gradually increases with speed. The presented torque schemes maximize the torque producing capability of the SRM and they also reduce the peak current requirements for the converter. The experimental results very closely match the simulation results. It is predicted that better performance can be achieved by using a more powerful DSP for the controller.

It is believed that this research is original in the SRM drive field and it can solve several problems mentioned in the introduction and improve the overall system performance. The proposed controller is readily expandable to the SRM with different configuration, PMSM

(Permanent Magnet Synchronous Motor) and BLDCM (Brushless DC Motor). In reference [26], a new power-converter topology was proposed to minimize the cost and to enhance the reliability of the BLDCM drive system. It is believed that with the proposed controller it is possible to add high performance to the BLDCM drive system.

APPENDIX A: APPLICATION OF THE PROPOSED TORQUE CONTROL ALGORITHM TO A LINEAR SWITCHED RELUCTANCE MOTOR

Linear Switched Reluctance Motors (LSRMs) with different machine configurations have been explored before in literature [33]-[41]. They are an attractive alternative to linear induction or synchronous machines due to lack of windings on either the stator or rotor structure. Further, the windings are concentrated rather than distributed making it ideal for easier manufacturing and maintenance. Although, LSRM configurations and finite element results have been described in literature, very little material describes the control of the LSRM. Basic converter configurations have been described in [33], [35], [39] - [41] but the control procedure is not described extensively. However, there is extensive material covering the various converter topologies for a Rotary Switched Reluctance Motor (RSRM) summarized in [6]. There are also various control strategies for the RSRM described in literature.

This chapter intends to describe the control algorithms and the converter topology for the prototype LSRM. A force controller based on the traditional single-phase excitation but with the associated complex control sequence is described. The torque control algorithm (force control algorithm in case of the LSRM) proposed in previous chapters is applied to this LSRM to reduce force ripple as well as the normal force. The unique feature of the LSRM lies in the fact that the operation of the machine is restricted to the linear magnetic region as operation in the saturated region causes high normal forces as described in [30]. Hence the torque control algorithm based on phase currents in the linear magnetic region and the unipolar switching strategy described Chapters 2, 3, 4 and 6 can be applied to the LSRM. In addition, because the mutual inductances of this specific LSRM are relatively small, they are not considered when designing the force controller and the phase current controller. The converter topology is chosen to minimize the number of switches and current sensors. It is a variant of the traditional asymmetric half-bridge converter as well as the shared switch asymmetric half-bridge converter used for RSRM with even number of phases.

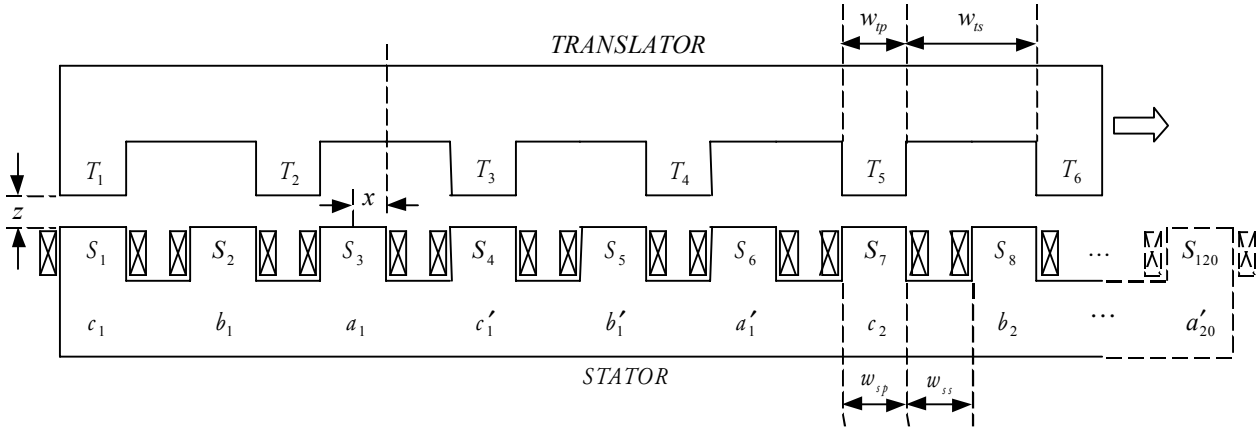

Fig. A.1 LSRM structure and winding diagram

The configuration of the LSRM and its basic operation is described in Section A.1. Section A.2 covers the converter topology and its various modes of operation. Section A.3 describes the two different force control strategies along with simulation results. Section A.4 gives the design of the current controller for the system. Section A.5 contains experimental set-up. Experimental results are included in Chapter 7. Conclusions and contributions of this work are summarised in section A.6.

A.1 LSRM Configuration

Fig. A.1 shows the machine structure and winding diagram of an LSRM. The LSRM has an active stator, a passive translator that is analogous to the rotor in a RSRM and a longitudinal flux configuration. The active stator configuration was chosen not to encounter the power transfer problems associated with the active translator configuration. The LSRM configuration corresponds to a 6/4 RSRM configuration. It consists of 6 translator poles and 120 stator poles spread over 4.8m. One stator sector is composed of 6 stator poles and hence the total number of stator sectors is 20. A RSRM has four rotor poles and hence the corresponding LSRM should have 4 translator poles. But in the LSRM structure with four translator poles, individual coils should be excited for continuous forward and backward motion resulting in doubling the number of switching devices [33]. The translator poles are increased from 4 to 6 to minimize the number of switching devices and simplify the excitation sequences.

Table A.1 Forward motion sequence in the first sector

Position (mm)	Phase	Stator	Translator
0-7.4	C_1	$S_1 - S_4$	$T_1 - T_3$
7.4-27.4	A_1	$S_3 - S_6$	$T_2 - T_4$
27.4-47.4	B_1	$S_2 - S_5$	$T_1 - T_3$
47.4-67.4	C_2	$S_7 - S_{10}$	$T_4 - T_6$
67.4-87.4	A_2	$S_3 - S_6$	$T_1 - T_3$
87.4-107.4	B_2	$S_8 - S_{11}$	$T_4 - T_6$
107.4-127.4	C_2	$S_7 - S_{10}$	$T_3 - T_5$
127.4-147.4	A_2	$S_9 - S_{12}$	$T_4 - T_6$
147.4-167.4	B_2	$S_8 - S_{11}$	$T_3 - T_5$
167.4-187.4	C_2	$S_7 - S_{10}$	$T_2 - T_4$
187.4-207.4	A_2	$S_9 - S_{12}$	$T_3 - T_5$
207.4-227.4	B_2	$S_8 - S_{11}$	$T_2 - T_4$
227.4-240	C_2	$S_7 - S_{10}$	$T_1 - T_3$

Table A.2 Reverse motion sequence in the first sector

Position (mm)	Phase	Stator	Translator
0-12.6	B_1	$S_2 - S_5$	$T_2 - T_4$
12.6-32.6	C_1	$S_1 - S_4$	$T_1 - T_3$
32.6-52.6	A_1	$S_3 - S_6$	$T_2 - T_4$
52.6-72.6	B_1	$S_2 - S_5$	$T_1 - T_3$
72.6-92.6	C_2	$S_7 - S_{10}$	$T_4 - T_6$
92.6-112.6	A_1	$S_3 - S_6$	$T_1 - T_3$
112.6-132.6	B_2	$S_8 - S_{11}$	$T_4 - T_6$
132.6-152.6	C_2	$S_7 - S_{10}$	$T_3 - T_5$
152.6-172.6	A_2	$S_9 - S_{12}$	$T_4 - T_6$
172.6-192.6	B_2	$S_8 - S_{11}$	$T_3 - T_5$
192.6-212.6	C_2	$S_7 - S_{10}$	$T_2 - T_4$
212.6-232.6	A_2	$S_9 - S_{12}$	$T_3 - T_5$
232.6-240	B_2	$S_8 - S_{11}$	$T_2 - T_4$

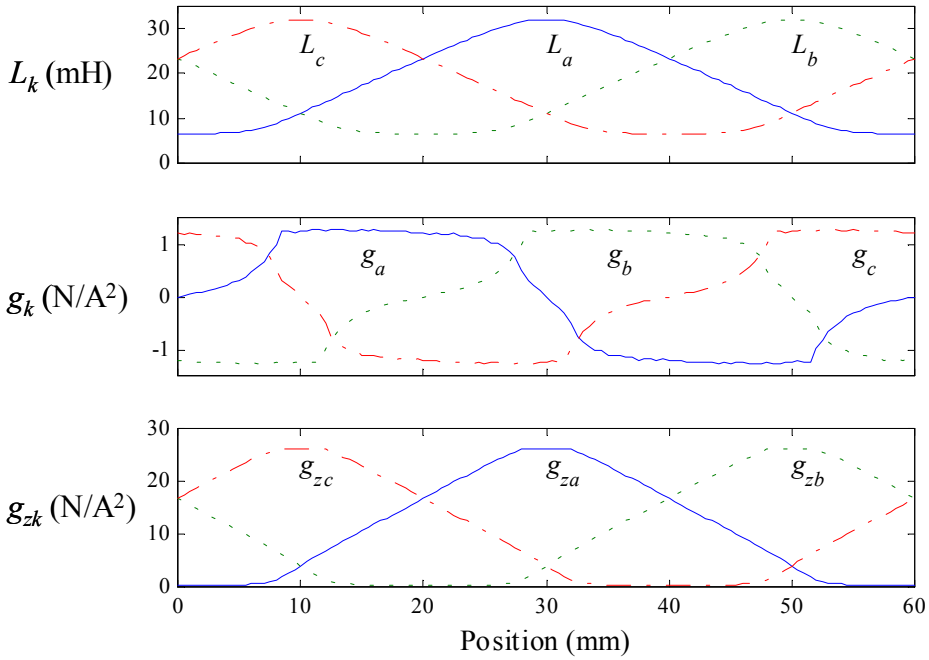

Fig. A.2 Parameters at rated current

In a prototype LSRM, the stator pole width w_{sp} and slot width w_{ss} are both 20mm and the translator pole width w_{tp} and slot width w_{ts} are 24mm and 36mm, respectively. The energization sequence $a_1a_1' - b_1b_1' - c_2c_2' - a_1a_1' - \cdots$ makes the translator move in the forward direction continuously. Similarly, a reverse direction sequence can be deduced. Since the prototype has 6 translator poles, a gating sequence based on the above description is developed such that the translator experiences continuous forward or backward motion. The sequences for forward and reverse operations in the first sector for the LSRM prototype whose sector length is $6(w_{ss} + w_{sp}) = 6(20 + 20) = 240$ mm are shown in Tables A.1 and A.2. Sequences in other sectors are derived in a similar manner.

In an LSRM, excitation of a phase winding produces a propulsion force along the x direction and a normal force along the z direction. Similar to a RSRM, inductance values can be obtained as the LSRM progresses from the unaligned to the aligned and back to the unaligned position. Assuming that the translator is moving in the direction x, and the three phases are named as a, b and c, Fig. A.2 shows inductance L_k, the rate of change of inductance with respect

to x, $\partial L_k / \partial x$, and the rate of change of inductance with respect to z, $\partial L_k / \partial z$ for $k = a, b, c$ at rated current. For notational convenience, $\partial L_k / \partial x$ and $\partial L_k / \partial z$ are defined as,

$$g_k \equiv \frac{\partial L_k}{\partial x} \qquad \text{for } k=a,\ b,\ c \qquad \text{(A.2)}$$
$$g_{zk} \equiv \frac{\partial L_k}{\partial z}$$

It is noticed that the normal force plays an important role in this machine. From the prototype LSRM parameters described above, it is observed that the patterns shown in Fig. A.2 repeats every $(w_{tp} + w_{ts}) = (24 + 36) = 60$ mm. At the points where the inductance is highest, a set of translator poles are in full alignment with two associated stator poles, which constitutes one phase. At zero position, the interpolar axis located between two translator poles T_2 and T_3, is aligned with the polar axis of the stator pole S_3.

A.2 Converter Topology

The proposed LSRM stator is divided into N_{sc} sectors, each with 6 poles or 3 consecutive phases. The windings are connected such that the coils in one sector are not connected to the coils in other sectors, *i.e*, each sector can operate independently. Based on it, the converter shown in Fig. A.3 is developed for the LSRM drive. Considering only one sector, it is observed that the converter can operate like a regular asymmetric bridge converter used in RSRM with all the advantages associated with that topology. Only three top switches are used, one for each phase. Each phase winding has its own switch. So although there are $3N_{sc}$ individual phases, only $(3N_{sc} + 3)$ switches are used unlike the asymmetric half-bridge converter that would use $6N_{sc}$ switches. The duty cycle of operation of the lower switches is $1/(3N_{sc})$ and smaller heat sinks are used when compared to the upper switches that have a duty cycle of $1/3$. With this converter, only a single current sensor per phase for the entire track is required and the unipolar switching strategy described in Chapter 6 can be applied.

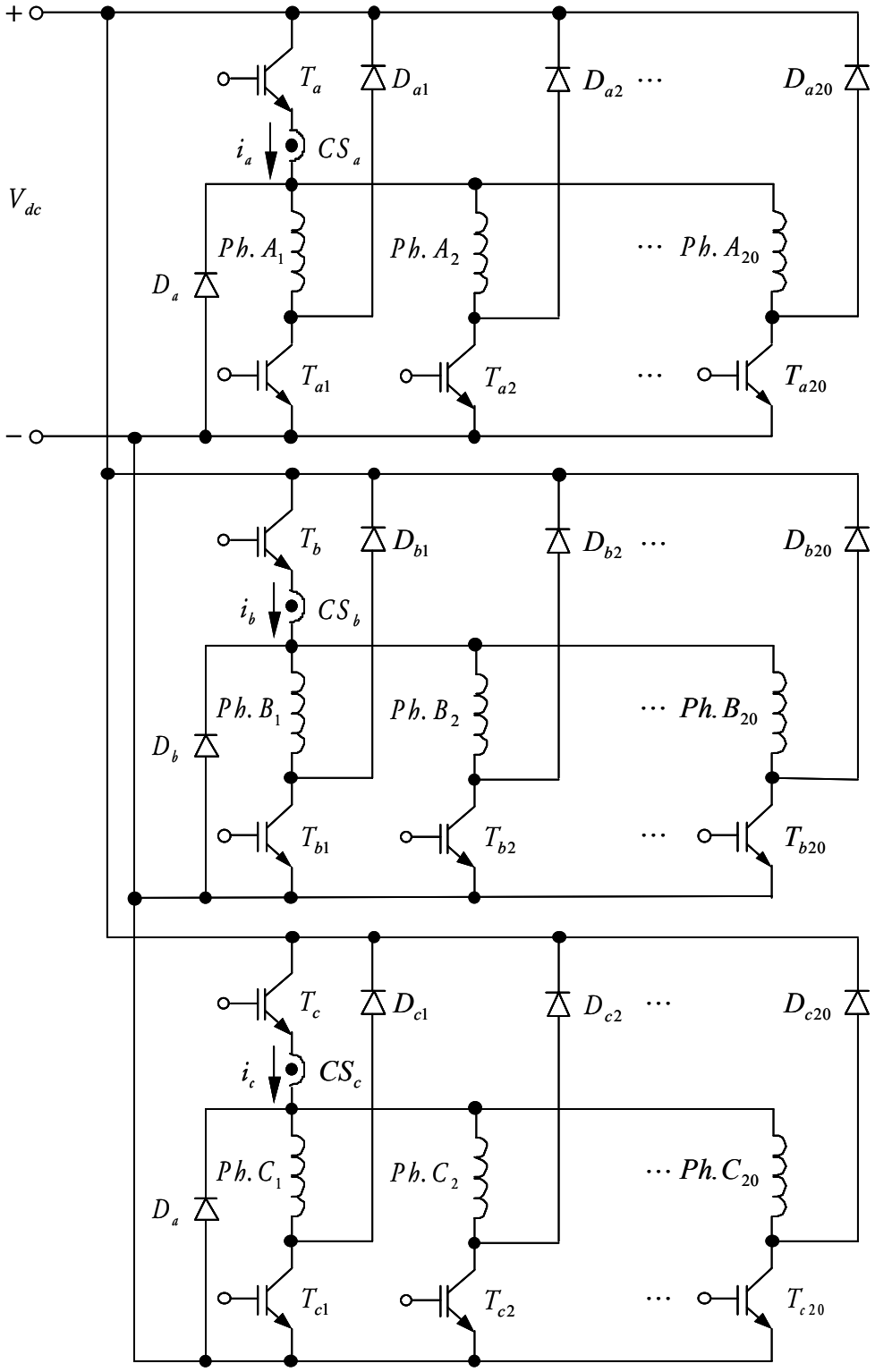

Fig. A.3 Proposed converter topology

A.3 Force Control Strategies

A.3.1 Single Phase Excitation

If a phase is energised during the rising slope of the inductance, a positive force is produced and if a phase is energised during the falling slope of the inductance, negative force is produced as shown in Fig. A.4. The polarity of the current makes no difference. Also, note that the force is dependent on the translator position. The commanded force generated by this control scheme is given as,

$$F_{xe}^{*} = \frac{1}{2} K_T \left(i_k^{*}\right)^2 \text{ for } k = a, b, c \tag{A.2}$$

where K_T is the average value of g_a for an excitation interval. From Fig. A.3, the optimal commutation position that minimizes current for a maximum possible machine efficiency [16], for phase a can be found to be 27.4 mm (the position where the rising torque function g_b is equal to the falling torque function g_a) and the average value of g_a for $7.4mm \le x \le 27.4mm$ is calculated as,

$$G_a \equiv K_T = 1.1808 \text{ N/A}^2 \tag{A.3}$$

The simulation results shown in Fig. A.5 are performed with a PWM carrier frequency of 20 kHz with the proposed current controller described in Section A.4 and 120 VAC, 1 ϕ, supply voltage to the rectifier. As the current commands are calculated using the average value of g_a, there is a large force ripple during commutation as seen in Fig. A.5. This might be considered in the design stage of the LSRM to reduce the force ripple, but in a practical machine, it is not easy to achieve a flat-topped force function. Increased audible noise and stress on the mechanical structure are drawbacks of this operation. For the rectangular phase currents, it is seen that the force is produced in a pulsed form, resulting in a possible increase in force ripple due to the limited bandwidth of current control loop.

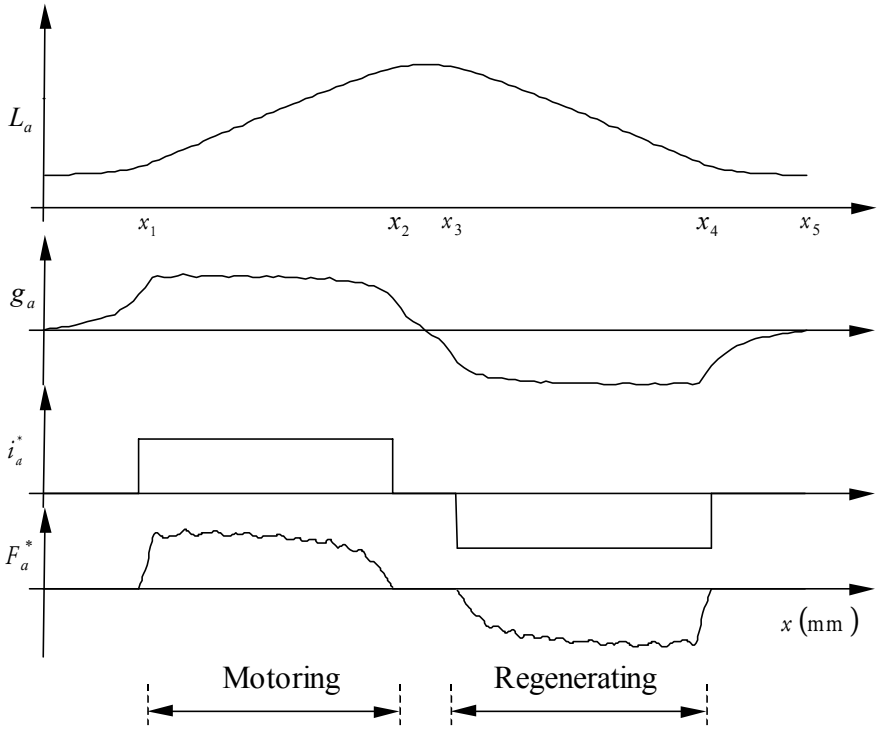

Fig. A.4 Elementary operation of the LSRM

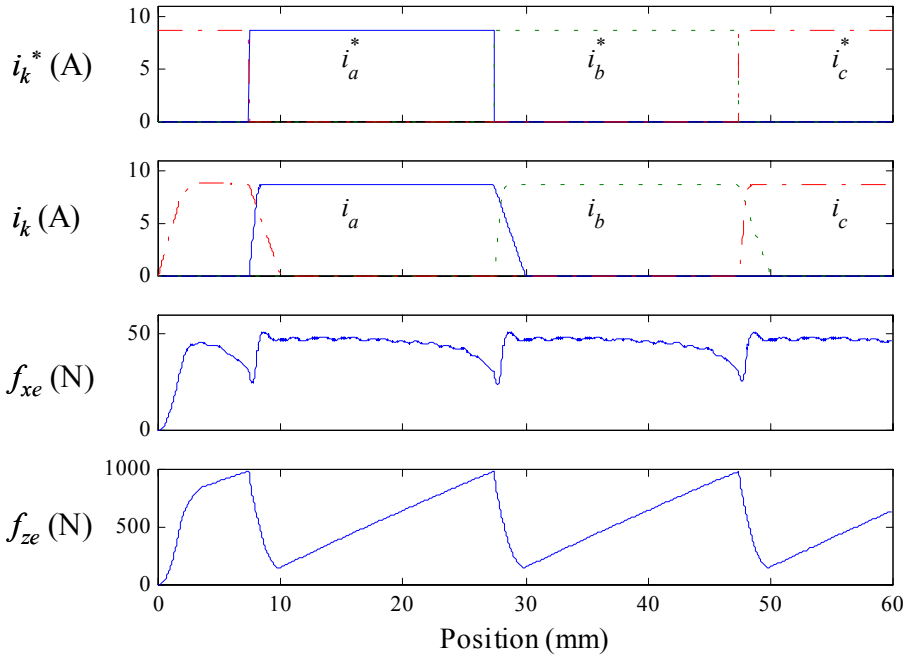

Fig. A.5 Simulation results of the single-phase excitation at $F_{xe}^* = 45$ N and $\dot{x}^* = 1.5$ m/s

A.3.2 Multiphase Excitation

Since a high force ripple will be present when only one phase of the LSRM is excited at a time, a multiphase excitation scheme is proposed. By distributing force to adjacent phases with the proposed Force Distribution Function (FDF), both phases can contribute to produce force of the same polarity. This reduces the rate of change of phase currents and the peak current magnitude. The proposed FDF also helps to reduce the peak and the rate of change of the normal force compared with the single-phase excitation method described before. Fig A.6 shows the proposed FDF when $F_{xe}^{*} \geq 0$ and $F_{xe}^{*} < 0$. The simulation results of the proposed method are shown in Fig. A.7. Other simulation parameters with regards to the PWM carrier frequency and supply voltage are identical to the simulation using single-phase excitation. If actual phase currents track the current commands precisely, by controlling phase currents, the required force is obtained. In other words, if $i_k^{*} \cong i_k$ for $k = a,b,c$, the actual force can be expressed as,

$$F_{xe}^{*} = \frac{1}{2}\sum_{k=a,b,c} g_k \left(i_k^{*}\right)^2 \cong \frac{1}{2}\sum_{k=a,b,c} g_k \left(i_k\right)^2 = F_{xe} \tag{A.4}$$

Then, the force control becomes a matter of selection of FDF and generation of phase current commands. The proposed force control loop is composed of FDF, Current Command Generation (CCG) and the current controller as illustrated in Fig. A.8.

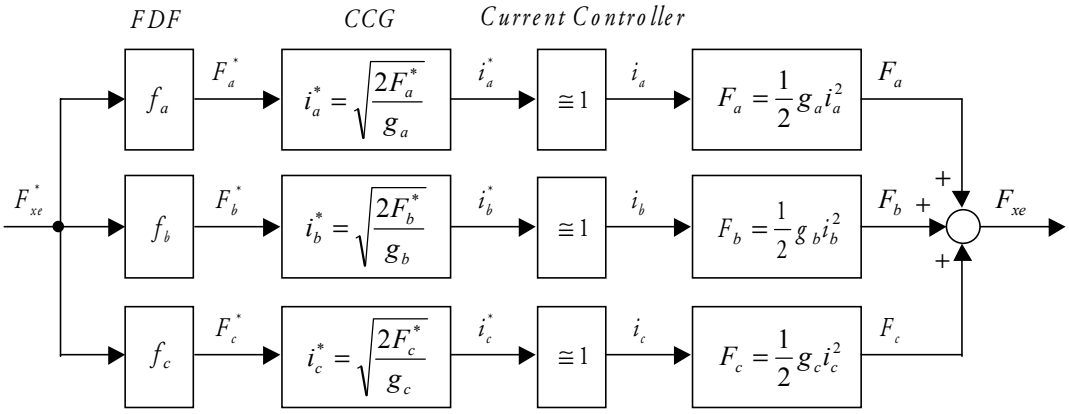

Fig. A.6 Proposed force control loop

Table A.3 Forward and reverse motion sequence in the first sector

Position (mm)	Forward	Reverse
0-10	C_1, A_1	B_1
10-20	A_1	B_1, C_1
20-30	A_1, B_1	C_1
30-40	B_1	C_1, A_1
40-50	B_1, C_2	A_1
50-60	C_2	A_1, B_1
60-70	C_2, A_1	B_1
70-80	A_1	B_1, C_2
80-90	A_1,B_2	C_2
90-100	B_2	C_2, A_1
100-110	B_2, C_2	A_1
110-120	C_2	A_1, B_2
120-130	C_2 , A_2	B_2
130-140	A_2	B_2, C_2
140-150	A_2, B_2	C_2
150-160	B_2	C_2, A_2
160-170	B_2, C_2	A_2
170-180	C_2	A_2 , B_2
180-190	C_2 , A_2	B_2
190-200	A_2	B_2, C_2
200-210	A_2, B_2	C_2
210-220	B_2	C_2, A_2
220-230	B_2, C_2	A_2
230-240	C_2	A_2 , B_2

The sequences for forward and reverse operations in the first sector for the proposed scheme are shown in Table A.3. Sequences in other sectors are derived in a similar manner. Tables A.1 and A.2 can be referred to identify associated stator and translator poles.

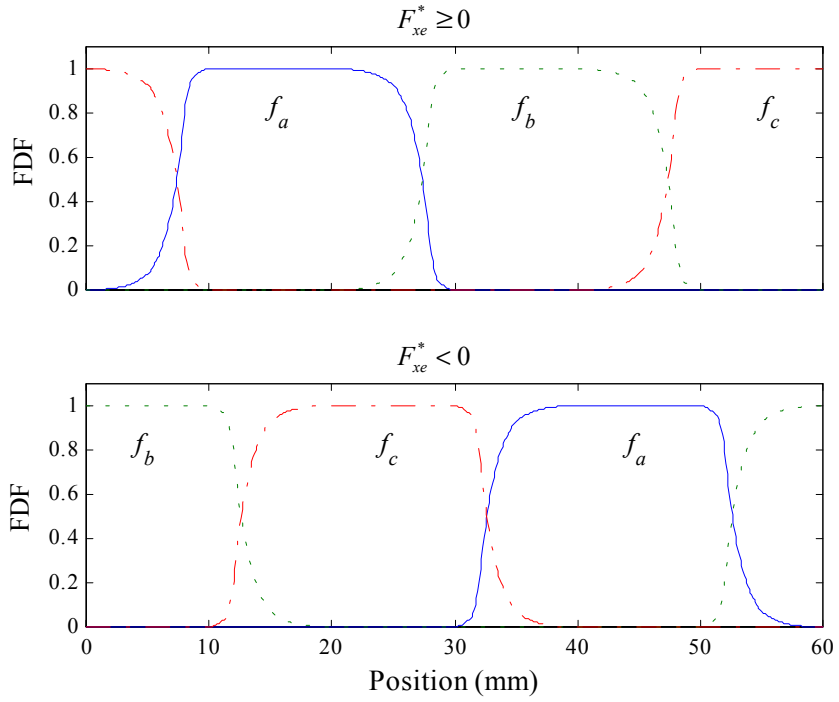

Fig. A.7 Proposed FDF

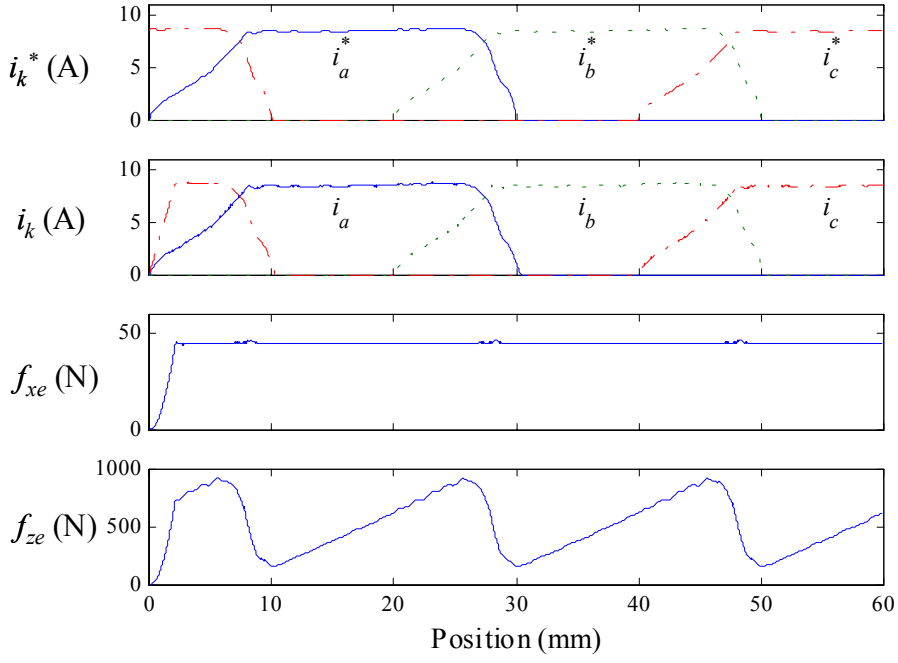

Fig. A.8 Simulation results of the proposed scheme at $F_{xe}^* = 45$ N and $\dot{x}^* = 1.5$ m/s

Table A.4 Proposed FDF in an excitation period

	$F_{xe}^* \geq 0$		$F_{xe}^* < 0$	
$f_a(x)$	$\frac{g_a(x)^2}{g_c(x)^2 + g_a(x)^2}$	for $0 \leq x < 10$	0	for $0 \leq x < 30$
	1	for $10 \leq x < 20$	$\frac{g_a(x)^2}{g_c(x)^2 + g_a(x)^2}$	for $30 \leq x < 40$
	$\frac{g_a(x)^2}{g_a(x)^2 + g_b(x)^2}$	for $20 \leq x < 30$	1	for $40 \leq x < 50$
	0	for $30 \leq x < 60$	$\frac{g_a(x)^2}{g_a(x)^2 + g_b(x)^2}$	for $50 \leq x < 60$
$f_b(x)$	0	elsewhere	1	for $0 \leq x < 10$
	$\frac{g_b(x)^2}{g_a(x)^2 + g_b(x)^2}$	for $20 \leq x < 30$	$\frac{g_b(x)^2}{g_b(x)^2 + g_c(x)^2}$	for $10 \leq x < 20$
	1	for $30 \leq x < 40$	0	for $20 \leq x < 50$
	$\frac{g_b(x)^2}{g_b(x)^2 + g_c(x)^2}$	for $40 \leq x < 50$	$\frac{g_b(x)^2}{g_a(x)^2 + g_b(x)^2}$	for $50 \leq x < 60$
$f_c(x)$	$\frac{g_c(x)^2}{g_c(x)^2 + g_a(x)^2}$	for $0 \leq x < 10$	0	elsewhere
	0	elsewhere	$\frac{g_c(x)^2}{g_b(x)^2 + g_c(x)^2}$	for $10 \leq x < 20$
	$\frac{g_c(x)^2}{g_b(x)^2 + g_c(x)^2}$	for $40 \leq x < 50$	1	for $20 \leq x < 30$
	1	for $50 \leq x < 60$	$\frac{g_c(x)^2}{g_c(x)^2 + g_a(x)^2}$	for $30 \leq x < 40$

Table A.4 shows the proposed FDF in an excitation period. The cycle for the prototype repeats every 60 mm. The function is described based on the relative linear position x. The sum of the phase force commands equals the force command at all positions, and given as,

$$F_k^* = F_{xe}^* f_k \text{ for } k = a, b, c \text{ and } \sum_{k=a,b,c} f_k = 1 \text{ for all } x \tag{A.5}$$

Then,

$$\sum_{k=a,b,c} F_k^* = F_{xe}^* \sum_{k=a,b,c} f_k = F_{xe}^* \tag{A.6}$$

Note that when $f_k = 0$, to avoid unnecessary switching, the corresponding phase is turned off instead of regulating i_k to zero. From the distributed phase force command F_k^*, the current command i_k^* is computed as,

$$i_k^* = \sqrt{\frac{2F_k^*}{g_k}} \text{ for } k = a, b, c \tag{A.7}$$

The resultant phase currents and normal force at rated force are shown in Fig. A.8. The changing rate of the phase current commands are much reduced so the current commands are more easily followed with practical and moderate controller gains. The force errors by the single-phase excitation scheme and the proposed scheme are 60.8% and 4.9%, respectively. Compared with the single-phase excitation, the proposed scheme shows about 6.7% decrease in the peak normal force and it helps to reduce friction between the wheels and track. In addition, the smooth waveform of the normal force can reduce the stress asserted on the mechanical structure.

A.4 Current Controller

A proportional plus integral controller is considered for the present implementation. The voltage equation of a phase of the LSRM neglecting the mutual inductance is given as,

$$v_k = R_s i_k + \frac{d\lambda_k}{dt} \text{ for } k = a, b, c \tag{A.8}$$

where

$$\lambda_k = L_k i_k \text{ for } k = a, b, c \tag{A.9}$$

By substituting (A.9) into (A.8),

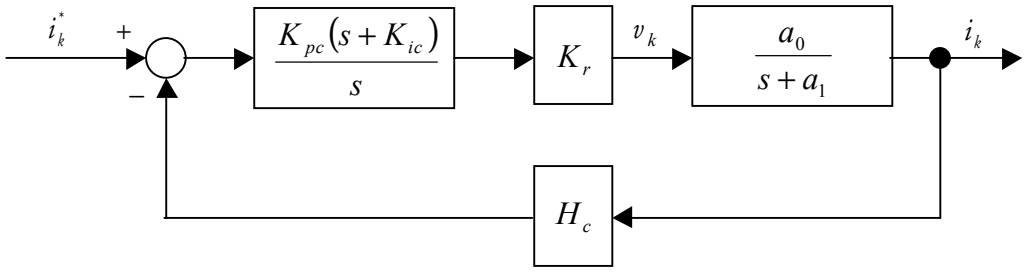

Fig. A.9 Current control loop with PI controller

$$\frac{di_k}{dt} = -a_1 i_k - a_2 \dot{x} \cdot i_k + a_0 v_k \text{ for } k = a, b, c \tag{A.10}$$

where,

$$\begin{aligned} a_0 &= \frac{1}{L_k} \\ a_1 &= \frac{R_s}{L_k} \text{ for } k = a, b, c \\ a_2 &= \frac{g_k}{L_k} \end{aligned} \tag{A.11}$$

System (A.10) can be easily linearized and decoupled by defining the control input v_k as,

$$v_k = a_2 \dot{x} \cdot i_k / a_0 + u_k \text{ for } k = a, b, c \tag{A.12}$$

where u_k is the new control input to be designed. Substituting (A.12) into (A.10) yields

$$\frac{di_k}{dt} = -a_1 i_k + a_0 u_k \text{ for } k = a, b, c \tag{A.13}$$

To obtain the required transient and steady state performance the new control input u_k is given by a PI controller as shown in Fig. A.9,

$$u_k = K_{pc}\left[\left(i_k^* - i_k\right) + K_{ic}\int_0^t \left(i_k^* - i_k\right) d\tau\right] \text{ for } k = a, b, c \tag{A.14}$$

where K_{pc} and K_{ic} are the gains of the current loop PI controller. The gains K_{pc} and K_{ic} can be evaluated by a conventional design procedure based on the frequency response characteristics. From the simplified current control loop shown in Fig. A.9, the system transfer functions $G_c(s)$ is derived as follows.

$$\begin{aligned} G_c(s) \equiv \frac{i_k(s)}{i_k^*(s)} &= \frac{1}{H_c} \cdot \frac{a_0 H_c K_r K_{pc} s + a_0 H_c K_r K_{pc} K_{ic}}{s^2 + (a_0 H_c K_r K_{pc} + a_1) s + a_0 H_c K_r K_{pc} K_{ic}} \\ &\cong \frac{1}{H_c} \cdot \frac{K_1 K_{pc} s + K_1 K_{pc} K_{ic}}{s^2 + K_1 K_{pc} s + K_1 K_{pc} K_{ic}} \quad \text{for } a_0 H_c K_r K_{pc} >> a_1 \end{aligned} \tag{A.15}$$

Where H_c and K_r are the current feedback gain and the converter gain, respectively and $K_1 = a_0 H_c K_r$.

To determine K_{pc} and K_{ic} to meet the control objectives, a simple and straightforward design procedure is proposed. One of the most common control objectives is the bandwidth ω_c and the damping ratio ζ_c of the current control loop. For a given set of ω_c and ζ_c, controller gains are calculated algebraically as,

$$\begin{aligned} K_{pc}(x) &= \frac{2\zeta_c \omega_c}{\sqrt{\left(1 + 2\zeta_c^2\right) + \sqrt{\left(1 + 2\zeta_c^2\right)^2 + 1}}} \cdot \frac{1}{K_1(x)} \\ K_{ic} &= \frac{\omega_c}{2\zeta_c \sqrt{\left(1 + 2\zeta_c^2\right) + \sqrt{\left(1 + 2\zeta_c^2\right)^2 + 1}}} \end{aligned} \tag{A.16}$$

A.5 Experimental Set-up

A picture of the prototype LSRM is shown in Fig. A.10. There are 120 stator poles spread across a length of 4.8 m. A magnetic sensor strip has a resolution of 10μm runs alongside the stator giving position feedback. Fig. A.10 shows the experimental setup of the control system.

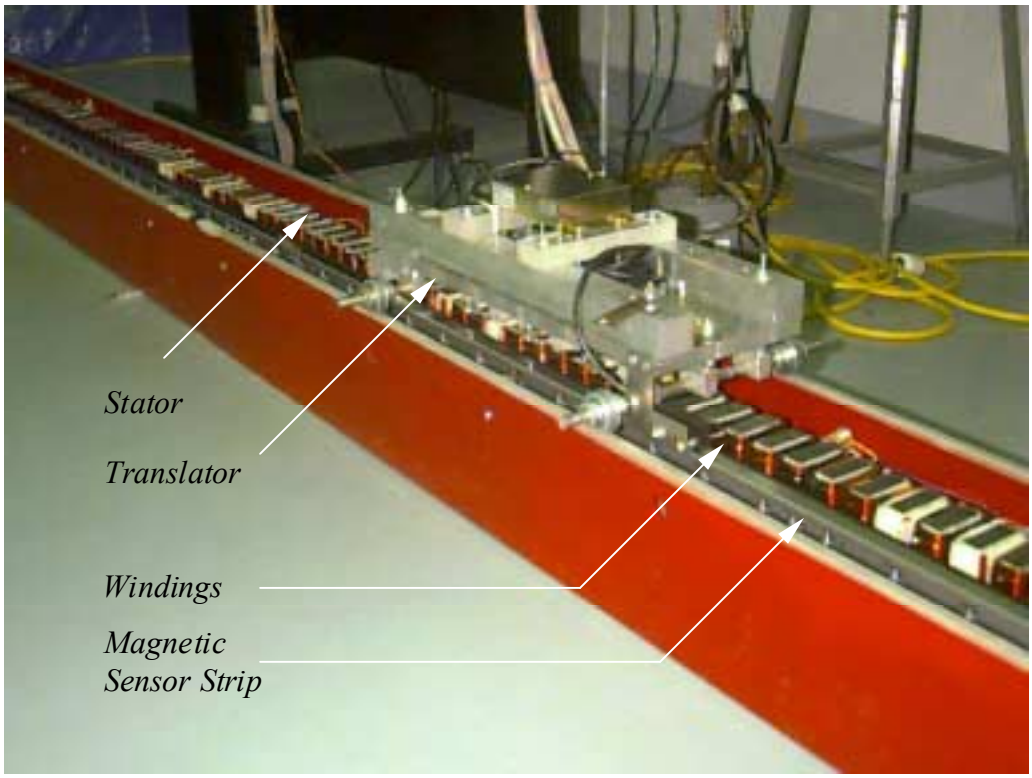

Fig. A.10 Prototype LSRM

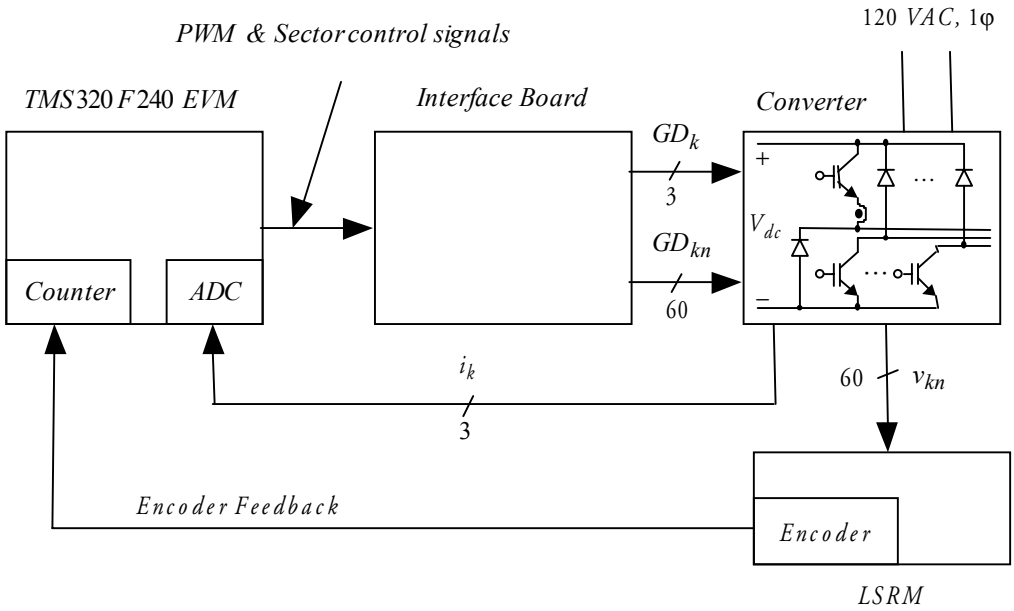

Fig. A.11 Experimental setup

The control system is digitally implemented with a sampling time of 50 μs using a TMS320F240 DSP evaluation module with an interface board. A proportional plus integral controller is implemented as a velocity controller along with the force controller within the DSP. The interface board generates gate drive signals for all converter boards from the PWM and sector control signals obtained from the evaluation module. Sector control signal identifies the active sector. The PWM carrier frequency is 20 kHz. The experimental results are described in Chapter 7.

A.6 Conclusions

It is shown that the proposed force controller maximizes the force producing capability of the LSRM with minimized force ripple and also reduces the peak normal force. An excellent correlation between simulation and experimental results is demonstrated. The key contributions of this study are:

1) A converter with minimum number of devices for this specific configuration of LSRM that has no operational restrictions is chosen and implemented.
2) A force ripple free control of the LSRM has been realised with multiphase excitation and has been experimentally verified on a 4.8m long prototype.
3) A unipolar switching for the proposed converter is developed and implemented.
4) The feedback linearizing current controller is derived, implemented, and tested to yield a high bandwidth and good damping. The current and velocity controllers are experimentally validated.
5) The system level controller has been realised with a DSP thus establishing a flexible software controller for future innovations.

List of Symbols

z : Displacement in normal force direction

x:	Displacement in propulsion force direction
N_{sc}:	Number of stator sectors
n_s:	Number of stator poles
n_t:	Number of translator poles
w_{sp}:	Width of stator pole
w_{ss}:	Width of stator slot
w_{tp}:	Width of translator pole
w_{ts}:	Width of translator slot
M:	Mass of the translator
$\dot{x}^*(\dot{x})$:	Commanded (actual) velocity
$F_{xe}^*(F_{xe})$:	Commanded (actual) electromagnetic force
$F_k^*(F_k)$ [1]:	Commanded (actual) phase electromagnetic force
L_k:	Self inductance
g_k:	Changing rate of inductance with respect to x
g_{zk}:	Changing rate of inductance with respect to z
V_{dc}:	DC link voltage, V
v_{kn} [2]:	Phase voltage in the nth sector
$i_k^*(i_k)$:	Commanded (actual) phase current
$\lambda_k^*(\lambda_k)$:	Commanded (actual) phase flux linkage
f_k:	Force function
H_c:	Current feedback gain
K_r:	Converter gain
ω_c:	Current loop bandwidth
ζ_c:	Current loop damping ratio
K_{pc}:	Proportional gain of the current control loop

[1] k=a, b, c
[2] n=1, 2, …, 20

K_{ic} :	Integral gain of the current control loop
GD_k :	Upper gate driver signal
GD_{kn} :	Lower gate drive signal in the n^{th} sector

LSRM Parameters

Rated Power:	200	W
Rated Force:	45	N
Rated Velocity, $\dot{x}_{rat}$:	1.5	m/sec
Rated Current, I_{rat} :	8.5	A
$L_{\min}$ at I_{rat} :	6.39	mH
$L_{\max}$ at I_{rat} :	31.96	mH
Stator resistance at $20^{\circ}C$, R_s :	0.797	Ω
Mass of the translator, *M*:	20	Kg

APPENDIX B: DERIVATION OF PROPORTIONAL GAIN K_p AND INTEGRAL GAIN K_i

Proportional and integral gains of a PI controller for a specific second-order system, which is common in this research, were derived from design specifications given by the system bandwidth ω_c and the damping ratio ζ_c. For a given second-order system transfer functions $G_c(s)$ is represented as,

$$G_c(s) = \frac{2\zeta_c \omega_n s + \omega_n^2}{s^2 + 2\zeta_c \omega_n s + \omega_n^2} \tag{B.1}$$

where,

$$\begin{aligned} 2\zeta_c \omega_n &= K_1 K_p \\ \omega_n^2 &= K_1 K_p K_i \end{aligned} \tag{B.2}$$

K_1 is a specific system constant and K_p and K_i are the proportional and integral gains of a PI controller, respectively. The system bandwidth ω_c is the frequency at which the magnitude of $G_c(j\omega)$ drops to $1/\sqrt{2}$ of its zero-frequency value. Thus we have

$$\left|G_c(j\omega)\right|_{\omega=\omega_c} = \sqrt{\frac{\left(\omega_n^2\right)^2 + \left(2\zeta_c \omega_n \omega_c\right)^2}{\left(-\omega_c^2 + \omega_n^2\right)^2 + \left(2\zeta_c \omega_n \omega_c\right)^2}} = \frac{1}{\sqrt{2}} \tag{B.3}$$

By rearranging Eq. (B.3), we have

$$\omega_c^4 - 2\left(1 + 2\zeta_c^2\right)\omega_n^2 \omega_c^2 - \omega_n^4 = 0 \tag{B.4}$$

This equation leads to

$$\omega_c^2 = \left(1 + 2\zeta_c^2\right)\omega_n^2 \pm \sqrt{\left(1 + 2\zeta_c^2\right)^2 + 1} \cdot \omega_n^2 \tag{B.5}$$

Since ω_c is a positive real value for any ζ_c, the plus sign should be chosen in Eq. (B.5). Therefore the bandwidth ω_c of the second order system is determined as,

$$\omega_c = \sqrt{\left(1+2\zeta_c^2\right)+\sqrt{\left(1+2\zeta_c^2\right)^2+1}}\cdot\omega_n \tag{B.6}$$

By rearranging Eq. (B.2) for the controller gains K_p and K_i, we have

$$\begin{aligned} K_p &= \frac{2\zeta_c\omega_n}{K_1} \\ K_i &= \frac{\omega_n^2}{K_1 K_p} = \frac{\omega_n^2}{K_1\dfrac{2\zeta_c\omega_n}{K_1}} = \frac{\omega_n}{2\zeta_c} \end{aligned} \tag{B.7}$$

Substituting Eq. (B.6) into Eq. (B.7) yields

$$\begin{aligned} K_p &= \frac{2\zeta_c\omega_c}{\sqrt{\left(1+2\zeta_c^2\right)+\sqrt{\left(1+2\zeta_c^2\right)^2+1}}}\cdot\frac{1}{K_1} \\ K_i &= \frac{\omega_c}{2\zeta_c\sqrt{\left(1+2\zeta_c^2\right)+\sqrt{\left(1+2\zeta_c^2\right)^2+1}}} \end{aligned} \tag{B.8}$$

Hence, for a given set of bandwidth ω_c and damping ratio ζ_c, the proportional gain K_p and the integral gain K_i are calculated algebraically above.

APPENDIX C: SPECIFICATION OF THR PROTOTYPE SRM

Number of stator poles, P_s:	8	
Number of rotor poles, P_r:	6	
Stator pole arc, β_s:	16	degrees
Rotor pole arc, β_r:	18	degrees
Airgap length, g:	0.2	mm
Stator to rotor interpolar space height, g_i:	4.3	mm
Bore diameter, d:	45.0	mm
Outer diameter, d_o:	105.2	mm
Core length, l:	44.4	mm
Thickness of back-iron, c:	8	mm
Number of turns:	300	turns/phase
Stator resistance at $20^\circ C$, R_s:	1.6	Ω
Rated torque, $T_{e,rat}$:	0.4	Nm

REFERENCES

[1] R. Krishnan and P. N. Materu, “Analysis and Design of a Low-Cost Converter for Switched Reluctance Motor Drives,” IEEE Transactions on Industry Applications, vol. 29, no. 2, pp. 320-327, 1993.

[2] R. Krishnan and P. N. Materu, “Design of a Single-Switch-Per-Phase Converter for Switched Reluctance Motor Drives,” IEEE Transactions on Industrial Electronics, vol. 37, no. 6, pp. 469-476, 1990.

[3] C. Pollock and B.W. Williams, “A Unipolar Converter for a Switched Reluctance Motor,” IEEE Transactions on Industry Applications, vol. 26, no.2, pp. 222-228, 1990.

[4] W.F. Ray and R.M. Davis, “Inverter Drive for Doubly Salient Motors: Its Fundamental Behaviors, Linear Analysis and Cost Implications,” IEE Proceedings Part B, vol.2, no.6, pp. 185-193, 1979.

[5] M. Barnes and C. Pollock, “Power Electronic Converters for Switched Reluctance Drives,” IEEE Transactions on Power Electronics, vol. 13, no. 6, pp. 1100-1111, 1998.

[6] R. Krishnan, *Analysis and Design of Switched Reluctance Motor Drives*, EE6444 Course Notes, Motion Control Systems Research Group, Virginia Tech., 1995.

[7] P. J. Lawrenson, J. M. Stephenson, P. T. Blenkinsop, J. Corda, and N. N. Fulton, “Variable-Speed Switched Reluctance Motors,” IEE Proceedings Part B, pp. 253-265, 1980.

[8] J. Corda and J. M. Stephenson, “An Analytical Estimation of the Minimum and Maximum Inductances of a Double Salient Motor,” Proceedings of International Conference on Stepping Motors and Systems, pp. 50-59, 1979.

[9] C. W. Trowbridge, *An Introduction to Computer Aided Electromagnetic Analysis*, Vector Fields Ltd., 1990.

[10] A. R. Esatham, H. Yuan, G. E. Dawson, P. C. Choudhury, and P. M. Cusack, “A Finite Element Evaluation of Pole Shaping in Switched Reluctance Motors,” Electrosoft, vol.1, no. 1, pp. 55-67, 1990.

[11] G. E. Dawson, A. R. Eastham, and J. Mizia, “Switched –Reluctance Motor Torque Characteristics : Finite-Element Analysis and Test Results,” IEEE Transactions on Industry Applications, vol. 23, no. 3, pp. 532-537, 1987.

[12] J. F. Lindsay, R. Arumugam, R. Krishnan, “Finite-Element Analysis Characterization of a Switched Reluctance Motor with Multitooth per Stator Pole,” IEE Proceedings Part B, vol. 133, no. 6, pp. 347-353, 1986.

[13] R. Arumugam, D. A. Lowther, R. Krishnan, and J. F. Lindsay, “Magnetic Field Analysis of a Switched Reluctance Motor Using a Two-Dimensional Finite Element Model,” IEEE Transactions on Magnetics, vol. 21, no. 5, pp. 1883-1885, 1985.

[14] J. C. Moreiara and T. A. Lipo, “Simulation of a Four Phase Switched Reluctance Motor Including the Effect of Mutual Coupling,” Electric Machines and Power Systems, vol. 16, pp. 281-299, 1989.

[15] H. H. Moghbelli, G. E. Adams, and R. G. Hoft, “Prediction of the Instantaneous and Steady State Torque of the Switched Reluctance Motor Using the Finite Element Method (FEM),” IAS, pp. 59-70,1988.

[16] D. S. Schramm, B. W. Williams, and T. C. Green, “Torque Ripple Reduction of Switched Reluctance Motors by Phase Current Optimal Profiling,” PESC, pp. 857-860, 1992.

[17] I. Husain and M. Ehsani, “Torque Ripple minimization in Switched Reluctance Motor Drives by PWM Current Control,” IEEE Transactions on Power Electronics, vol. 11, no.1, pp. 83-88,1996.

[18] M. Ilic-Spong, T. J. E. Miller, S. R. Macminn, and J. S. Thorp, “Instantaneous Torque Control of Electric Motor Drives,” IEEE Transactions on Power Electronics, vol. 2, no.1, pp. 55-61,1987.

[19] R. S. Wallace and D. G. Taylor, “A Balanced Commutator for Switched Reluctance Motors to Reduce Torque Ripple,” IEEE Transactions on Power Electronics, vol. 7, no.4, pp. 617-626,1992.

[20] C. H. Kim and I. J. Ha, “A New Approach to Feedback-Linearizing Control of Variable Reluctance Motors for Direct-Drive Applications,” IEEE Transactions on Control Systems Technology, vol. 4, no. 4, pp. 348-362, 1996.

[21] P. Pillay, Y. Liu, W. Cai, and T. Sebastian, “ Multiphase operation of Switched Reluctance Motor Drives,” IEEE Industry Applications Society Annual Meeting, Conference Record, pp. 310-317, 1997.

[22] I. Husain and M, Ehsani, “Rotor Position Sensing in Switched Reluctance Motor Drives by Measuring Mutually Induced Voltage,” IEEE Transactions on Industry Applications, vol. 30, no. 3, pp. 665-672, 1994.

[23] P. C. Krause, *Analysis of Electric Machinery*, McGraw-Hill, 1986.

[24] H. K. Bae and R Krishnan, “A Study of Current Controllers and Development of a Novel Current Controller for High Performance SRM Drives,” IEEE Industry Applications Society Annual Meeting, Conference Record, pp. 68-75, 1996.

[25] N. Mohan *et al*., *Power Electronics : Converters, Applications and Design*, John Wiley & Sons,1989.

[26] R. Krishnan and S. Lee, “PM Brushless DC Motor with a New Power-Converter Topology,” IEEE Transactions on Industry Applications, vol. 33, no. 4, pp. 973-982, 1997.

[27] J. J. E. Slotine and W. Li, *Applied Nonlinear Control*, Prentice-Hall, 1991.

[28] R. Krishnan and P. N. Materu, “Measurement and Instrumentation of a Switched Reluctance Motor,” IEEE Industry Applications Society Annual Meeting, Conference Record, pp. 116-121, 1989.

[29] H. K. Bae, B. S. Lee, P. Vijayraghavan, and R. Krishnan, “A Linear Switched Reluctance - Motor: Converter and Control,” IEEE Industry Applications Society Annual Meeting, Conference Record, pp. 547-554, 1999.

[30] B. S. Lee, H. K. Bae, P. Vijayraghavan, and R. Krishnan, “Design of a Linear Switched Reluctance Machine,” IEEE Industry Applications Society Annual Meeting, Conference Record, pp. 2267-2274, 1999.

[31] Magsoft Corporation, *FLUX2D User’s Guide*, Ver. 7.11, 1995.

[32] Magsoft Corporation, *FLUX2D Command Reference*, Ver. 7.11, 1995.

[33] K. Adamiak, D. Barlow, C.P. Choudhury, P.M. Cusack, G.E. Dawson, A.R. Eastham, B. Grady, E. Ho, Y. Hongping, L. Pattison, and J. Welch, “The Switched Reluctance Motor as a Low-speed Linear Drive,” International Conference on Maglev and Linear Drives, Las Vegas, NV, pp. 39-43, May 1987.

[34] Takayama, Y. Takasaki, R. Ueda, T. Sonoda, and T. Iwakane, “A New Type Switched Reluctance Motor,” IEEE Industry Applications Society Annual Meeting, Conference Record, pp. 71-8, vol. 1, Oct. 1988.

[35] P.M. Cusack, G.E. Dawson, and T.R. Eastham, “Design, Control and Operation of a Linear Switched Reluctance Motor,” Canadian Conference on Electrical and Computer Engineering, pp. 19.1.1-5, 1991.

[36] C.T. Liu and Y.N. Chen, “On the Feasible Polygon Classifications of Linear Switched Reluctance Machines,” IEEE International Electric Machines and Drives Conference Record, pp.TB1/11.1-3, 1997.

[37] U.S. Deshpande, J.J. Cathey, and E. Richter, “A High Force Density Linear Switched Reluctance Machine,” IEEE Transactions on Industry Applications, vol. 31, no.2, pp.345-352, 1995.

[38] J. Corda and E. Skopljak, “Linear Switched Reluctance Actuator,” Sixth International Conference on Electrical Machines and Drives, Oxford, UK, pp. 535-539, 1993.

[39] D. Matt, R. Goyet, J. Lucidarme, and C. Rioux, “Longitudinal-field Multi-airgap Linear Reluctance Actuator,” Electric Machines and Power Systems, vol. 13, no. 5, pp. 299-313, 1987.

[40] J. Lucidarme, A. Amouri, and M. Poloujadoff, “Optimum Design of Longitudinal Field Variable Reluctance Motors-Application to a High Performance Actuator," IEEE Trans. on Energy Conversion, vol. 8, no. 3, pp. 357-361, 1993.

[41] I. Boldea, and S.A. Nasar, *Linear Electric Actuators and Generators*, Cambridge University Press, UK, pp. 163-178, 1997.

[42] T.J.E. Miller, *Switched reluctance motors and their control*, Clarendon Press, UK, 1993.

VITA

Mr Han-Kyung Bae was born in Seoul, Korea on April 10, 1963. He received the B.S. and M.S. degree in Control and Instrumentation Engineering from Seoul National University, Seoul, Korea in 1985 and 1992, respectively. In 1985, he joined R & D Center, Daewoo Heavy Industries, Inc., where he led a research team in developing a line of BLDCM drives for automation and a line of PMSM drives for machine tools. He joined the Ph.D. program at VPI & SU in fall, 1994. His research interests include electric motor drives, power electronics, and MagLev systems.